Chapter 3
The Demographics of Close-In Planets

K. Biazzo, V. Bozza, L. Mancini, and A. Sozzetti

Abstract The large sample of presently-known exoplanetary systems orbiting within a few au from their parent stars has enabled detailed studies of their demographics, which provide essential constraints for improved understanding of the processes at work in planet formation and evolution. In this Chapter, we first summarize the strengths and weaknesses of the two detection methods that have unveiled the population of short- and intermediate-separation exoplanets, i.e. the radial velocity (RV) and photometric transit techniques. Secondly, we review the wealth of information on the statistical properties of close-in exoplanets gathered from Doppler and transit surveys, focusing on occurrence rates as a function of two fundamental physical properties, mass and radius, and orbital separation. Next, we discuss statistical trends and correlations in the orbital and structural properties of two classes of planets that are not found in our Solar System, super Earths and sub-Neptunes. Then, we present an overview of the global and planet-to-planet patterns in the demographics of multiple-plane systems. We conclude by discussing the (primarily dynamical)

K. Biazzo
INAF—Rome Astronomical Observatory, Via di Frascati, 33, 00078 Monte Porzio Catone, RM, Italy
e-mail: katia.biazzo@inaf.it

V. Bozza
Department of Physics "E.R. Caianiello", University of Salerno, Via Giovanni Paolo II 132, 84084 Fisciano, SA, Italy
e-mail: valboz@sa.infn.it

L. Mancini
Department of Physics, University of Rome "Tor Vergata", Via della Ricerca Scientifica 1, 00133 Rome, Italy
e-mail: lmancini@roma2.infn.it

A. Sozzetti (✉)
INAF—Turin Astrophysical Observatory, Via Osservatorio 20, 10025 Pino Torinese, TO, Italy
e-mail: alessandro.sozzetti@inaf.it

K. Biazzo et al. (eds.), *Demographics of Exoplanetary Systems*,
Astrophysics and Space Science Library 466,
https://doi.org/10.1007/978-3-030-88124-5_3

information content of the orbital architectures of close-in planets (eccentricities, obliquities), and by highlighting the peculiar properties of the class of ultra-short period exoplanets. Throughout this Chapter, we underline key aspects of the fundamental link between planetary and host stars' properties and stress relevant elements of the mutual feedback between observations and theory (This Chapter is based on the lecture series given in May 2019 by A. Howard.).

3.1 Introduction

Out of the > 4300 known exoplanets to-date, for about 3800 (87%) the measured orbital period is $P \lesssim 1$ year.[1] Of course, this reflects an observational bias intrinsic to the two most successful planet detection techniques, i.e. photometric transits and radial velocities, which are primarily sensitive to close-in exoplanets. Furthermore, the very slow orbital motion of planets in wide orbits makes the reconstruction of the orbital parameters a very time-taking endeavor.

Whatever the reason, we can clearly see that the available statistics for close-in exoplanets is nearly an order of magnitude richer than that of exoplanets on distant orbits. With thousands of planets available, we can thus not only distinguish basic exoplanetary populations by radius, mass, density, incident stellar flux, but we are also starting to be sensitive to fine structures in the distributions (e.g., the famous 'radius valley', see Sect. 3.4.2) that can help us understand the formation scenarios of different classes of exoplanets. Furthermore, the numerous detections of multiple systems provide precious examples of the possible final outcomes of the formation of planetary systems. The existence of planets on high eccentric orbits with high obliquities with respect to the host star's spin is indicative of non-trivial dynamical interactions among the planets in the same disk. Every single system is thus important in its own regard as an individual case study, besides adding one more brick to all distributions of the various orbital and physical parameters.

3.2 Radial Velocity and Transit Measurement Techniques

Here we briefly review the basic concepts of the two main detection methods responsible for uncovering the present-day sample of close-in exoplanets, which has enable the demographics studies discussed in the following sections of this chapter. We will refer the reader to more specialized sources when necessary.

[1] Source: http://exoplanet.eu.

3.2.1 Radial Velocities

3.2.1.1 Doppler Measurements

The first successful observational campaign that found a planet around a solar-type star was based on high-precision RV monitoring of 51 Peg (Mayor and Queloz 1995). The principle of the Doppler technique had been well-known for more than a century and had been used to detect and characterize spectroscopic binaries (Pickering 1890). The orbital motion of two bodies around the common center of mass determines a periodic modulation of the radial velocity v_r, which can be detected to very high accuracy in terms of the Doppler shift z in the absorption lines in the spectrum:

$$z \equiv \frac{\lambda - \lambda_0}{\lambda_0} = \gamma(1 + v_r/c) - 1, \tag{3.1}$$

where λ_0 is the rest wavelength and γ is the relativistic Lorentz factor. For stellar binaries with sufficiently bright components, we can follow the absorption lines of both stars as they move periodically in opposite directions. In the case of a planetary system, we can only measure the RV variations of the host star, with a semi-amplitude $K_\star$ that is related to that of the planet by the law of barycenter: $K_\star = (M_\mathrm{p}/M_\star)\, K_p$. If the radial velocity of a close-in terrestrial planet around a solar-type ($M_\mathrm{p}/M_\star \simeq 10^{-5}$) has $K_p \sim 10^5$ m/s, the reflex velocity of the star would be of the order of $1\,\mathrm{m\,s^{-1}}$, which poses a severe challenge to current spectroscopic facilities.

In order to resolve such tiny displacements in the spectra, state-of-the-art instruments are typically echelle spectrographs (Bouchy et al. 2001) working at very high spectral resolution (i.e. with resolving power $R \sim$100,000). It is interesting to note that a displacement of $30\,\mathrm{cm\,s^{-1}}$ in the spectrum may correspond to just a few atoms on the detector surface! Therefore, such displacements can only be detected by means of cross-correlation techniques on broad regions of the spectrum (Fellgett 1955; Griffin 1967; Queloz 1995). Besides being very precise, the measurement apparatus must be very stable over long timescales, in order to enable firm detection of longer-period planets. For example, the motion of the Sun induced by Jupiter has a semi-amplitude of $12\,\mathrm{m\,s^{-1}}$ over a period of 12 years! For more information on the details of RV measurements, we refer the reader to specific reviews (e.g., Hatzes 2016; Perryman 2018; Wright 2018).

3.2.1.2 Form of the Signal

If we neglect the mutual interactions between the planets of the system, the measured radial velocity of the host star will be the sum of the individual Keplerian contributions. For n planets, we have

$$v_r(t) = \sum_{j=1}^{n} K_j \left[\cos(\omega_j + f_j(t)) + e_j \cos\omega_j\right] + \gamma + \dot{\gamma}(t - t_0), \qquad (3.2)$$

where t_0 is a reference epoch, e_j is the eccentricity of planet j, ω_j is the argument of the periastron, f_j is the true anomaly (angular position of the planet taken from the periastron), K_j is the semi-amplitude of the modulation, as detailed below. Equation (3.2) also contains a constant offset γ that corresponds to the stellar barycentric motion with respect to the Solar System, and a linear trend $\dot{\gamma}$, which takes into account possible systematic drifts in the measurement apparatus or long-term RV signals induced by long-period companions that cannot be modeled in detail within a finite duration campaign.

The semi-amplitude of the modulation is a function of the masses, period, eccentricity and inclination of the system. For a planet with mass $M_{\rm p}$, in convenient units, it can be cast in the form

$$K_\star = \frac{28.4\,{\rm m\,s^{-1}}}{\sqrt{1-e^2}} \frac{M_{\rm p}\sin i}{M_{\rm Jup}} \left(\frac{M_{\rm p}+M_\star}{M_\odot}\right)^{-2/3} \left(\frac{P}{1\,{\rm year}}\right)^{-1/3}, \qquad (3.3)$$

where $M_\odot$ is the solar mass and $M_{\rm Jup} \simeq 10^{-3} M_\odot$ the Jupiter mass.

This formula shows how the semi-amplitude of the RV signal decreases for longer period planets, following Keplerian laws. If the mass of the planet is negligible compared to the mass of the star, the third factor only depends on the mass of the host star. This implies that a conversion of the RV measure into a planetary mass requires accurate knowledge of the mass of the host star. This is typically obtained by means of techniques that match properties of the observed spectra to stellar model libraries (e.g., Torres et al. 2012). Of course, this procedure leaves some systematic uncertainty that is reflected in the ultimate error budget of the planetary mass.

Finally, we clearly see the well-known degeneracy between the mass of the planet and the inclination of the system. With RVs we can only derive a lower limit for the mass of the planet by fixing $\sin i = 1$ (edge-on system). However, without independent knowledge of the inclination, the mass of the planet can be anything from this lower limit to infinity ($\sin i = 0$ corresponds to a face-on system).

For hypothetical extrasolar analogues of the planets in our system, we get $K = 12\,{\rm m\,s^{-1}}$ for Jupiter and $K = 0.09\,{\rm m\,s^{-1}}$ for the Earth. Close-in planets are mildly favored by Kepler's third law. In fact, for a Jupiter-mass planet orbiting a solar-mass star with a period of 3 days we would have $K_\star = 140\,{\rm m\,s^{-1}}$, while an Earth-mass planet orbiting in one day would have $K = 0.6\,{\rm m\,s^{-1}}$. A more typical Super-Earth with $M_{\rm p} = 10\,M_\oplus$ and a period of 10 days would give $K = 3\,{\rm m\,s^{-1}}$. We conclude that it is relatively easy to detect hot giants, while we need better than $1\,{\rm m\,s^{-1}}$ accuracy to reach the regime of detectability of Earths and Super-Earths or to detect planets in wide orbits.

The shape of the radial velocity modulation, as shown in Eq. (3.3), is sinusoidal in the true anomaly. This angle is a linear function of time only for zero eccentricity. In general, in order to disclose the time-dependence of our signal, we must recall the

relation between the true anomaly and the eccentric anomaly E_j

$$\tan \frac{f_j(t)}{2} = \sqrt{\frac{1+e_j}{1-e_j}} \tan \frac{E_j(t)}{2} \,. \tag{3.4}$$

The eccentric anomaly as a function of time can be obtained by numerically solving the Kepler equation

$$E_j(t) - e_j \sin E_j(t) = \frac{2\pi(t - t_{p,j})}{P_j} \equiv M_j(t) \,, \tag{3.5}$$

where $t_{p,j}$ is the epoch of periastron passage and the last quantity is called the mean anomaly. Planets in eccentric orbits will move faster when they are at the periastron and slower at the apoastron. Therefore, the sine wave will be compressed at the periastron epoch and stretched at the apoastron. The position of the periastron is given by ω_j. In Fig. 3.1 we show how the shape of the Keplerian RV signal changes for different values of e and ω.

3.2.1.3 Signal Analysis

A generic, unevenly sampled RV time series will contain periodic modulations as described above superposed to instrumental and astrophysical noise. The latter mainly comes from the stellar activity of the target star, which generates oscillations

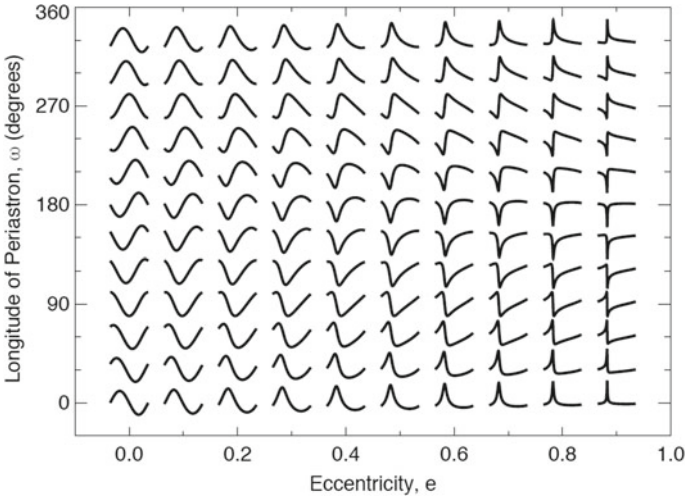

Fig. 3.1 Shapes of the radial velocity signals for various eccentricities and periastron arguments. *Note* that higher eccentricities lead to very rapid variations

in the RVs due to a variety of time-variable stellar surface structures (Queloz et al. 2001; Fischer et al. 2016). In order to extract the planetary signal, one may use the (Generalized) Lomb-Scargle periodogram (Lomb 1976; Scargle 1982; Zechmeister and Kürster 2009), which evaluates the χ^2 improvement coming from the fit of a sine wave compared to a constant function using a figure of merit called periodogram power computed as a function of a grid of trial periods. In such diagrams, the periodic signals arise as sharp peaks in power over the background. Furthermore, the periodogram may exhibit peaks produced by the cadence of the observations (the so-called window function), dictated, for example, by Earth's rotation and revolution period, and lunar cycles. Periodic RV signals induced by stellar activity will also be revealed in a periodogram. For in-depth discussions of how to unveil planetary signals in the presence of stellar activity see, for example, Haywood et al. (2014); Hatzes (2016).

When a planetary signal is identified, it can be subtracted from the data and the analysis can be repeated to search for progressively lower signals from other planets until the noise level is reached (Fischer et al. 2008). A variety of sophisticated methods for Keplerian orbit fitting are utilized for the task (for a review, see e.g. Dumusque et al. 2017)

The efficiency of a radial velocity campaign can be evaluated by injecting simulated signals with known characteristics in the data and then running the analysis pipeline to recover the signal Howard and Fulton (2016). Figure 3.2 illustrates the efficiency for a given Doppler survey calculated in this way as a function of the planetary mass and semi-major axis. Indeed the noise level constrains the efficiency from below, while longer period planets cannot be detected with a finite duration campaign.

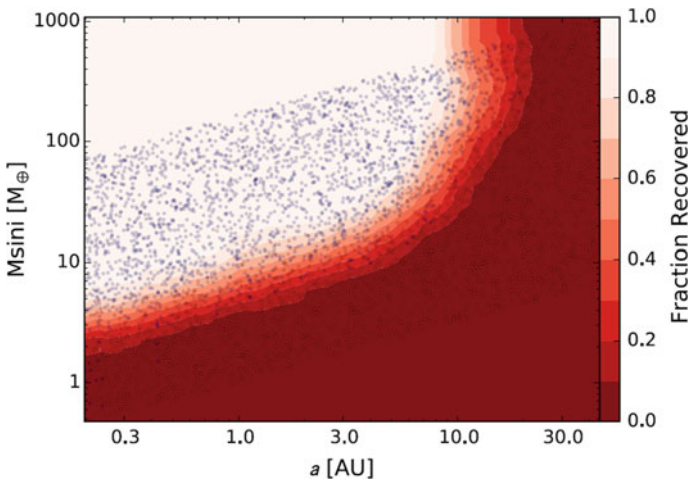

Fig. 3.2 Completeness of the RV sample of planets in a Doppler survey estimated by injection/recovery of simulated signals in the data

3.2.1.4 RV Surveys Highlights

Besides being the first method successfully employed for the detection of a planet around a normal star, the RV technique has also been able to provide the detection of the first multiple planetary systems (Butler et al. 1999), the detection of long-period planets (Howard et al. 2010a), and, enabled by $\mathrm{m\,s^{-1}}$-level precision, the discovery of the first low-mass planets, Neptunes and Super Earths (Lovis 2006; Mayor et al. 2009). Although next-generation spectrographs (e.g., ESPRESSO, Pepe et al. 2021; EXPRES, Jurgenson et al. 2016; for a review see Fischer et al. 2016) are approaching a nominal precision of $10\,\mathrm{cm\ s^{-1}}$, the main limitation comes from the modeling of stellar activity, which can easily produce RV signals with the dominant amplitude when compared to those of low-mass planets (Dumusque et al. 2017).

3.2.2 Transits

About 70% of the currently known exoplanets have been discovered by the transit method. Most of these discoveries come from the *Kepler* mission, to which we owe the possibility to speak in so great detail about the statistics of close-in exoplanets, but many ground-based surveys have contributed to the discovery of interesting systems.

3.2.2.1 Transit Geometry

As depicted in Fig. 3.3, planets on nearly edge-on orbits may transit in front of their parent star, blocking the light coming from an area corresponding to their projected disk. In a first approximation, the flux detected by the observer drops by a fraction

$$\delta \simeq \frac{R_\mathrm{p}^2}{R_\star^2}, \tag{3.6}$$

which means that, if we know the radius of the star by its position on the HR diagram, we can immediately infer the radius of the planet (Seager and Mallén-Ornelas 2003). More refined modeling of the transit light curve may take into account the limb darkening profile of the star (Mandel and Agol 2002), the thermal flux from the night side of the planet (Charbonneau 2003), oblateness (Carter and Winn 2010) and so on (Winn 2010; Perryman 2018).

In general, the planet will also pass behind the star. In this secondary eclipse, the light of the day-side of the planet is blocked, giving rise to a much shallower event that, when observed, preciously increases our knowledge on the planet, as it allows to further constrain the orbital eccentricity, but most importantly opens the door to measurements of the properties of its atmosphere (Deming et al. 2005).

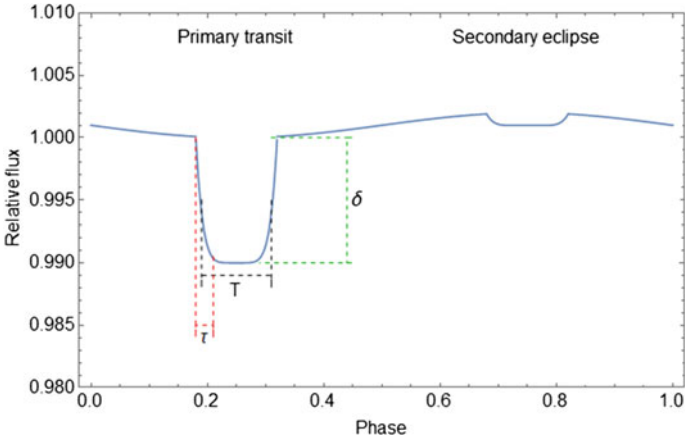

Fig. 3.3 Light curve of a system with a transiting planet. The primary transit (planet in front of the host star) is characterized by a duration T, a descent time τ and a deficit flux δ. The secondary eclipse occurs when the planet dayside light is blocked by the star

The direct observables in a transit are the orbital period P, the depth δ, the duration T and the time τ taken by the planet to cross the limb of the star (see also Chap. 4, Sect. 4.4). Simple formulae relate these to physical parameters such as the ratio of the radii $R_{\rm p}/R_\star$, the semi-major axis in units of the star radius $a/R_\star$, the impact parameter b, and the stellar density ρ_* (Seager and Mallén-Ornelas 2003). Finally, after the use of stellar models to derive the host star parameters, we may get $R_{\rm p}$, a and the orbital inclination i (for details, see e.g. Seager and Mallén-Ornelas 2003; Collier Cameron 2016).

If the host star is bright enough, spectroscopic follow-up with high-precision RVs and subsequent detection of the RV semi-amplitude can provide, combined with the i value from the transit, a determination of the true planet mass. For these precious planets, we can derive their bulk density and finally gain insights concerning their internal composition (see Sect. 3.4.3).

Transiting planets obviously orbit on nearly edge-on configurations. Assuming an isotropic distribution for the orbital planes, the probability that a generic planet on a circular orbit transits in front of its star is roughly (Borucki and Summers 1984)

$$P_{\rm tra} \approx \frac{R_*}{a} = 0.005 \left(\frac{R_*}{R_\odot}\right) \left(\frac{a}{1\,\mathrm{AU}}\right)^{-1} , \tag{3.7}$$

which means that we need to survey thousands of stars before finding one transiting planet. The probability decreases relatively fast with the orbital distance a, biasing the technique toward the detection of very close-in planets.

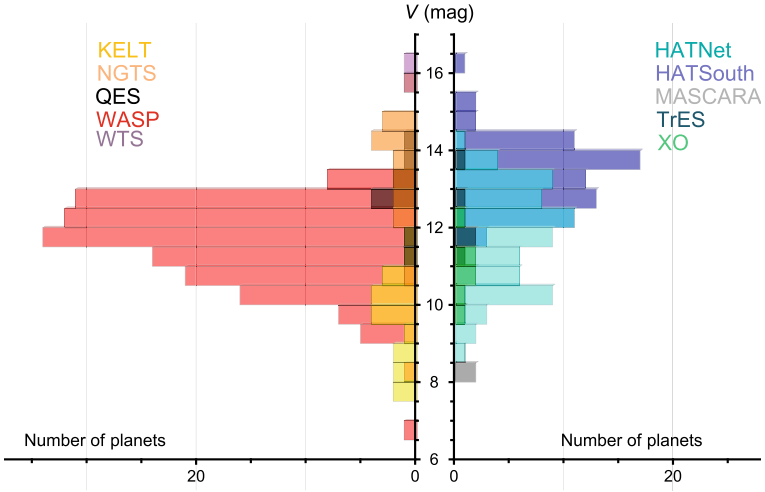

Fig. 3.4 Histograms of the number of planets detected by the most successful ground-based all-sky transit surveys versus host-star *V* mag. Data taken from the Transiting ExoPlanet Catalogue (TEPCat; www.astro.keele.ac.uk/jkt/tepcat) as of May 2021

3.2.2.2 Transit Campaigns and Analysis

Surveys for the discovery of transiting exoplanets typically monitor large fields in the sky with percent-level, high-cadence photometry. Ground-based surveys of F-G-K-type stars have often used arrays of wide-field cameras on the same mount. Here we mention HATNet (Bakos et al. 2004), WASP/SuperWASP (Pollacco et al. 2001; Wheatley 2015), OGLE (Udalski et al. 2002), TrES (Alonso et al. 2004), XO (McCullough et al. 2005), KELT (Pepper et al. 2007), MASCARA (Snellen et al. 2012), QES (Alsubai et al. 2013), HATSouth (Bakos et al. 2013), WTS (Kovács et al. 2013), NGTS (Wheatley et al. 2013). Note that depending on the details of the technical implementations, choices of exposure time and observing strategy, and camera sensitivity, all these surveys have differing sky coverages, limiting magnitudes for faint targets and a minimum magnitude for bright stars leading to saturation, translating into a broad visual magnitude distribution of the detected companions (see Fig. 3.4; for a review, see Collier Cameron 2016).

Other ground-based transit surveys (MEarth, Charbonneau et al. 2009; APACHE, Sozzetti et al. 2013; TRAPPIST, Gillon et al. 2012; ExTrA, Bonfils et al. 2015; SPECULOOS, Delrez et al. 2018; EDEN, Gibbs et al. 2020) have instead focused on late-type M and ultra-cool dwarfs, adopting a one (or few) target(s) per field approach and 40-cm to 1-m class telescope arrays. Such experiments exploit the possibility to reach detection of short-period transiting sub-Neptunes, super Earths, and even temperate Earth-sized, rocky planets from the ground with modest-size telescopes, which is enabled by the small radii of low-mass stars, leading to deep transits ($\Delta\text{mag} \gtrsim 0.005$ mag), and by the low temperatures of the primaries, lead-

ing to much closer-in habitable zones that those of solar-type stars, and therefore increased likelihood of observing transits of temperate planets.

Space-based transit photometry allows obtaining uninterrupted, high-cadence light curves that can reach better than 10^{-4} precision, which is the level required for detection of transits of Earth-sized planets across Sun-like stars. Figure 3.5 depicts the time progression of past, present and future transiting-planet space missions over a quarter-century. The first planetary transit discovery in space was made by CoRoT (Auvergne et al. 2009), which operated in the 2007–2013 time frame, but it was indeed with *Kepler* (Borucki 2016) that the field experienced a dramatic revolution. *Kepler* observed the same $10^\circ \times 10^\circ$ field on the Galactic plane between the Cygnus and Lyra constellations for 4 years (2009–2013), leaving us with more than 4000 transiting planet candidates. Most of them have either been statistically validated or confirmed as true planets via dynamical mass measurements. Even in its refurbished version (renamed K2) after the failure of the reaction wheels, the *Kepler* spacecraft continued (in the period 2014–2018) to deliver transiting candidates distributed all along the ecliptic plane (Vandenburg et al. 2016).

More recently the TESS mission, launched in 2018, is performing an all-sky survey of bright stars to look for transiting super-Earths and sub-Neptunes, particularly around late-type dwarfs (Ricker et al. 2015). TESS is designed to be a primary provider of bright transiting planets for spectroscopic follow-up measurements with JWST (Greene et al. 2016), which, due to launch in December 2021, is expected to provide an in-depth characterization of their atmospheres. The sample of bright transiting planets will also be the key input list for ESA's Ariel mission (launch expected in 2029), which is expected to survey ~ 1000 of them for the purpose of atmospheric characterization (Tinetti et al. 2018). CHEOPS (launched in 2019) is starting to observe known transiting planets to derive much more accurate radii (Broeg et al. 2013). Finally, PLATO (launch expected in 2026) is designed to monitor approximately 50% of the visible sky and discover Earth-like transiting planets in the habitable zone of Sun-like stars (Rauer et al. 2014).

Independent of the cadence and precision of the light curve, the search for planetary transits is prone to a large number of false positives, i.e. transit-like events caused by phenomena other than planetary transits. Astrophysical false positives are mostly produced by a variety of configurations of stellar systems (for details on the subject see e.g., Collier Cameron 2016).

Transit detection is performed by fitting a periodic box-like function (the Box Least Squares technique; Kovács et al. 2002) to the photometric time-series phase-folded over a large grid of trial frequencies. The frequency spectrum produced by the box-fitting algorithm is then inspected for identification of a statistically significant peak, corresponding to the period of the transit-like feature. Many sophisticated algorithms are then able to fit for the detailed shape of the transit light curve and retrieve the planet and stellar parameters. For more details, we direct the interested readers to the review by Collier Cameron (2016), and also the works by, e.g., Mandel and Agol (2002), Fulton et al. (2011), Eastman et al. (2013) and Southworth (2013).

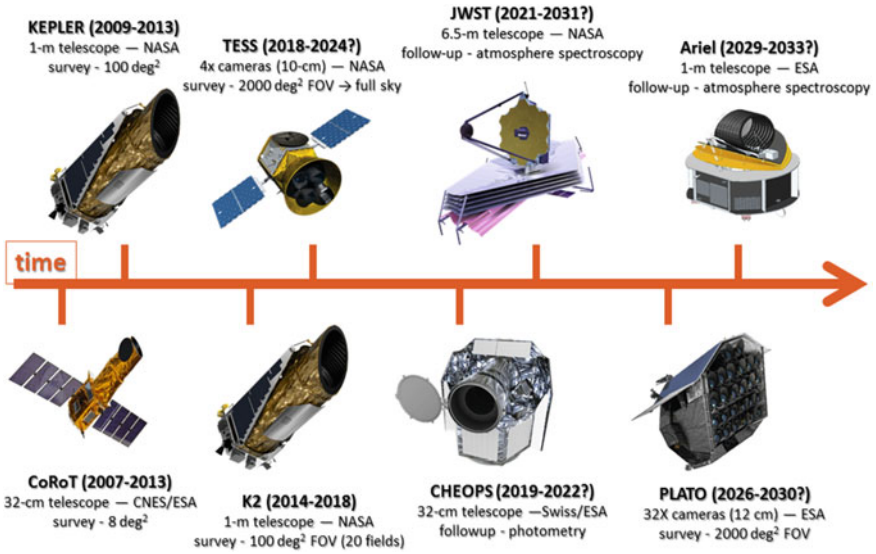

Fig. 3.5 Timeline of NASA and ESA space missions devoted to the detection and characterization of transiting exoplanets

3.2.2.3 Transit Surveys Highlights

The first discovered transiting exoplanet, HD 209458b (Henry et al. 1999; Charbonneau et al. 2000), was a typical hot Jupiter, and provided the final proof that the Doppler-detected companions since 1995 were, in fact, exoplanets. Ground-based transit photometry allowed to discover GJ 436b, the first Neptune-sized planet (Butler et al. 2004; Gillon et al. 2007), and GJ 1214b, the first transiting Super Earth orbiting a low-mass star (Charbonneau et al. 2009). However, in order to find the first bona-fide rocky planets (CoRoT-7b, Kepler-10b), space missions were needed (Léger et al. 2009; Batalha et al. 2011). *Kepler* has been able to find hundreds of multi transiting-planet systems (see Sect. 3.5), containing up to six planets within Mercury's orbit, like Kepler-11 (Lissauer et al. 2011a). *Kepler* also unveiled a class of transiting giant planets orbiting short-period eclipsing binaries, i.e. circumbinary planets, Kepler-16b being the first of its kind (Doyle et al. 2011. For a review see Welsh and Orosz 2018). Besides, ground-based surveys have continued to provide spectacular results, such as the TRAPPIST-1 multi-planet system (Gillon et al. 2017), composed of 7 transiting Earth-sized, Earth-mass planets orbiting an ultra-cool dwarf. Probably three of these planets lie in the habitable zone and may harbor water on their surface. Finally, transiting exoplanets have allowed us to enter the era of atmospheric characterization of close-in planets orbiting main-sequence stars (see, e.g., the review by Sing 2018).

3.3 Mass, Size, and Period Distributions

Modern Doppler and transit surveys have shown the prevalence of planets at short and intermediate separations, which we will operationally define here as having a semi-major axis $a < 5$ au. The RV method has driven the field during its first decade of development, while ground-based and space-borne transit surveys (CoRoT, *Kepler*) have provided a major boost in the second decade. The initial focus of such investigations was on the discovery of new exoplanets and on improving the surveys' sensitivities in order to expand the region of accessible parameter space. When the sample of detected planets in individual surveys became large enough, the first statistical analyses were performed.

The basic aim of such studies was to determine *a*) the intrinsic frequency of stars with planets or *b*) the mean number of planets per star. These are two ways of determining occurrence rates of exoplanets having properties (such as mass, radius, and orbital distance) within a specified range. The key calculation to perform is the following:

$$\text{Occurrence Rate} = \frac{\#\,\text{planets}}{\#\,\text{stars}}\,, \tag{3.8}$$

where # planets is the number of detected planets in the survey that have the stipulated properties and # stars is the number of stars in the survey for which such planets could have been detected. This is however not a trivial task, as an accurate measurement of occurrence rate requires a large sample of stars that have been searched for planets and the proper understanding of observational biases/selection effects that favor the discovery of certain types of planets. For instance, in the representation of Fig. 3.6 one can appreciate how the most sensitive transit survey to-date, the *Kepler* mission, can discover planets with a very wide range of planetary radii up to a separation of about 1 au, beyond which it is essentially blind. Conversely, the Doppler domain can

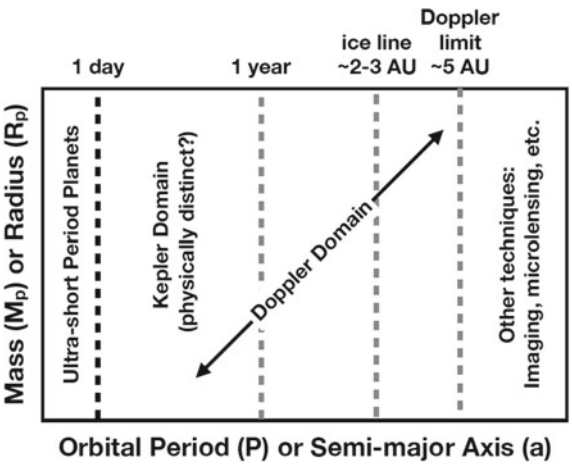

Fig. 3.6 Relevant domains of planet detection techniques in the mass (o radius) versus orbital period (or semi-major axis) parameter Space. Figure showed by A. Howard in May 2019 during his lecture

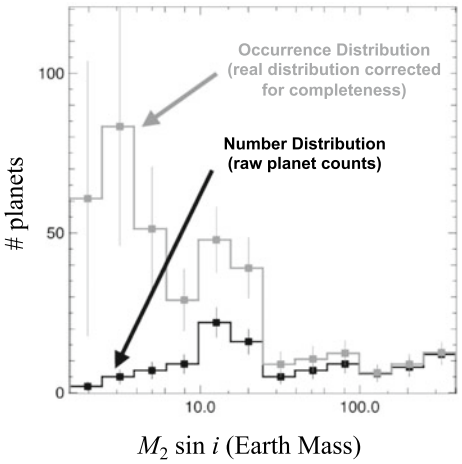

Fig. 3.7 The observed histogram (black line) of planetary masses compared with the equivalent histogram after correcting for the detection bias (gray line). Figure adapted from Mayor et al. (2011)

extend to significantly larger semi-major axes, but with variable sensitivity in terms of accessible mass range.

In order to effectively compute occurrence rates, the strategy to adopt includes modeling all effects, which cause planets to be missed during the detection process, and correct for those as much as possible, so that remaining errors are small compared to counting statistics. This implies achieving the best-possible understanding of the underlying observational biases/selection effects that affect a survey's completeness. In this way one moves from a measurement of raw planet counts (number distribution) to a representation of the true underlying distribution (see Fig. 3.7). When biases are not sufficiently well-understood, one is expected to honestly, clearly state caveats and limitations of the performed analyses.

In the remainder of this Section we will focus on understanding how occurrence is computed and then discuss major trends in occurrence at short and intermediate separations for Doppler-detected and transiting planets, using mass, size, and orbital period/semi-major axis as proxies of the accessible parameter space.

3.3.1 Doppler Surveys

The results from three major Doppler surveys have been used to address the issue of planet occurrence around F-G-K-type stars in the solar neighborhood ($d \lesssim 30$ pc). The analysis of the Keck RV survey, which was performed by Cumming et al. (2008), included 475 F-G-K dwarfs monitored for about 8 years and found to host a total of 48 planets (including confirmed companions and candidates). Cumming et al. (2008) determined the completeness-corrected occurrence rate of giant planetary companions with minimum mass in the range $0.3\,M_{\rm Jup} < m_{\rm p} \sin i < 10\,M_{\rm Jup}$ and orbital period $P < 2000$ days. Limits on companion detectability were determined based

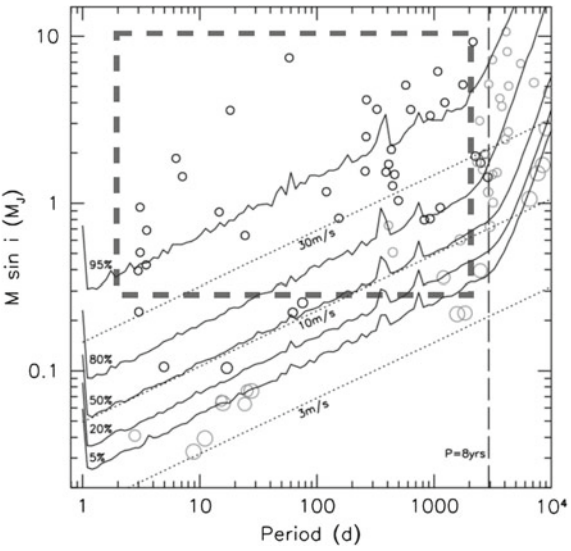

Fig. 3.8 Giant-planet occurrence based on the Keck survey consisting of 475 FGK-dwarf stars. Figure adapted from Cumming et al. (2008), © The Astronomical Society of the Pacific. Reproduced by permission of IOP Publishing. All rights reserved

on a Lomb-Scargle (Lomb 1976; Scargle 1982) periodogram analysis to identify significant periodicities in the RV time-series. Signals with given RV amplitude K and P producing a false-alarm probability (FAP; Horne and Baliunas 1986) below 10^{-3} were considered as detections and the fraction of stars, for which such an instance occurred, recorded. Any detected RV amplitude K was transformed into a corresponding minimum companion mass by inverting Eq. 3.2. Cumming et al. (2008) found that companions with $K > 30$ m s^{-1} would have been detected around most of the stars in their sample. Corrections for incompleteness became important to characterize the loss in sensitivity below that threshold. This was done in practice by computing a missed planet correction factor $F(P,\ m_{\rm p} \sin i)$ for each detected planet (both confirmed and candidates). If in a given region of the mass-period plane, planets can be ruled out for a fraction C of stars, the best estimate of the number of planets is $1/C$ times the number of detections, and $1/C$–1 planets remain undetected. The corresponding completeness-corrected map produced by Cumming et al. (2008) is shown in Fig. 3.8.

Cumming et al. (2008) then employed a maximum likelihood technique to fit a simple power-law function to the exoplanet minimum mass-period distribution, finding:

$$\frac{dN}{d\log m_{\rm p} \sin i\, d\log P} = C(m_{\rm p} \sin i)^{\alpha} P^{\beta} \propto (m_{\rm p} \sin i)^{-0.31\pm0.20} P^{0.26\pm0.10}. \quad (3.9)$$

The normalization constant was chosen such that $\sim 10\%$ of solar-type stars host at least one planet with mass and period in the above range. This functional form to represent the occurrence rate of planets eventually became a benchmark for many

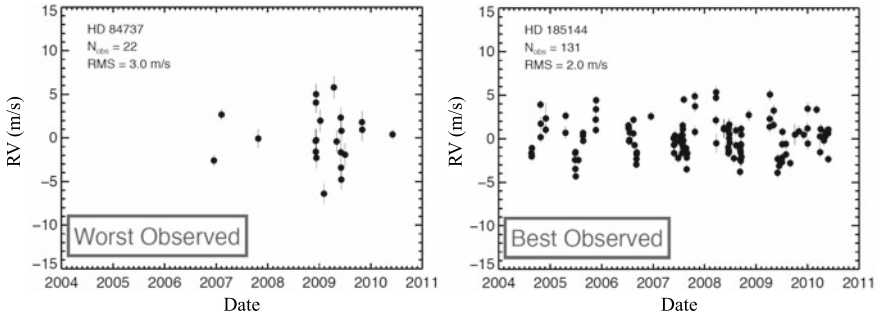

Fig. 3.9 Examples of RV time-series for targets in the Keck Eta-Earth survey with sparse and dense sampling of the observations (left and right panel, respectively). Figure showed by A. Howard in May 2019 during his lecture

subsequent studies.[2] The mass and period power-law coefficients indicate that small-mass planets are more common, and longer-period planets are more common. Cumming et al. (2008) also extrapolated the occurrence rate of giant planets at wider separations, estimating that $\sim 20\%$ of solar-type stars host a giant planet with mass $> 0.3\,M_{\rm Jup}$ within 20 au.

The period distribution studied by Cumming et al. (2008) showed additional structure, not directly captured by the power-law fits. They found evidence of a pile-up of hot Jupiters (gas giants operationally defined as having $P < 10$ days) at $P \simeq 3$ days, followed by a 'period valley' of lower probability in the approximate period range $10 - 100$ days, and then by a sharp rise in occurrence for separations $a \gtrsim 1$ au. These findings are entirely in line with those first discussed by Udry et al. (2003). In the Keck RV survey, the fraction of F, G, and K dwarfs in the solar neighborhood hosting hot Jupiters was found to be $1.5\% \pm 0.6\%$, a number in line with those later obtained by Mayor et al. (2011), using CORALIE and HARPS data ($0.89\% \pm 0.36\%$), and by Wright et al. (2012), based on data from the Keck and Lick observatories ($1.2\% \pm 0.38\%$).

The Keck Eta-Earth survey (Howard et al. 2010b) and the CORALIE+HARPS survey (Mayor et al. 2011) provided the first opportunity to explore the domain of low-mass (3–30 $M_\oplus$) planets with periods $\lesssim 50$ days. The two programs surveyed 166 G-K-M dwarfs and 376 G-K dwarfs, respectively. Most of the stars in both samples were selected based on low levels of chromospheric activity, allowing to achieve a typical *rms* dispersion in the Keck Eta-Earth and CORALIE+HARPS RV datasets of $2 - 4\,{\rm m\,s^{-1}}$ and $1 - 3\,{\rm m\,s^{-1}}$, respectively. Figure 3.9 shows detection limits for two individual objects with low and high cadence RV observations in the Keck Eta-Earth survey.

The two surveys achieved comparable sensitivity to close-in planets with $P < 50$ days (an example is shown in Fig. 3.10), and when accounting for the high degree of incompleteness (10%–30%) for minimum masses in the super-Earth regime ($m_{\rm p} \sin i < 10\,M_\oplus$), the findings from both experiments provide a convergent picture:

[2] More details on the mathematical formalism of the technique are provided in Sect. 2 of Chap. 4.

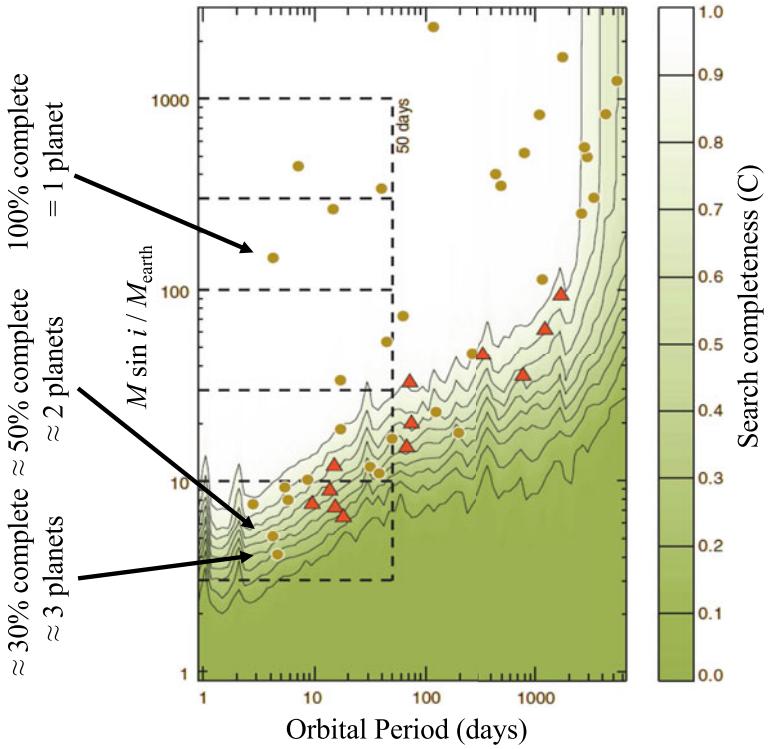

Fig. 3.10 Minimum mass versus orbital period for the detected (yellow circles) and candidate planets (FAPs $\sim 1-5\%$; red triangles) from the Eta-Earth survey. Contours refer to the *search completeness*, that is the fraction of stars with enough RV measurements to be sensitive to planets in circular orbits of a given orbital period and minimum mass. Dashed lines refer to five different mass domains out to 50 day orbits. The arrows identify high, intermediate, and low completeness. Figure adapted from Howard et al. (2010b) and reproduced with permission from A. Howard

the planet mass function rises steeply towards lower-mass planets, such that the occurrence of planets with $3\,M_\oplus \lesssim m_\mathrm{p} \sin i \lesssim 30\,M_\oplus$ is found to be around 20%–25%.[3] These planets are at least an order of magnitude more common than giant planets in the same period range around solar-type stars. The results from both surveys were also broadly consistent in indicating a lack of hot Neptunes ($10\,M_\oplus \lesssim m_\mathrm{p} \sin i \lesssim 30\,M_\oplus$) with $P < 10$ days, a population otherwise conspicuous at longer periods.

The findings of the Keck Eta-Earth and CORALIE+HARPS surveys were at the time very informative for planet formation theory. Early attempts at producing models of synthetic planet populations (e.g., Ida and Lin 2005, 2008; Mordasini et al. 2009a, b) predicted a "planet desert" in the super-Earth mass domain for $P < 50$ days or so, precisely where the two programs determined the highest val-

[3] Similar findings were also presented by Wittenmyer et al. (2011), who reported that 17.4% of stars host a planet with $m_\mathrm{p} \sin i < 10\,M_\oplus$ and $P < 50$ days.

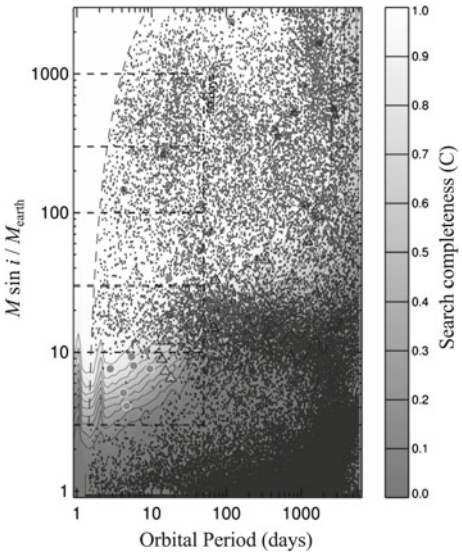

Fig. 3.11 A population-synthesis model superimposed on the plot shown in Fig. 3.10. Figure adapted from Mordasini et al. (2009b) and Howard et al. (2010b) and showed by A. Howard in May 2019 during his lecture

ues of completeness-corrected planet frequency (see Fig. 3.11). The observational evidence put forth motivated significant improvements in population synthesis models of planet formation (e.g., Ida and Lin 2010, 2013; Mordasini et al. 2012a, b, c; Paardekooper et al. 2011, 2013).

At intermediate separations, the Eta-Earth and CORALIE+HARPS surveys confirmed the trend of increasing frequency of giant planets with increasing orbital period, up to $\sim$ 5 year ($\sim$ 3 au). This roughly corresponds to the location of the snow line in protoplanetary disks around solar-type stars (e.g., Mulders et al. 2015b; Morbidelli et al. 2016). Beyond 3 au or so, the agreement of Doppler surveys appears to degrade sharply with orbital separation. Recent studies indicate the presence of a decline in giant planet occurrence with increasing separation (Fernandes et al. 2019), others (Wittenmyer et al. 2020) find no evidence of a turnover in giant planet frequency at the snowline (see top and bottom panels of Fig. 3.12), and in general observational uncertainties (e.g., sample sizes and their exact definition in terms of mass interval, survey duration, sampling) do not allow yet achieving consensus on the exact regime of orbital separations at which the occurrence rate of gas giants might start declining as well as its possible dependence on planetary mass (Fulton et al. 2021). The connection between occurrence rates at close-in, intermediate and wide separations is further discussed in Chap. 4 (Sect. 5).

Finally, a large number of investigations has used the results from the above-mentioned RV surveys and other Doppler programs to explore the dependence of planet occurrence on stellar properties. In particular, giant planet frequency increases sharply with increasing stellar metallicity for F-G-K dwarfs (Santos et al. 2004b; Fischer and Valenti 2005; Sozzetti et al. 2009; Mortier et al. 2012), while whether small-planet occurrence correlates positively with metallicity in the same stellar samples is still a matter of debate (Sousa et al. 2008; Courcol et al. 2016; Sousa et al.

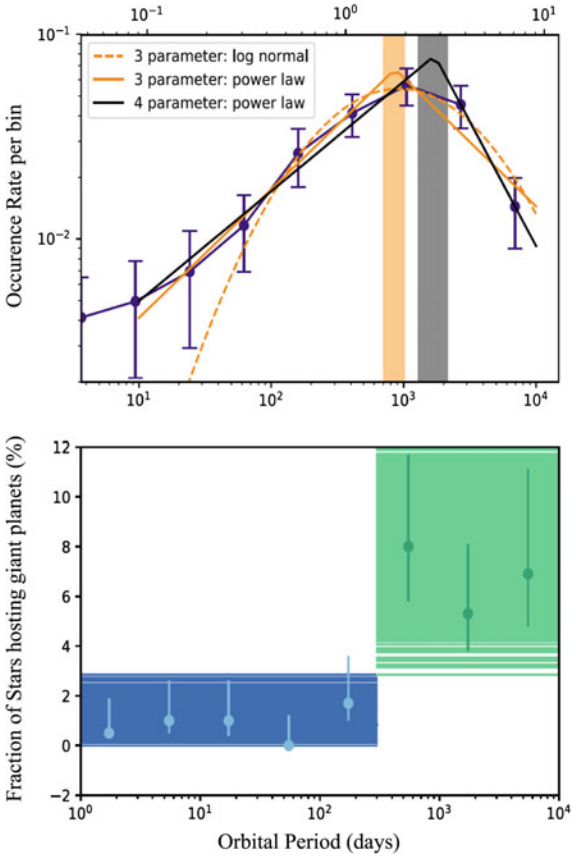

Fig. 3.12 *Top*: occurrence rate of 0.1–20 $M_{\rm Jup}$ planets (purple) with best-fit relations beyond 10 days: asymmetric broken power law (solid black line), symmetric broken power law (solid yellow line), and log-normal (dotted yellow line). The location of the *break* is shown as a shaded region (gray for the asymmetric broken power law and yellow for the other two fits). Figure adapted from Fig. 3 of Fernandes et al. (2019) and reproduced with permission from R. Fernandes. *Bottom*: frequency of giant planets as a function of orbital period. Figure adapted from Fig. 1 of Wittenmyer et al. (2020)

2019; Bashi et al. 2020). The occurrence rate for giant planets within 3 au increases with host star mass up to $\sim 2\,M_{\odot}$ (Johnson et al. 2010; Reffert et al. 2015; Ghezzi et al. 2018), with low-mass M dwarfs hosting as few as 3–10 times less Jovian mass companions than solar-type stars (e.g., Butler et al. 2004; Endl et al. 2006; Bonfils et al. 2013; Tuomi et al. 2014). On the contrary, the occurrence rate of close-in super Earths around M dwarfs could be higher than that for F-G-K stars by a factor of 2–3 (Bonfils et al. 2013) and it presents weak or no correlation with mass and metallicity, respectively (Maldonado et al. 2020). The theoretical interpretation of the above trends in terms of planet formation and evolution processes and models is provided in Chap. 1.

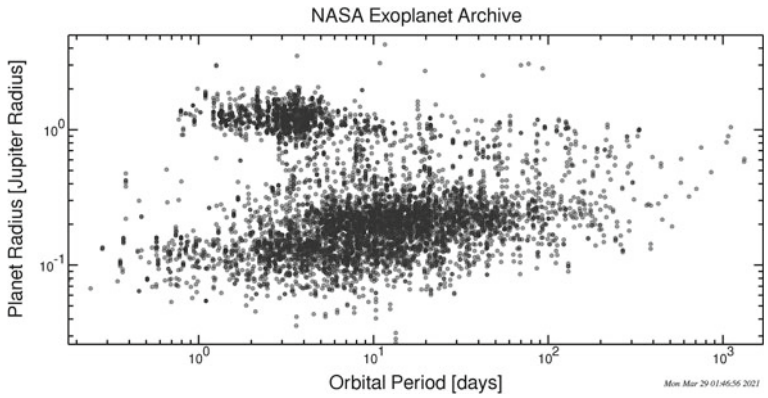

Fig. 3.13 The diagram of planet radius versus orbital period for the exoplanets belonging to the *Kepler* sample. The error bars have been suppressed for clarity. Data were taken from the NASA Exoplanet Archive in March 2021

3.3.2 Transit Surveys

The *Kepler* mission sample of thousands of transiting planet candidates (see Fig. 3.13) has enabled a large number of analyses aimed at determining the occurrence rates of planets with radii as small as 1 $R_\oplus$, and at correlating planet occurrence estimates in the *Kepler* field with stellar properties (e.g., Howard et al. 2012; Fressin et al. 2013; Petigura et al. 2013a, b; Dressing and Charbonneau 2013, 2015; Burke et al. 2015; Foreman-Mackey et al. 2015; Fulton et al. 2017; Fulton and Petigura 2018; Zhu and Wu 2018; Narang et al. 2018; Mulders et al. 2018; Petigura et al. 2018; Hardegree-Ullman et al. 2019; Hsu et al. 2019; Berger et al. 2020; Bryson et al. 2020a, b; Lu et al. 2020; Yang et al. 2020).[4]

With time, the sophistication of the approaches to the analysis of *Kepler* data for the purpose of occurrence rate calculation has increased. Most of the effort has been devoted to the improved characterization of both completeness and reliability against false alarms of the content of the *Kepler* catalog of candidates. The first studies utilized simple Gaussian cumulative distribution functions, or their linear approximations, as proxies for pipeline completeness, or identified restricted samples with an assumed high degree of completeness. These approaches evolved further into using Poisson-likelihood-based calculations and approximate Bayesian computations that took advantage of the most significant effort to characterize the reliability of the *Kepler* planet candidates catalog realized in the final DR25 catalog paper (Thompson et al. 2018). The interested reader can find additional details on the difficulties inherent to accurate occurrence rate calculations (using the *Kepler* survey as a guiding example) in Sect. 3 of Chap. 4. We will focus here on the methodological approach

[4] A non-exhaustive list of of planet occurrence rate papers, heavily focused on the analysis of *Kepler* mission data, can be found at exoplanetarchive.ipac.caltech.edu/docs/occurrence_rate_papers.html.

of Howard et al. (2012), who provided the first such estimate for transit candidates within 0.25 au of solar-type stars, matching the period range of Howard et al. (2010b) analysis based on Doppler data.

Howard et al. (2012) adopted a carefully crafted strategy to effectively use Eq. (3.8) in the occurrence rate calculation. At the time, the Gaia mission had yet to provide direct distance estimates for the overwhelming majority of stars in the *Kepler* field, so they made careful cuts in effective temperature ($4100\,\mathrm{K} < T_{\mathrm{eff}} < 6100\,\mathrm{K}$) and surface gravity ($4.0 < \log g < 4.9$), and selected only bright stars with *Kepler* bandpass magnitudes $K_{\mathrm{p}} < 15\,\mathrm{mag}$, so as to ensure sufficient photometric precision for transit signal detectability. Similarly, transit candidates were selected based on a high threshold in terms of signal-to-noise ratio (S/N) of the detection:

$$\mathrm{S/N} = \frac{\delta}{\sigma_{\mathrm{CDPP}}}\sqrt{\frac{n_{\mathrm{tr}}\,T_{\mathrm{dur}}}{3\,\mathrm{hr}}} \tag{3.10}$$

where δ is from Eq. 3.6, n_{tr} is the number of transits observed by *Kepler* in a 90-day quarter, T_{dur} is the transit duration (see Eq. 3.15), σ_{CDPP} is the Combined Differential Photometric Precision, i.e. the empirical rms noise in 3-hr time interval bins coming from the *Kepler* pipeline. The transit candidates where selected so as to have $R_{\mathrm{p}} > 2\,R_{\oplus}$, $P < 50\,\mathrm{days}$, and $\mathrm{S/N} > 10$, substantially a regime of nearly complete detection efficiency, with minimal pollution ($\sim 5\%$) from false positives. The top panel of Fig. 3.14 shows the final selection of candidates made by Howard et al. (2012).

The occurrence rate calculation was performed on a grid of cells in logarithmically spaced intervals of orbital period and radius. If $n_{\star}$ is the number of stars around which that planet could have been detected with $\mathrm{S/N} > 10$, and $p_{\mathrm{tr}} = R_{\star}/a$ is the geometric transit probability, then the average occurrence rate of planets within a cell is:

$$f_{\mathrm{cell}} = \sum_{j=1}^{n_{\mathrm{pl,cell}}} \frac{1/p_{\mathrm{tr},j}}{n_{\star,j}}, \tag{3.11}$$

where the sum is over all detected planets within the cell. The actual planet count is thereby augmented taking into account that for each detected planet there are actually $1/p_{\mathrm{tr}}$ planets in all orbital inclinations orbiting $n_{\star}$ stars. The bottom panel of Fig. 3.14 shows the result of the full occurrence rate calculation, color-coded in terms of occurrence per logarithmic area units ($\frac{\mathrm{d}^2 f}{\mathrm{d}\log P\,\mathrm{d}\log R_{\mathrm{p}}}$).

The distribution of planet occurrence provides crucial clues on planet formation, migration, and evolution processes. Summing occurrence over all periods in the various radius bins, the top panel of Fig. 3.15 shows occurrence as a function of planet radius, modeled with a power-law of the form $df/d\log R_{\mathrm{p}} = kR^{\alpha}$, with $k = 2.9 \pm 0.5$ and $\alpha = -1.92 \pm 0.11$. Quite clearly, planet occurrence increases with decreasing planet radius. This is qualitatively in agreement with the power-law dependence of the planet mass function found by Howard et al. (2010b), albeit with a significantly steeper dependence on radius. The bottom panel of Fig. 3.15

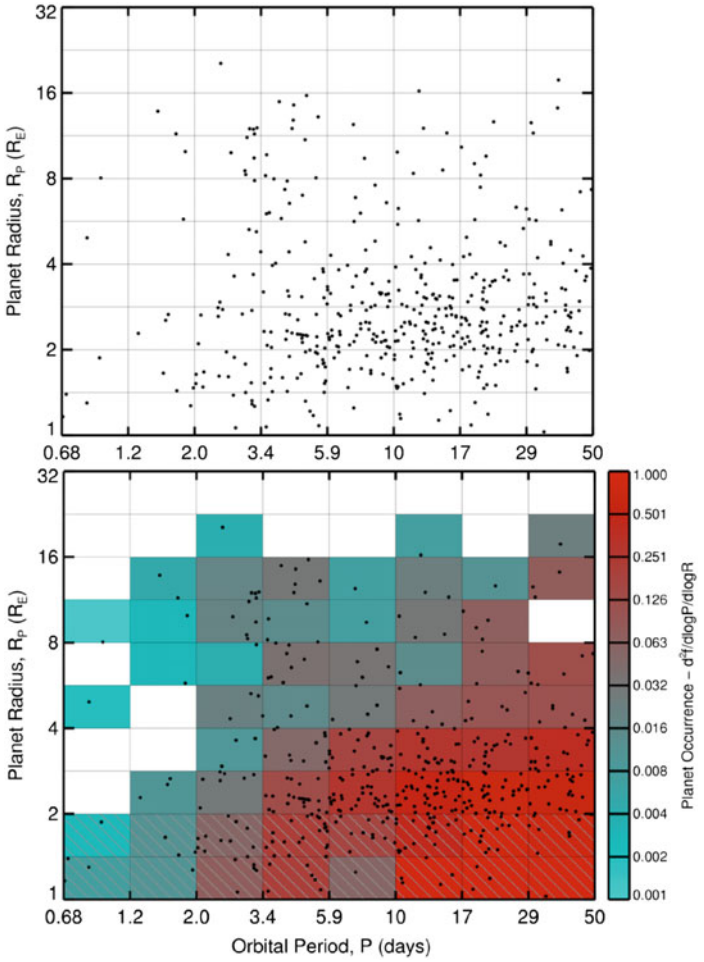

Fig. 3.14 *Top*: planet radius versus orbital period for the *Kepler* transit candidates with $P < 50$ days. it Bottom: planet occurrence in the radius-orbital period plane for solar-type stars from *Kepler*. See text for details. Figures adapted from Howard et al. (2012) and reproduced with permission from A. Howard

shows instead the measured planet occurrence as a function of orbital period using power-law fits with exponential cutoffs below a characteristic period P_0 in the form:

$$\frac{dN}{d\log P} = kP^{\beta}\left(1 - e^{-(P/P_0)^{\gamma}}\right) . \tag{3.12}$$

Planet occurrence increases with $\log P$ for all planet classes considered ($\beta > 0$), while P_0 increases with decreasing planet radius, suggesting that the migration and parking mechanism that deposits planets close-in depends on planet radius.

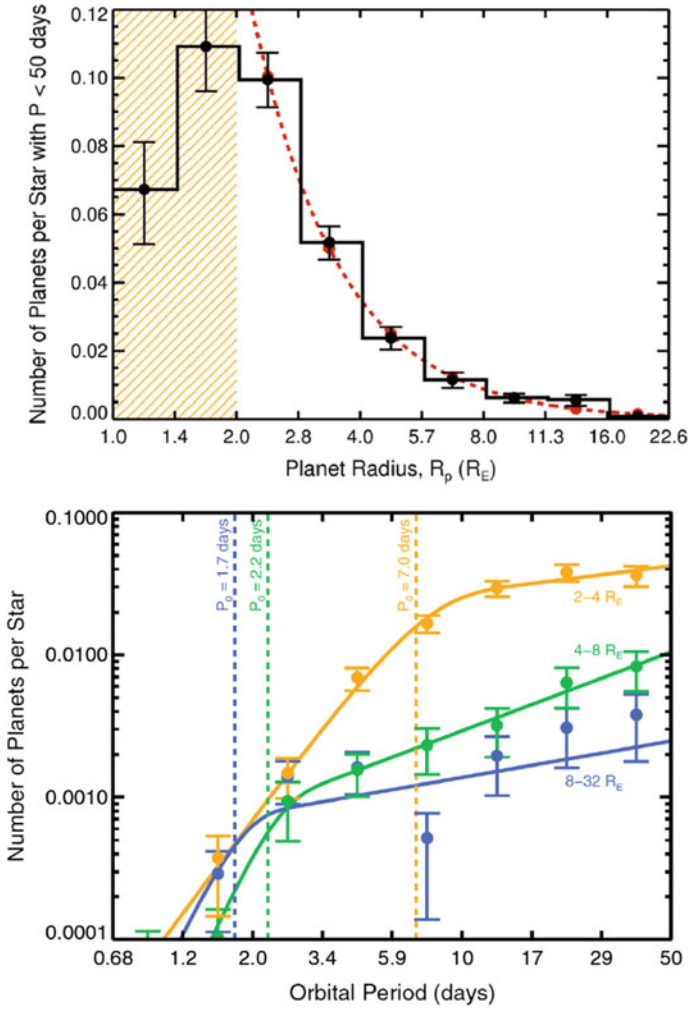

Fig. 3.15 *Top*: histogram of planet occurrence as a function of planet radius for planets with $P_{\rm orb} <$ 50 days. The dashed line represents a power-law fit to occurrence measurements. In particular, $df/d\log R_{\rm p} = kR_{\rm p}^{\alpha}$, with $k = 2.9 \pm 0.5$ and $\alpha = -1.92 \pm 0.11$. *Bottom*: the filled circles represent the measurements of planet occurrence as a function of the orbital period with best-fitting models superimposed. Figures adapted from Howard et al. (2012) and reproduced with permission from A. Howard

Finally, Howard et al. (2012) extended the occurrence rate calculation to include cooler and hotter stars beyond the G-K dwarf sample initially selected, to unveil a clear trend of increasing close-in planet frequency within decreasing $M_{\star}$, which was fitted with a linear relation as a function of $T_{\rm eff}$:

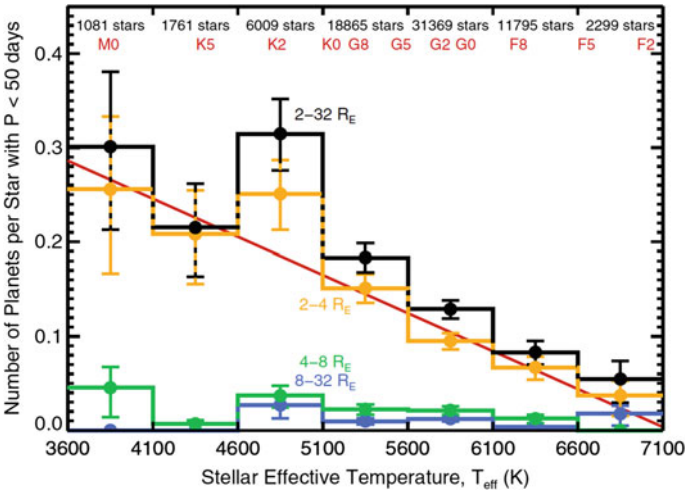

Fig. 3.16 Planet occurrence as a function of stellar effective temperature. Figure taken from Howard et al. (2012) and reproduced with permission from A. Howard

$$f = f_0 + k_T \left(\frac{T_{\rm eff} - 5100\,{\rm K}}{1000\,{\rm K}} \right) . \tag{3.13}$$

The trend in occurrence (shown in Fig. 3.16) is produced entirely by the population of super Earths and Neptunes with $R_{\rm p} < 8\,R_\oplus$, while for $R_{\rm p} > 8\,R_\oplus$ the opposite trend is recorded, in agreement with the findings from Doppler surveys of increasing giant planet frequency with stellar mass.

The findings by Howard et al. (2012) were extended to radii below $2\,R_\oplus$ and $P >$ 50 days in a follow-on study by Petigura et al. (2013b). They utilized an independent pipeline for transit candidates identification, a larger extent of *Kepler* photometry, partial reconnaissance spectroscopy of the primary stars and the same Howard et al. (2012) methodology to eventually estimate that $26 \pm 3\%$ of Sun-like stars harbor an Earth-size planet ($1 - 2\,R_\oplus$) with $P = 5$–100 days (see Fig. 3.17). They produced an extrapolation of the occurrence rate of such companions to the $P = 200$–400 days range (none was directly detected), corresponding to planets that receive stellar flux comparable to Earth, and derived a first reliable estimate of the frequency of Earth-like planets: $\eta_\oplus = 5.7^{+1.7}_{-2.2}\%$.

The large body of works on global occurrence rate calculations and trends with stellar properties in the *Kepler* field, which appeared since the Howard et al. (2012) and Petigura et al. (2013b) analyses, has broadly confirmed the fact that planets of increasingly smaller size and longer period are increasingly more common (e.g., Dong and Zhu 2013; Fressin et al. 2013; Batalha 2014; Burke et al. 2015). However, differences in the assumptions underlying the baseline occurrence rates (e.g., detection and vetting completeness, characterization of false alarms and astrophysical false positives, choice of the parent stellar population) can translate into significant

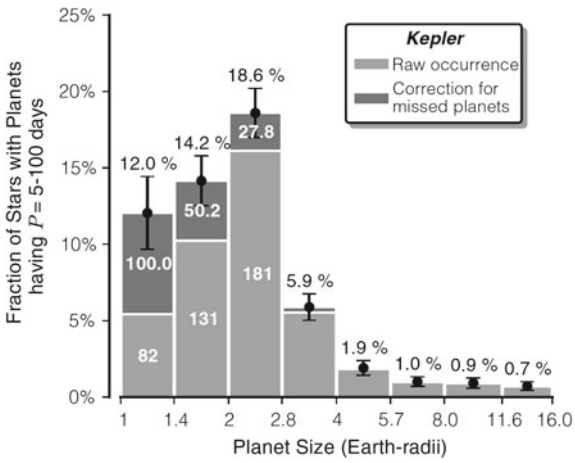

Fig. 3.17 The measured distributions of planet sizes for $R_p > 1\ R_\oplus$ and $P_{orb} = 5 - 100$ days. The first three bars are annotated to reflect the number of planets detected (light-gray bars) and missed (dark-gray bars). Figure adapted from Petigura et al. (2013b), ©2013—National Academy of Sciences

differences in terms of the specific numbers for different types of planets orbiting different types of stars (the reader can find additional details on such issues in Chap. 4, Sect. 3).

For example, while the trend of increasing planet frequency with decreasing stellar mass is not in doubt, absolute values and strength of the dependence measured by the different authors do not necessarily agree with each other (e.g., Foreman-Mackey et al. 2014; Dressing and Charbonneau 2015; Mulders et al. 2015a; Silburt et al. 2015; Mulders et al. 2018; Narang et al. 2018; Hsu et al. 2019; Hardegree-Ullman et al. 2019; Yang et al. 2020). Even more open for debate is the possible dependence of occurrence rates of small planets in the *Kepler* field with stellar metallicity (e.g., Buchhave et al. 2012, 2014; Buchhave and Latham 2015; Wang and Fischer 2015; Zhu et al. 2016; Petigura et al. 2018; Wilson et al. 2018; Zhu 2019; Lu et al. 2020), which as we have seen is still an open issue also for Doppler surveys. As for the much sought-after $\eta_\oplus$ estimate, increasingly sophisticated attempts to constrain it have been produced in recent times. When robust corrections for completeness and reliability are included, this value appears to be constrained to lie in the approximate range 5-50%, the dominant source of uncertainty being the virtual lack of true detections in the relevant parameter space. Table 3.1 summarizes the state of affairs of Earth-like planets occurrence rates.

A key aspect of the occurrence rate calculations based on *Kepler* data is that the use of a simple product of power laws in period and radius when modeling exoplanet population statistics appears as a sub-optimal choice. This was already apparent in Howard et al. (2012), Fressin et al. (2013), and Petigura et al. (2013a), where a power law was a poor fit to the observed planet population as a function of radius. In particular, additional structure in the radius distribution for $R_p \lesssim 3.0\ R_\oplus$ was smeared in those early studies due to the large uncertainties (typically 40%) in the stellar radii. The combination of spectroscopically-determined radii based on data collected as part of the California-Kepler Survey (CKS; Petigura et al. 2017) and the availability

Table 3.1 Rates of occurrence of habitable-zone Earth-like planets as measured by several authors

Planet type (planet-radius range in $R_\oplus$)	$\eta_\oplus$ (planets per star)	Reference	Notes
0.5–1.5	$0.37^{+0.48}_{-0.21}$–$0.60^{+0.90}_{-0.36}$	Bryson et al. (2021)	FGK dwarfs[a]
0.5–1.5	$0.58^{+0.73}_{-0.33}$–$0.88^{+1.28}_{-0.51}$	Bryson et al. (2021)	FGK dwarfs[b]
0.75–1.5	$0.13^{+0.09}_{-0.06}$–$0.11^{+0.07}_{-0.05}$	Kunimoto and Matthews (2020)	G dwarfs[a,b]
0.5–1.5	$0.302^{+0.181}_{-0.113}$	Bryson et al. (2020a)	GK dwarfs[a,c]
0.5–1.5	$0.126^{+0.095}_{-0.055}$	Bryson et al. (2020a)	GK dwarfs[a,d]
0.7–1.5	$0.11^{+0.06}_{-0.04}$	Pascucci et al. (2019)	FGK dwarfs[a,f]
0.7–1.5	$0.05^{+0.07}_{-0.03}$	Pascucci et al. (2019)	FGK dwarfs[a,g]
0.75–1.5	$0.33^{+0.10}_{-0.12}$	Hsu et al. (2020)	M dwarfs[a]
0.75–1.5	$0.04 - 0.40$	Hsu et al. (2019)	GK dwarfs[e]
0.85–1.4	0.33	Hsu et al. (2019)	GK dwarfs[a]
0.72–1.7	0.34 ± 0.02	Zink and Hansen (2019)	G dwarfs[a]
1.0–1.5	$0.41^{+0.29}_{-0.12}$	Hsu et al. (2018)	GK dwarfs[h]
1.0–1.5	$0.31^{+0.02}_{-0.03}$	Garrett et al. (2018)	G dwarfs[a]
0.5–1.5	$0.88^{+0.04}_{-0.03}$	Garrett et al. (2018)	G dwarfs[a]
0.5–1.0	$0.215^{+0.148}_{-0.099}$	Kopparapu et al. (2018)	G dwarfs[i]
1.0–1.75	$0.145^{+0.071}_{-0.0.061}$	Kopparapu et al. (2018)	G dwarfs[j]
0.7–1.5	0.36 ± 0.14	Mulders et al. (2018)	G stars[a]
1.0–1.5	$0.16^{+0.17}_{-0.07}$	Dressing and Charbonneau (2015)	M dwarfs[a]
1.5–2.0	$0.12^{+0.10}_{-0.05}$	Dressing and Charbonneau (2015)	M dwarfs[a]
1.0–1.5	$0.21^{+0.08}_{-0.08}$	Burke et al. (2015)	G dwarfs[k]
0.5–1.5	$0.50^{+0.40}_{-0.20}$	Burke et al. (2015)	G dwarfs[k]
1.0–2.0	$0.064^{+0.034}_{-0.011}$	Silburt et al. (2015)	FGK dwarfs[l]
0.6–1.7	$0.017^{+0.018}_{-0.009}$	Foreman-Mackey et al. (2014)	G dwarfs[a]
1.0–2.0	0.00059	Schlaufman (2014)	G stars[m,n]
1.0–2.0	$0.057^{+0.022}_{-0.017}$	Petigura et al. (2013b)	G stars[m]
0.5–1.4	$0.15^{+0.13}_{-0.06}$	Dressing and Charbonneau (2013)	M dwarfs[a]
0.5–1.4	$0.48^{+0.12}_{-0.24}$	Kopparapu (2013)	M dwarfs[a]
0.5–2.0	0.34 ± 0.14	Traub (2012)	FGK dwarfs[o]
0.8–2.0	$0.028^{+0.019}_{-0.009}$	Catanzarite and Shao (2011)	FGK dwarfs[p]
0.5–3.0	2.75 ± 0.33	Youdin (2011)	G dwarfs[(q)]

Notes: [a]conservative Habitable Zone estimate (Kopparapu 2013); [b]optimistic Habitable Zone estimate (Kopparapu 2013); [c]corrected for reliability; [d]not corrected for reliability; [e]$237 \le P \le 500$ days; [f]model #4; [g]model #7; [h]$237 \le P \le 320$ days; [i]$0.28 \le S_{\rm inc} \le 1.0$; [j]$0.30 \le S_{\rm inc} \le 1.12$; [k]$237 \le P \le 500$ days; [l]$0.99 \le a_{\rm HZ} \le 1.7$ au; [m]$200 \le P \le 400$ days; [n]the author also required the Earth-sized planet to have a long-period giant-planet companion; [o]$228 \le P \le 1377$ days; [p]$0.75 \le a_{\rm HZ} \le 1.8$ au; [q]$P < 1$ year

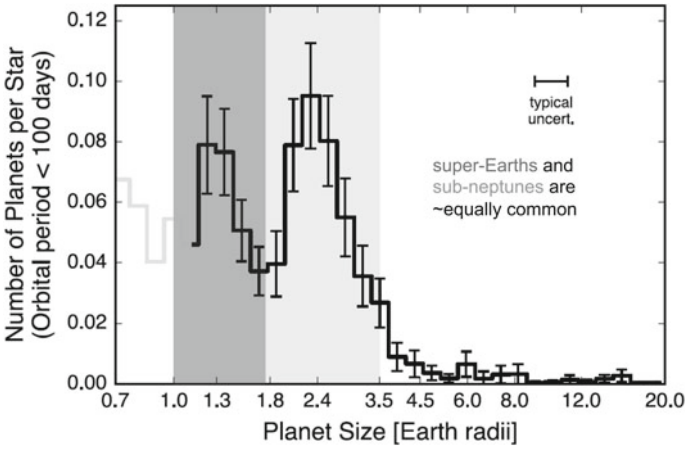

Fig. 3.18 The distribution of close-in planet sizes. The figure was showed by A. Howard in May 2019, during his lecture, and represents an update of the distribution reported by Fulton and Petigura (2018)

of extremely precise direct distance estimates provided by the second intermediate data release (DR2) of the Gaia mission (Gaia Collaboration 2016a, b, 2018) allowed to reduce typical uncertainties on the radius of stars in the *Kepler* field by close to a factor of 10. Using the improved knowledge of the stellar radii, Fulton et al. (2017) and Fulton and Petigura (2018) revisited the radius distribution of close-in ($P < 100$ days), small-size ($R_p < 4.0\ R_\oplus$) planets orbiting bright, unevolved solar-type stars, unveiling its clear bimodality (Fig. 3.18). In particular, the occurrence rate distribution at 1.5–2.0 $R_\oplus$ is suppressed by factor ~ 2. This 'gap' splits the population of close-in small planets into two size regimes of nearly identical intrinsic frequency: super Earths with $R_p < 1.5\ R_\oplus$ and sub-Neptunes with $R_p = 2.0$–$3.0\ R_\oplus$. The physical interpretation for the existence of the radius gap and in-depth studies of these two classes of small planets are the objective of much of recent research in the field, to which we now turn our attention.

3.4 Super-Earths and Sub-Neptunes

3.4.1 Key Questions

The bimodality of the small-radius planet distribution uncovered based on *Kepler* mission data suggests that super-Earths and sub-Neptunes are primarily rocky planets, which were born with primary atmospheres a few percent by mass accreted during the early stages of formation in the protoplanetary disk. Theoretical modeling suggests that terrestrial planet core sizes reach a maximum of ~ 1.6–$1.7\ R_\oplus$

(e.g., Fortney et al. 2007; Valencia et al. 2007; Rogers and Seager 2010; Mordasini et al. 2012b; Rogers 2015; Dorn et al. 2015). Planets with larger radii are mostly low-density and the inclusion of an extended atmosphere becomes a necessary ingredient. The radius gap is thus observed to occur precisely at the transition radius separating planets with and without gaseous envelopes.

Planets above the radius gap, the sub-Neptunes, were somehow able to retain their atmospheres, while planets below it, the super Earths, likely have lost their atmospheres and appear as naked cores. The mechanism that drives atmospheric loss for these planets remains an outstanding question. As with the mass-loss mechanism, the origin of the compositional properties of these two classes of planets is still a matter of debate. The two plausible formation pathways presently considered are[5]:

(a) the growth and migration of embryos from beyond the ice line (*the migration model*, e.g., Ida and Lin 2010; Morbidelli et al. 2015);
(b) inward-drifting of pebbles that coagulate to form planets close-in (*the drift model*, e.g., Ormel et al. 2017; Johansen and Lambrechts 2017).

In principle, density determination for transiting planets with measured radius and mass allows to directly infer their bulk composition, and one would therefore expect that the structural properties of exoplanets so determined would allow to distinguish between proposed scenarios for their formation and evolution. However, mass-radius relationships for small, low-mass planets from theoretical modeling (e.g., Bitsch et al. 2019; Turbet et al. 2020, and references therein) carry intrinsic degeneracies, with planets of vastly different composition (with different amounts of rock, ices, and/or gas) predicted to have observationally indistinguishable bulk densities (e.g., Adams et al. 2008; Miller-Ricci et al. 2009; Lozovsky et al. 2018), particularly for sub-Neptunes above the radius gap. Follow-up atmospheric characterization measurements are therefore necessary to help break any compositional degeneracies. However, density measurements are still of critical importance, as atmospheric analyses rely on the precise (typically, better than 20%) knowledge of mass and radius (e.g., Batalha et al. 2019).

The key questions on the true nature of close-in super Earths and sub-Neptunes can be summarized as follows: Did they form *in situ* or beyond the snowline? What causes the rock-gas transition and at what exact radius? What mechanism sculpted the radius gap? What is the diversity of planet core masses and compositions? Does it depend on stellar properties? There are the two observational channels routinely explored today to tackle these questions, as we discuss in the remainder of this Section: (1) in-depth statistical studies of the radius distribution of small *Kepler* planets, and (2) detailed investigations of the mass-radius relation for small planets.

[5] Excellent reviews of the subject can be found in Chap. 1 and, e.g., in Bean et al. (2021) and references therein.

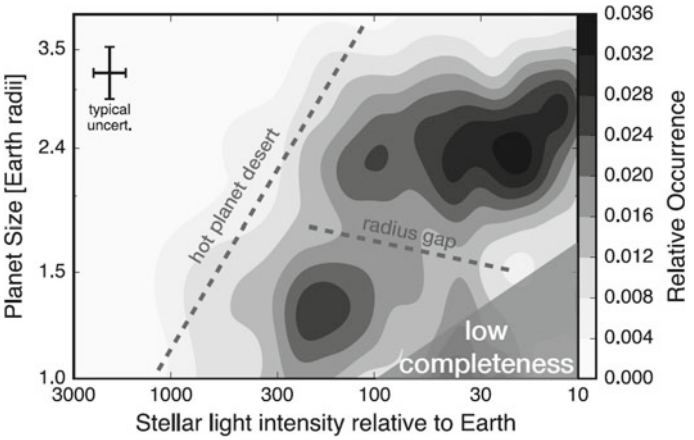

Fig. 3.19 Two-dimensional distribution of planet size and incident stellar flux. There are at least two peaks in the distribution. The figure was showed by A. Howard in May 2019, during his lecture, and represents an update of the distribution reported by Fulton et al. (2017) and Fulton and Petigura (2018)

3.4.2 Precise Radius Demographics

In the Fulton et al. (2017) and Fulton and Petigura (2018) studies, the nature of the two populations of super Earths and sub-Neptunes is best investigated when the planet radius distribution is plotted as a function of incident flux (Fig. 3.19). First of all, there is a clear dearth of $R_p > 2\,R_\oplus$ sub-Neptunes orbiting in high incident flux environments ($S_{inc} > 300\,S_\oplus$). These should be the easiest to detect, yet they do not appear in the Fulton et al. (2017) and Fulton and Petigura (2018) samples. The two studies reinforced the evidence for a scarcity of short-period Neptune-type (in size and mass) planets discussed in early analyses of exoplanet-population statistics from the *Kepler* mission, which had brought about the concept of 'Neptunian desert' (Szabó and Kiss 2011; Mazeh et al. 2016; Lundkvist et al. 2016). Second, most of the super-Earths with radii below the gap are orbiting in environments with $S_{inc} > 200\,S_\oplus$, while sub-Neptunes with radii above the gap typically receive $S_{inc} < 80\,S_\oplus$. Finally, from Fig. 3.19 it is also clear that the gap is present over a very wide range of $S_\oplus$, and there is hint of dependence of the central radius gap value on stellar insolation levels (or orbital period).

In the Fulton et al. (2017) and Fulton and Petigura (2018) studies the location of the peaks in occurrence for super Earths and sub-Neptunes is found at $R_p \sim 1.3\,R_\oplus$ and $R_p \sim 2.4\,R_\oplus$, respectively. More recent analyses with different sub-samples of *Kepler* planets all clearly resolved the radius valley, shifted the location of the peaks closer to $\sim 1.5\,R_\oplus$ and $\sim 2.7\,R_\oplus$, moved the center of the radius valley at ~ 1.9–$2.0\,R_\oplus$, and more robustly established that its position decreases with orbital period, characterizing the slope of the valley as a power law $R \propto P^\gamma$, with $\gamma \simeq -0.1$ (Van Eylen et al. 2018; Martinez et al. 2019; Petigura 2020) for the small-planet population

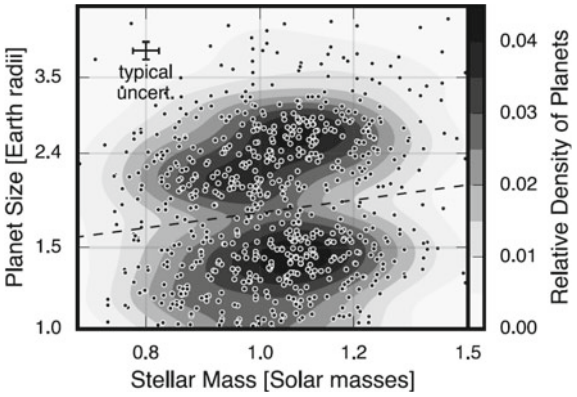

Fig. 3.20 Two-dimensional distribution of stellar mass and planet size. A dashed line is plotted at the location of the gap to guide the eye. Figure adapted from Fulton and Petigura (2018) and reproduced with permission from B. J. Fulton

around F-G-K dwarfs in the *Kepler* field. A slope with an opposite sign is instead recorded for the sample of close-in super Earths and sub-Neptunes found by *Kepler* around M dwarfs (Cloutier and Menou 2020). Fulton and Petigura (2018), Wu (2019) and Cloutier and Menou (2020) also showed that the feature locations (radius of both peaks and valley) move to smaller planet radii with decreasing mass of the F-G-K-M stellar primaries (see Fig. 3.20),

The radius gap (or valley), the 'desert' of hot sub-Neptunes, the location of the peaks in occurrence for super Earths and sub-Neptunes in different regimes of incident flux, and the trends of the feature locations with stellar mass provide some of the most formidable observational constraints for our understanding of the origin and composition of exoplanets with radii between those of Earth and Neptune. The gap has so far been explained primarily in terms of two atmospheric mass-loss mechanisms: core-powered mass-loss (e.g., Ginzburg et al. 2018; Gupta and Schlichting 2019 and photoevaporation (e.g., Owen and Wu 2016, 2017; Lopez & Fortney 2013; Jin and Mordasini 2018).

3.4.2.1 Radius Valley from Core-Powered Mass-Loss

In the core-powered mass-loss model (Ginzburg et al. 2016, 2018; Gupta and Schlichting 2019) the luminosity from a young, cooling rocky core heats a planet's envelope and drives its thermal evolution and mass loss. After a few Gyr of evolution the two end-member states are: (*i*) super-Earths, stripped rocky cores found below the radius valley, and (*ii*) sub-Neptunes, engulfed in H/He atmospheres and located above the valley (see Fig. 3.21). This mechanism is indeed capable to match the valley's location, shape and slope in planet radius–orbital period parameter space, and the relative magnitudes of the planet occurrence rate above and below the valley.

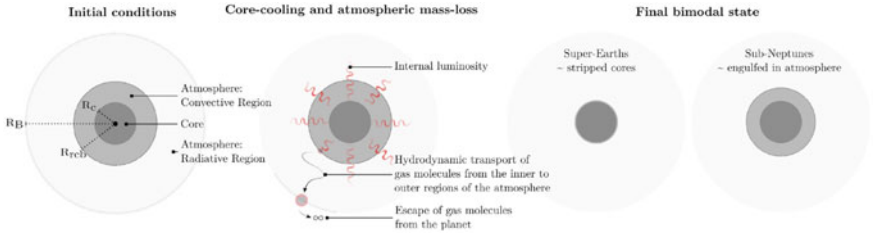

Fig. 3.21 Schematic drawing of planet evolution regulated by the core-powered mass-loss mechanism. The main components of the planet structure (left-hand panel) are the core (dark grey), the convective region (grey), and the radiative region (light grey). The thermal evolution and the atmospheric mass loss at the Bondi radius (middle panel) bring to two possible states at the end of evolution (right-hand panel). Figure taken from Gupta and Schlichting (2019) and reproduced with permission from Akash Gupta

In order to reproduce the correct position of the valley, the model requires that the observed planet population be predominantly composed of rocky cores with typical water–ice fractions of less than $\sim 20\%$.

A key element of the model is that the mass-loss mechanism is a by-product of planet formation processes, therefore it mostly depends on the properties of the planet. The studies carried out thus far have yet to show a dependence of the planet distribution parameters such as $S_{\rm inc}$ and $R_{\rm p}$ with stellar mass, which is instead clearly observed.

3.4.2.2 Radius Valley from Photoevaporation

The fact that small planets at short orbital periods are strongly influenced by the radiation of their host stars is generally expected within a broad range of theoretical frameworks (for a review of the subject see e.g., Owen 2019). At young ages, close-in planets, with extended atmospheres still in the cooling and contraction processes, absorb more efficiently a large fraction of the central stars' high-energy luminosity component L_{XUV}, which in turn emit the largest fraction of their total (bolometric) luminosity L_{Bol} in this channel precisely when they are young. The evolution of a star's high-energy flux is typically split into two different regimes (e.g., Jackson et al. 2012): a period lasting on the order of 100 Myr during which L_{XUV} is a constant fraction of L_{Bol} (the so-called saturated regime), followed by a clear decline in high-energy output that falls as $L_{XUV}/L_{Bol} \propto t^a$, with $a < -1.0$ (see Fig. 3.22). It is primarily in the saturated regime that the X-ray and UV radiation heats the outer layers of a close-in planet's envelope and drives mass loss, with the atmosphere undergoing severe photoevaporative effects (see cartoon of Fig. 3.23).

Theoretical models predicting that atmospheric erosion of short-period planets should result in the presence of a 'photoevaporation valley' in the radius distribution of planets around $1.7 - 2.0\,R_\oplus$ appeared in the literature before the radius gap was

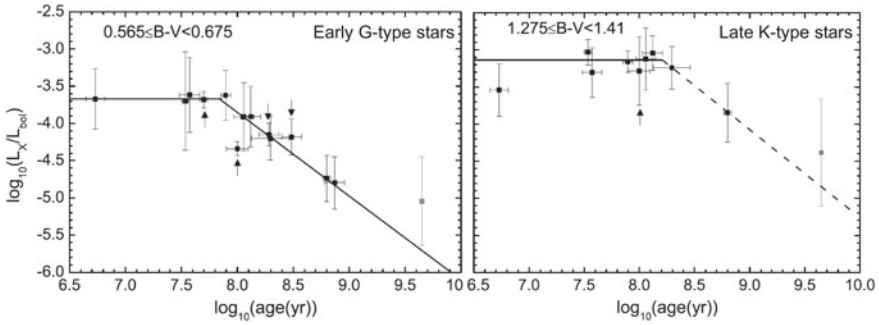

Fig. 3.22 X-ray-to-bolometric luminosity ratio versus age for earlier- (left panel) and later-type (right panel) stars in open clusters analyzed by Jackson et al. (2012). The solid lines indicate the fits to the data, while the dashed line indicates a less certain fit. Figure adapted from Jackson et al. (2012)

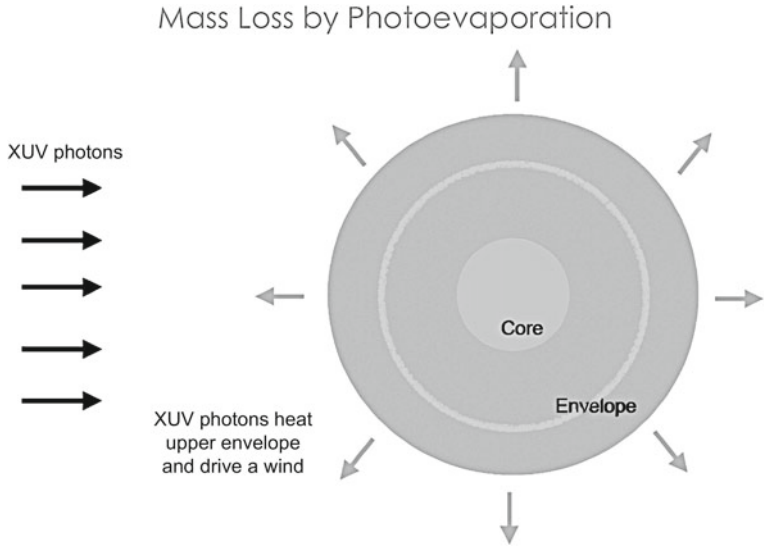

Fig. 3.23 Schematic drawing of mass loss by photoevaporation

actually observed (Owen and Wu 2013; Jin et al. 2014; Lopez and Fortney 2014; Chen and Rogers 2016). An example of the very good match between theoretical expectations and observational evidence is shown in the two panels of Fig. 3.24. Photoevaporation within ~ 100 Myr or so effectively 'herds' small planets into a population of closer-in super-Earths with $\sim 1.4\ R_\oplus$, which have been mostly stripped of their envelopes and one of sub-Neptunes further out that retained a significant fraction of their extended atmospheres and have approximately twice the core's radius ($\sim 2.6\ R_\oplus$).

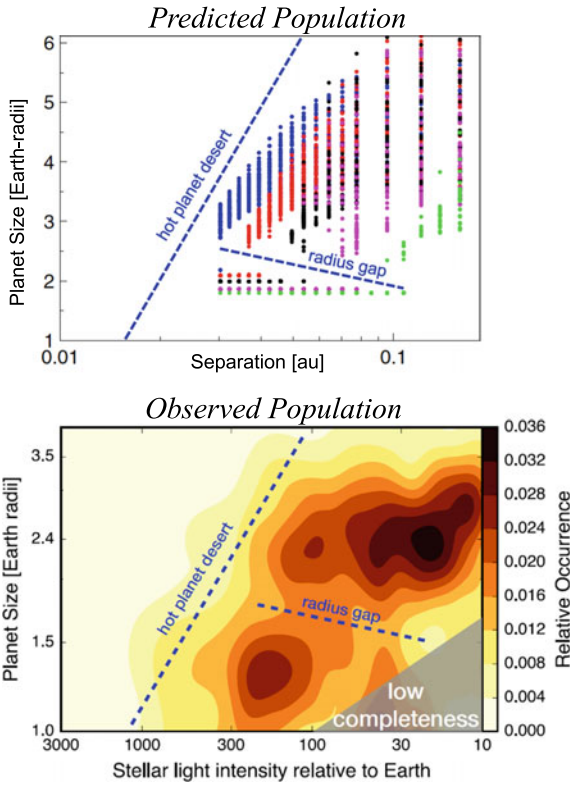

Fig. 3.24 Comparison between predicted and observed population. *Top*: Result of a planetary-evolution simulation; final radii of planets with an initial mass $M_{\rm p} < 20\,M_{\oplus}$, as a function of separation from a Sun-like star. Different colors represent different core masses. Figure adapted from Owen and Wu (2013) and reproduced with permission from James Owen. *Bottom*: same as Fig. 3.19

The exact details of the location, shape, and slope of the radius valley are a function of the adopted recipes in terms of planet formation processes, compositional properties of the formed planets, and the physics of evaporation (e.g., Owen and Wu 2017; Lopez & Rice 2018). In the most successful photoevaporation model to-date (Owen and Wu 2017), the valley location is found to be at:

$$R_{\rm valley} \sim 1.85\,R_{\oplus}\left(\frac{\rho_{M_{\oplus}}}{5.5\,{\rm g\,cm^{-3}}}\right)^{-1/3}\left(\frac{M_{\rm c}}{3\,M_{\oplus}}\right)^{1/4}, \tag{3.14}$$

where $M_{\rm c}$ is the core mass, and $\rho_{M_{\oplus}}$ is the density of a $1-M_{\oplus}$ core that depends only on the core composition. For terrestrial composition, $\rho_{M_{\oplus}} = 5.5\,{\rm g\,cm^{-3}}$, while it is 11.0, 4.0, and $1.4\,{\rm g\,cm^{-3}}$ for pure iron, silicate, and water/ice cores, respectively (Fortney et al. 2007). As shown in Fig. 3.25, the observed data exclude ice-rich cores and favor compositions that are roughly terrestrial, namely silicate–iron composites. In the Owen and Wu (2017) model, the observed features in the small-size planet radius distribution in the *Kepler* field can be explained in terms of a single population of planets initially formed with typical core masses around $3\,M_{\oplus}$ and terrestrial compositions, that were born with typical H/He envelopes of a few percent in mass.

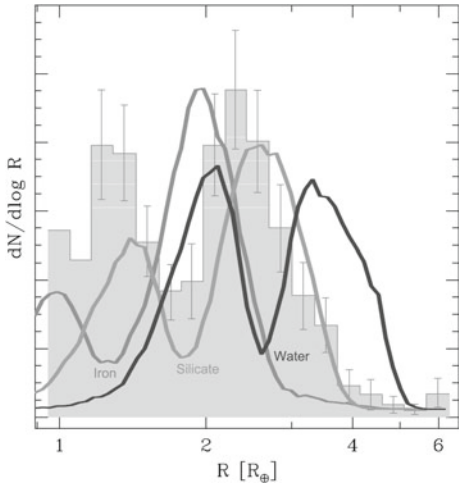

Fig. 3.25 Comparison between the observed radius distribution and models of evolving planets with cores made up of pure iron ($\rho_{\rm core} = 11\,{\rm g\,cm^{-3}}$), pure silicate ($\rho_{\rm core} = 41\,{\rm g\,cm^{-3}}$), and pure water ($\rho_{\rm core} = 1.3\,{\rm g\,cm^{-3}}$). Figure adapted from Owen and Wu (2017) and reproduced with permission from James E. Owen

Furthermore, as the time-integrated ratio L_{XUV}/L_{Bol} is a strong function of stellar mass ($\propto M_\star^{-3}$), the photoevaporation model also predicts shifts in the $S_{\rm inc}$ and $R_{\rm p}$ distribution with $M_\star$ that are also observed (Fig. 3.20, see also Fulton and Petigura 2018).

3.4.2.3 Other Ways of Creating the Radius Valley

Other small planet formation mechanisms have been proposed that could potentially produce a gap in the size distribution. These include: delayed formation in a gas-poor disk (e.g., Lee et al. 2014; Lee and Chiang 2016) and sculpting by giant impacts (e.g., Lee et al. 2015; Schlichting et al. 2015; Inamdar and Schlichting 2016). However, such models fail to reproduce some of the observed features of the radius distribution, such as the changing location of the gap radius as a function of orbital period or the correct gap radius location.

A key point to consider is that both the photoevaporation and core-powered mass-loss models are able to reproduce the correct position of the radius valley only under the assumption that the remnant cores populating the first peak of the radius distribution are mostly rocky in composition. This directly implies that such ice-poor planets must have formed within the water ice line (Owen and Wu 2017; Gupta and Schlichting 2019). However, a pure dry core composition for most short-period exoplanets is not really expected from formation models (Raymond et al. 2018; Bitsch et al. 2019; Brügger et al. 2020), as the combination of prominent accretion beyond the ice line and type I migration tends to move small-mass planets with $M_{\rm p} \lesssim 20\,M_\oplus$ inwards quite effectively (e.g., Tanaka et al. 2002). Recent work coupling planet formation and evolution modeling (Venturini et al. 2020) has shown that a bimodality

in core mass and composition from birth naturally renders a radius valley at 1.5–2.0 $R_\oplus$. In this framework, the first peak of the *Kepler* size distribution is confirmed to be populated by bare rocky cores, as shown extensively by others (Owen and Wu 2017; Jin and Mordasini 2018; Gupta and Schlichting 2019), while the second peak can host half-rock–half-water planets with thin or non-existent H-He atmospheres, as suggested by a few previous studies (Dorn et al. 2017; Zeng et al. 2019).

3.4.3 Structural Properties of Small Planets

The mass-radius diagram for transiting exoplanets is the fundamental tool that allows to directly compare the observational data with structural models, expressed in terms of iso-density curves that describe the mass-radius relation for a fixed composition, For almost a decade since the discovery of the first transiting planet (Charbonneau et al. 2000), inferences on the structure of exoplanets were confined to the realm of hot Jupiters, to which wide-field ground-based transit surveys (e.g., TrES, XO, HAT-Net, HATSouth, Super-WASP) are mostly sensitive. Nevertheless, the growing numbers of Doppler-detected low-mass ($m_\mathrm{p} \sin i < 30\ M_\oplus$) companions and the expectations from very high-precision space-based transit photometry missions (CoRoT and *Kepler*) motivated the development of early structural models and theoretical mass-radius relations for super Earths and sub-Neptunes (e.g., Valencia et al. 2007; Seager et al. 2007; Fortney et al. 2007).

3.4.3.1 The Dawn of Density Measurements of Small Planets

From a historical perspective, the two highly successful space-borne transit surveys, CoRoT and *Kepler*, were not the first to provide initial insights on the structural properties of small planets with $R_\mathrm{p} \sim 1 - 4\ R_\oplus$. Indeed, the first planet with a Neptune-like radius was discovered by Gillon et al. (2007) transiting the nearby M-dwarf GJ 436, as part of a follow-up project to search for transits of known Doppler-detected planets. Soon thereafter, the first ground-based transit survey aimed specifically at finding small-size planets around mid- to late-M stars, the MEarth project, identified a transiting sub-Neptune with $R_\mathrm{p} = 2.79 \pm 0.2\ R_\oplus$ around the M4.5 V dwarf GJ 1214 (Charbonneau et al. 2009).

Eventually, the era of space-based transit photometry unfolded. Figure 3.26 shows the mass-radius diagram for small planets as of summer 2011. The three notable additions belong to the class of ultra-short-period ($P_\mathrm{orb} < 1$ day) planets (see Sect. 3.7): a) CoRoT-7 b, the first rocky super-Earth with measured radius (Léger et al. 2009; Hatzes et al. 2010), Kepler-10 b, the first rocky planet delivered by *Kepler* (Batalha et al. 2011), and 55 Cnc e, a hot super Earth that constitutes one of the two most important results from the MOST satellite (Winn et al. 2011). This handful of keystone planets is representative of the diversity of compositional properties of small planets. By comparison with more recent structural and evolutionary models (Zeng

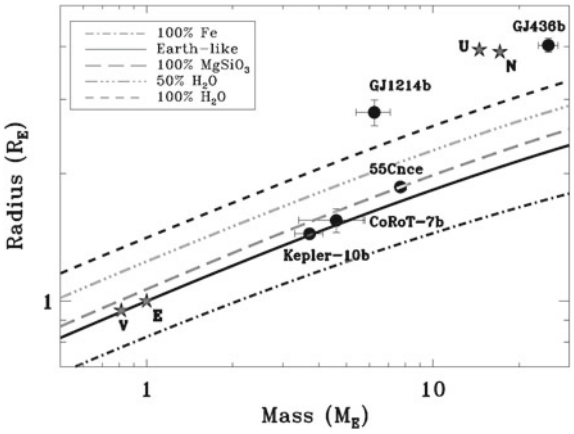

Fig. 3.26 The mass-radius diagram for small transiting exoplanets in mid-2011. The positions of the rocky and ice-giant planets of the Solar System are also shown. The different curves depict internal structure models of a variable composition from Zeng et al. ((Zeng et al. 2019)) (as reported in the legend): 100% iron, Earth-like (32.5% Fe + 67.5% MgSiO3), pure rock (100% MgSiO3), 50% Earth-like rocky core + 50% H_2O layer by mass, and 100% H_2O mass

and Sasselov 2013; Howe et al. 2014; Zeng et al. 2019) one infers that GJ 1214 b and GJ 436 b could be described as rocky worlds with a variable degree of volatiles in their interiors and substantial (2%–10% in mass), thick H_2/He gaseous envelopes of primordial origin (e.g., Lozovsky et al. 2018; Zeng et al. 2019). For Kepler-10 b and CoRoT-7 b, a truly Earth-like composition fits very well the observed mass and radius (e.g., Zeng et al. 2019), while 55 Cnc e has either a very low iron fraction or an envelope of low-density volatiles (e.g., Dai et al. 2019).

3.4.3.2 An Instructive Example

One of the relevant results of the Eta-Earth Keck survey was the discovery announced by Howard et al. (2011) of a warm ($P = 9.5$ days) low-mass planet around the bright K1 dwarf HD 97658. The planet was successively found transiting based on observations with the MOST and Spitzer satellites (Dragomir et al. 2013; Van Grootel et al. 2014). Its measured mass and radius are 7.8 $M_\oplus$ and 2.2 $R_\oplus$, respectively, making it a typical resident of the second peak in the radius distribution of small planets.

The physical properties of HD 97658 b imply a bulk composition that cannot be uniquely determined. Its mass and radius are compatible with those of a planet with a rocky core, a large silicate mantle, and a thin H_2/He envelope. However, the same mass and radius equivalently match those of a water-rich sub-Neptune, with no gaseous envelope (Fig. 3.27). Alternatively, the similar mass and radius can also be reproduced by structural models encompassing a 10%–20% super-critical water hydrosphere topping a 80%–90% mantle-like composition interior (e.g., Mousis et al.

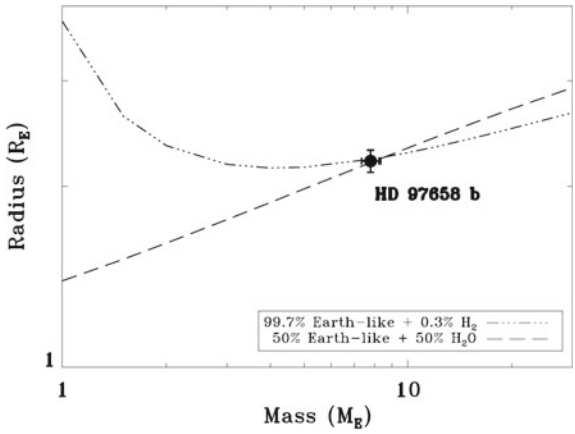

Fig. 3.27 The mass and radius of HD 97658 b highlight the problem of compositional degeneracies for sub-Neptunes, that cannot be resolved solely based on their physical properties (see text)

2020). As a consequence, HD 97658 b's formation history is also unclear, as a rocky super Earth with a small H_2/He envelope mass fraction could have formed *in situ*, while a water-rich sub-Neptune is expected to have formed beyond the snowline ($\gtrsim 2$ au) and then migrated inward to its present location at ~ 0.1 au.

To break compositional degeneracies for sub-Neptunes, atmospheric characterization measurements should play a decisive role. In particular, measurements of the transmission spectra allow to directly estimate the mean molecular weight of the planet's atmosphere (e.g., Miller-Ricci et al. 2008a, b; Fortney et al. 2013), which in turn provides improved constraints on its interior composition. Knutson et al. (2014a) utilized HST/WFC3 to perform near-infrared transmission spectroscopy of HD 97658 b's atmosphere, retrieving a featureless transmission spectrum. The most likely explanation is that the planet's atmosphere is dominated by clouds or hydrocarbon hazes that prevent one from detecting molecular absorption features. Similar results have been derived with HST/WFC3 transmission spectroscopy of GJ 1214 b (Kreidberg et al. 2014) and GJ 436 b (Knutson et al. 2014b). This is a potentially strong limitation towards gaining further insights on the overall structural properties of sub-Neptunes such as HD 97568 b. Fortunately, successful detections of molecular absorption have also been reported in the most recent literature for such objects (e.g., Tsiaras et al. 2019; Benneke et al. 2019; Kreidberg et al. 2020; Guilluy et al. 2021; Mikal-Evans et al. 2021). Even in the case of flat transmission spectra measured with HST, there are encouraging prospects for accessing strong molecular features in the atmospheres of sub-Neptunes at longer wavelengths with JWST (Crossfield and Kreidberg 2017; Kawashima et al. 2019).

3.4.3.3 Modern-Day Mass-Radius Relationships

The wealth of $R_p < 4\,R_\oplus$ transiting planet candidates uncovered by the *Kepler* mission refocused the investment of observing time with high-resolution spectro-

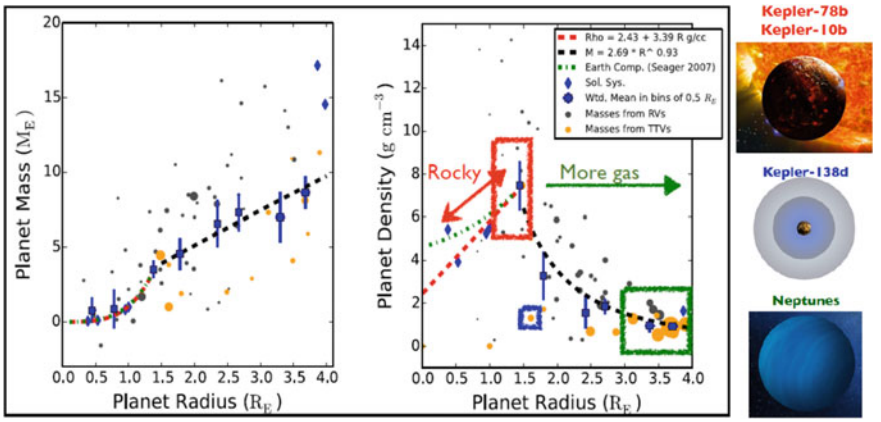

Fig. 3.28 The mass-radius diagram as of 2014. The colored boxes refer to the position of Earth, Super-Earth and Neptunes planets (see the legend on the top of the right-hand panel). Prototypes of these types of planets are shown to the right of the plots. Figure adapted from Weiss and Marcy (2014) and reproduced with permission from Lauren M. Weiss

graphs with high-precision RV measurement capabilities in follow-up programs for mass determination. Marcy et al. (2014) presented a first significant sample of mass measurements (or meaningful upper limits) for small *Kepler* candidates based on Keck/HIRES RVs. This study enabled the first empirical determination of the mass-radius relation for super Earths and sub-Neptunes. Weiss and Marcy (2014) used a sample of 65 planets with $P < 100$ days and with either measured masses or upper limits (including $\sim 10\%$ of objects with negative masses!). They fit a simple parametric model, a power-law, to the observed mass-radius distribution, obtaining $R_p \propto M_p^{0.27}$ for $R_p < 1.5\,R_\oplus$ and $R_p \propto M_p^{1.07}$ for $1.5\,R_\oplus \leq R_p \leq 4\,R_\oplus$. They showed an increase in density with R_p, with a clear peak at $\rho_p \sim 7.6\,\mathrm{g\,cm^{-3}}$ for $R_p \sim (1.4\text{–}1.5)\,R_\oplus$, followed by a sharp decline at larger radii (see Fig. 3.28).

The Weiss and Marcy (2014) analysis constituted the first comparative study of the observed mass-radius relation for close-in super Earths and sub-Neptunes with theoretical expectations. It broadly confirmed the notion that objects with $R_p \lesssim 1.5\,R_\oplus$ are mostly rocky in composition, while planets with larger radii must be composed of increasingly larger amounts of volatiles and/or H_2/He gaseous envelopes. Weiss and Marcy (2014) also found a large scatter around the empirical $M_p - R_p$ relation, indicating a significant diversity in planet composition at a given radius.

After the end of the original *Kepler* mission in 2013, its continuation, the K2 mission, and more recently (since 2018) the TESS mission have produced > 1000 new transiting planet candidates in the super-Earth and sub-Neptune radius regime. Most importantly, a large fraction of the candidates orbits around much brighter stars than the original *Kepler* sample. This has enabled more successful, systematic follow-up programs for mass determination with the Doppler method. As of March 2021, there are 192 planets with $R_p < 4\,R_\oplus$ and a non-zero mass measurement reported

with any precision. This number becomes 146, 102, and 34 with the request of mass measurements good to better than 30%, 20%, and 10% precision, respectively.[6]

With growing numbers of better characterized small-size, low-mass planets, modeling efforts have revisited the initial studies on theoretical mass-radius relations (e.g., Seager et al. 2007; Fortney et al. 2007; Rogers and Seager 2010; Valencia et al. 2010; Lopez et al. 2012). On the one hand, consensus appears to have been reached on threshold radii for a given composition, representing the radius above which a planet has a very low probability of being of that specific composition. Rogers (2015) and Lozovsky et al. (2018) converged on a threshold value of $\sim 1.6\ R_{\oplus}$ for purely rocky planets, and Lozovsky et al. (2018) determined that planets with radii above $\sim 2.6\ R_{\oplus}$ (and up to the radius of Neptune) must have retained envelopes of hydrogen and helium typically amounting to 1%–10% in terms of mass fraction. On the other hand, the details of the compositional properties of super Earths and sub-Neptunes have been fine-tuned, particularly in the latter case. Recent work has not only revisited the notion that they could be rocky worlds with small amounts of volatiles in their interiors and substantial, thick H_2/He gaseous envelopes of primordial origin (e.g., Owen and Wu 2017; Van Eylen et al. 2018; Gupta and Schlichting 2019), but it has also re-assessed the likelihood that sub-Neptunes might be 'water worlds' or 'ocean planets', containing significant amounts of water in primarily solid (ices) form, with thin or non-existent H_2/He-dominated atmospheres (e.g., Léger et al. 2004; Zeng et al. 2019; Madhusudhan et al. 2020; Venturini et al. 2020). Finally, recent investigations have also produced predictions on the mass-radius relation for strongly irradiated water-rich rocky planets that might also possess endogenic thick H_2O-dominated, steam atmospheres, in which up to 100% of the planetary water content appears in vaporized form (Dorn et al. 2018; Turbet et al. 2019; Zeng et al. 2019; Mousis et al. 2020).

From an (semi-)empirical point of view, updates to the Weiss and Marcy (2014) power-law fits have been published in the recent past by Wolfgang et al. (2016), Zeng et al. (2016), Bashi et al. (2017), Chen and Kipping (2017), and most recently by Otegi et al. (2020). These works used different cuts in the properties of the small planet population, different prescriptions on the statistical confidence with which planet radii and particularly masses are determined, and differ also in aspects of the methodological approach. Despite some degree of heterogeneity in the planet samples investigated, the above analyses provide broadly consistent results, as summarized in Table 3.2. Other determinations of the mass-radius relationship based on slightly more flexible Bayesian or non-parametric approaches (Ning et al. 2018; Ma & Ghosh 2019; Kanodia et al. 2019; Ulmer-Moll et al. 2019) capture its main features similarly well, reducing in part the spread around the relation.

The two panels of Fig. 3.29 show the state-of-the-art of the mass, radius, and density measurements of super Earths and sub-Neptunes, restricted to mass determinations to better than 20% precision. In the left panel, the power-law fits from Otegi et al. (2020) in the rocky and volatile-rich regime are overplotted. The two populations are rather clearly identified, The dispersion in the relation for rocky planets

[6] Data from the transiting exoplanet catalogue TEPCat: https://www.astro.keele.ac.uk/jkt/tepcat/ .

Table 3.2 Parametric mass-radius relations derived for small planets by past studies

Authors	Power-law Fit	Regime of validity
Weiss and Marcy (2014)	$R_\mathrm{p} \propto M_\mathrm{p}^{0.27}$	$R_\mathrm{p} < 1.5\ \mathrm{R}_\oplus$ (rocky)
Weiss and Marcy (2014)	$R_\mathrm{p} \propto M_\mathrm{p}^{1.07}$	$1.5\ \mathrm{R}_\oplus \leq R_\mathrm{p} \leq 4.0\ \mathrm{R}_\oplus$ (non-rocky)
Wolfgang et al. (2016)	$R_\mathrm{p} \propto M_\mathrm{p}^{0.66}$	$R_\mathrm{p} < 4\ \mathrm{R}_\oplus$ (small planets)
Zeng et al. ((Zeng et al. 2016))	$R_\mathrm{p} \propto M_\mathrm{p}^{0.27}$	$1\ \mathrm{M}_\oplus < M_\mathrm{p} < 8\ \mathrm{M}_\oplus$ (small planets)
Bashi et al. ((Bashi et al. 2017))	$R_\mathrm{p} \propto M_\mathrm{p}^{0.55}$	$R_\mathrm{p} < 12.1\ \mathrm{R}_\oplus$, or $M_\mathrm{p} < 124\ \mathrm{M}_\oplus$ (small planets)
Chen and Kipping ((Chen and Kipping 2017))	$R_\mathrm{p} \propto M_\mathrm{p}^{0.28}$	$M_\mathrm{p} < 2\ \mathrm{M}_\oplus$ (Earth-like)
Chen and Kipping ((Chen and Kipping 2017))	$R_\mathrm{p} \propto M_\mathrm{p}^{0.59}$	$2\ \mathrm{M}_\oplus < M_\mathrm{p} < 120\ \mathrm{M}_\oplus$ (Neptune-type)
Otegi et al. ((Otegi et al. 2020))	$R_\mathrm{p} \propto M_\mathrm{p}^{0.29}$	$\rho_\mathrm{p} > 3.3\ \mathrm{g\ cm^{-3}}$ (rocky)
Otegi et al. ((Otegi et al. 2020))	$R_\mathrm{p} \propto M_\mathrm{p}^{0.63}$	$\rho_\mathrm{p} < 3.3\ \mathrm{g\ cm^{-3}}$ (volatile-rich, up to $M_\mathrm{p} \sim 120\ \mathrm{M}_\oplus$)

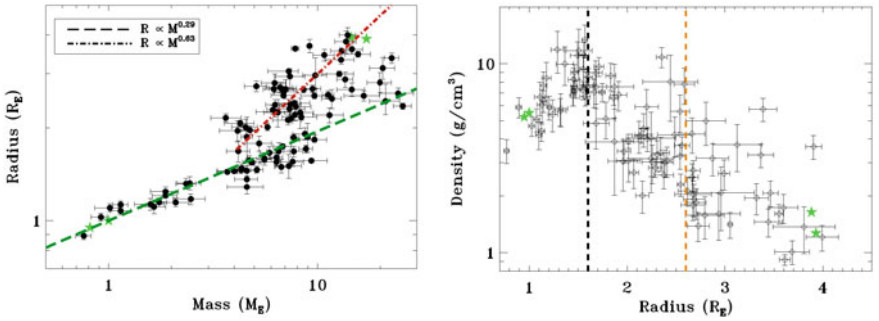

Fig. 3.29 *Left*: the state-of-the-art mass-radius diagram for super-Earth and sub-Neptune exoplanets having a mass that was determined with a precision better than 20%. Dashed and dot-dashed lines are the best-fitting lines for the rocky and volatile-rich populations from Otegi et al. (2020). The green stars denote the Solar System planets as in Fig. 3.26. *Right*: the radius-density diagram for the same population. The two vertical dashed lines at 1.6 $R_\oplus$ and 2.6 $R_\oplus$ indicate the threshold radii for the rocky to volatile-rich transition and for the transition between water worlds and planets with gaseous envelopes, respectively

is rather small, with indications of a population of planet with very large iron cores with masses in the approximate range $4 - 10\ M_\oplus$. The most massive rocky planet has $M_\mathrm{p} \sim 25\ M_\oplus$. The dispersion around the relation for volatile-rich planets is much larger. In the right panel, the threshold radius of 1.6 $R_\oplus$ for the rocky to volatile-rich transition rather clearly matches the point in which ρ_p changes its dependence with R_p (from direct to inverse). At the transition radius of 2.6 $R_\oplus$ between water worlds and planets with gaseous envelopes proposed by Lozovsky et al. (2018) nothing special seems to happen.

It is finally worth mentioning how the growing sample of super Earths and sub-Neptunes with well-determined properties can be investigated in a statistical sense in order to uncover patterns (e.g., overdensities) in parameter space that might represent

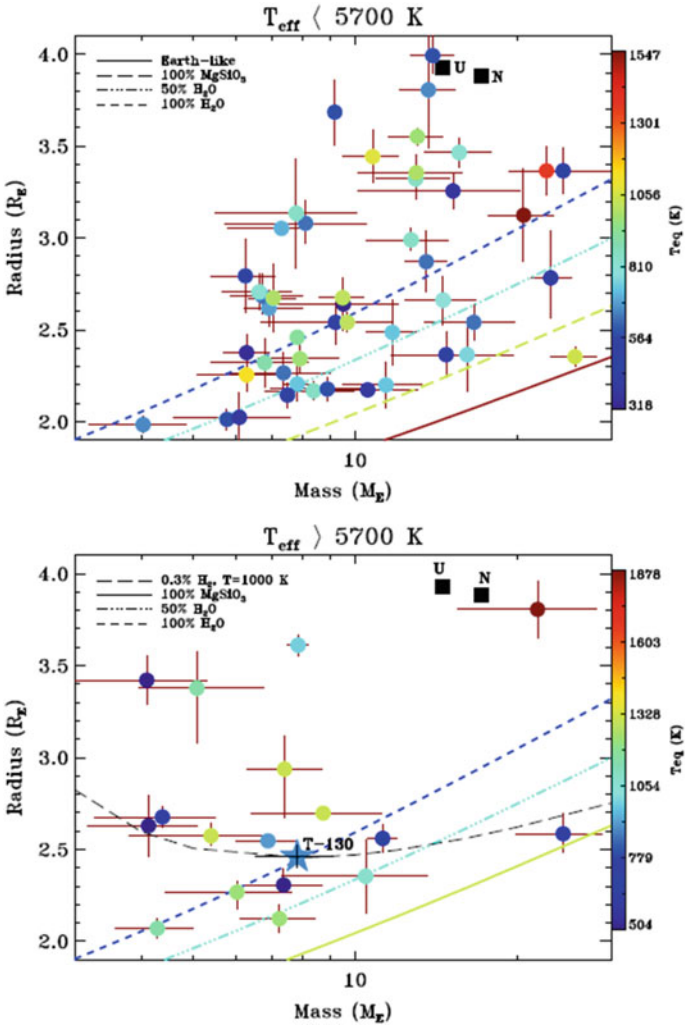

Fig. 3.30 *Top*: mass-radius diagram of sub-Neptunes with masses determined at the $3\,\sigma$ level (or better), orbiting primaries with $T_{\rm eff} < 5700$ K. The objects are color-coded by their equilibrium temperature. The different curves depict internal structure models of variable composition from Zeng et al. 2019, as reported in the legend. *Bottom*: same plot, but for sub-Neptunes around primaries with $T_{\rm eff} < 5700$ K

fossil evidence of the planets' formation and evolution history, as it has been done using radius alone (Fulton et al. 2017; Fulton and Petigura 2018). Considering all sub-Neptunes with masses detected to better than 30% precision, Sozzetti et al. (2021) showed a possible lack of $M_{\rm p} > 10\,M_{\oplus}$ companions around G- and F-type stars with $T_{\rm eff} > 5700$ K, particularly for objects with $R_{\rm p} \gtrsim 2.5\,R_{\oplus}$ (see Fig. 3.30). This can be

interpreted as fossil evidence of planet formation around stars of varied mass. More massive primaries typically have higher-mass disks. Upon reaching the critical mass ($10\,M_\oplus$ or so), newly formed cores have a higher chance of quickly accreting large amount of gas, ending up their formation process as giant planets.

3.5 Planet Multiplicity

The average number of planets per star is a very difficult parameter to constrain precisely, because of the variety of selection effects and variable sensitivity to areas of the parameter space inherent to different detection techniques. Our Solar System has 8 planets, which sounds like a high degree of multiplicity, and a very interesting architecture with the following relevant features: (*a*) quasi-geometric progression in orbital spacings; (*b*) clear hierarchy in mass, with inner terrestrial planets 10–100 s of times lower in mass than the outer gas giants; (*c*) almost circular orbits; (*d*) mostly prograde orbits; (*e*) almost coplanar orbits, with low mutual inclinations (Fig. 3.31).

Are we typical? This is one key question in the field of exoplanet demographics, for which we have yet to find the answer. On the one hand, by comparison with the astonishing diversity of the orbital and physical properties of known planetary systems to-date (see Fig. 3 in Chap. 1 for examples from RV and transit surveys), one would be inclined to draw the conclusion that the one we live in is *unlike* any

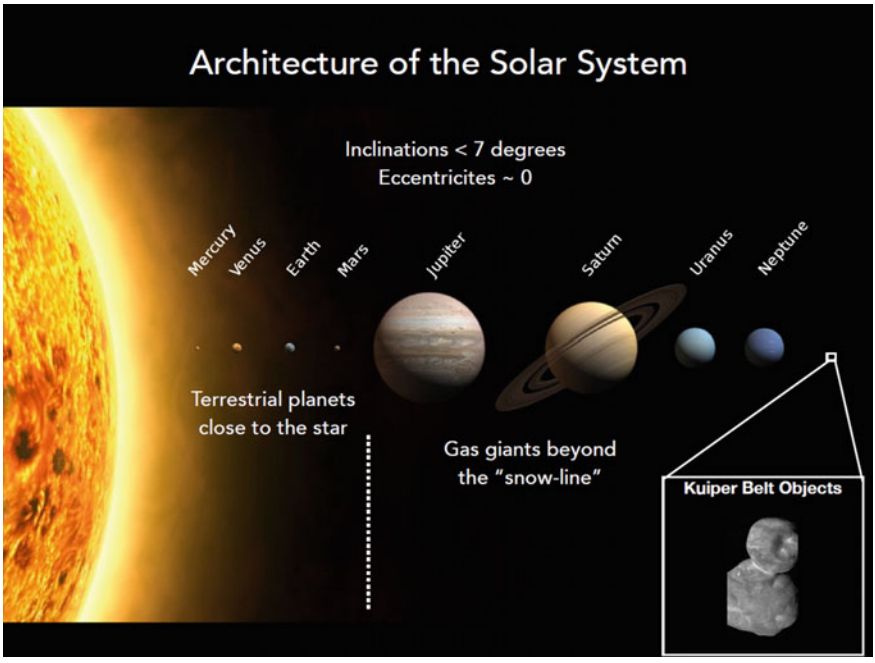

Fig. 3.31 Solar-system architecture. Figure showed by A. Howard in May 2019 during his lectures

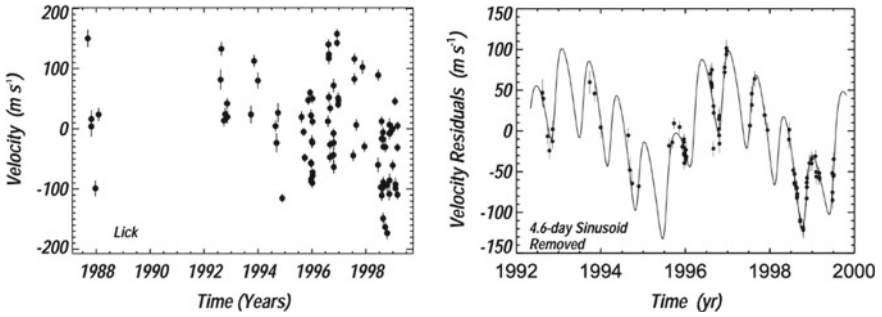

Fig. 3.32 *Left*: RV measurements for υ And from the Lick Observatory. *Right*: residual velocities for υ And after removal of the 4.6-day Keplerian signal from the data. The line shows the best-fit model describing the RV variations due to the outer two companions. Figures taken from Butler et al. (1999) and reproduced with permission from R. P. Butler

other planetary systems, and the rate of occurrence of Solar-System analogs might be (much) below 1% (e.g., Schlaufman 2014. See also Chap. 1). On the other hand, the limited sensitivity of detection techniques to Solar-System-like architectures suggests that the result is still due, at least in part, to observational biases rather than an intrinsically low frequency of true analogs of the Solar System.

The study of the global architecture of planetary systems and the identification of trends and patterns in their properties constitute some of the most formidable observational constraints for planet formation, orbital migration, and dynamical evolution models. As far as multiple-planet systems at short and intermediate separation are concerned, the Doppler and transit techniques have allowed us to make large strides toward the understanding of how different other systems can be from our own.

3.5.1 Multi-planet Systems from Doppler Surveys

3.5.1.1 Early Investigations

The detection of the first multi-planet system around a solar-type star[7] was announced four years after the discovery of 51 Peg b by Butler et al. (1999). Three giant planetary companions were found orbiting the solar-type star υ Andromedae: a hot Jupiter ($M_\mathrm{p} \sin i = 0.7\, M_\mathrm{Jup}$) with $P = 4.6$ d, and two super-Jupiters ($M_\mathrm{p} \sin i \sim 2.0 M_\mathrm{Jup}$ and $M_\mathrm{p} \sin i \sim 4.0 M_\mathrm{Jup}$) on longer periods (241 d and 1278 d, respectively).

Figure 3.32 shows the original RV time-series and the multi-Keplerian orbit fit to the RV signals induced by the two outer gas giants. The amplitudes and periods of

[7] Prior to this announcement, Wolszczan and Frail (1992) had published the detection, based on the pulsar timing technique, of two terrestrial-mass companions orbiting at 0.36 au and 0.47 au from the neutron star PSR 1257 + 12.

the RV modulations could not be explained in terms of any known star-related effects (rotation, pulsations, magnetic cycles) that could mimic a truly Keplerian signal, and their planetary nature therefore safely established. A decade later, Wright et al. (2009) presented a detailed analysis of 67 exoplanets in 28 multiple systems, at the time comprising 14% of known host stars of extrasolar planets within 200 pc. Figure 3.33 presents the chart of semi-major axes and minimum masses for the Wright et al. (2009) sample.

This remarkably diverse sample enabled the first systematic investigation of the statistical properties of multi-planet systems. In particular, Wright et al. (2009) uncovered difference in the population compared to that of systems with only one detected planet: *a*) multiple systems appear to have typically lower eccentricities, *b*) planets in multiple systems are somewhat lower in mass, and *c*) the distribution of orbital distances for multi-planet systems differs from that of single planets. Wright et al. (2009) also found marginal evidence for multi-planet hosts to be slightly more metal-rich that host stars of single planets, while no differences with stellar mass between the two populations arose.

The Wright et al. (2009) sample contained important information on orbital spacing of exoplanet systems. In particular, $\sim 20\%$ of the sample was known at the time to be in or near mean-motion resonances, characterized by period ratios that are nearly equal to ratios of small integers. At least one system (GJ 876) had been shown to undergo strong dynamical interactions, with changes in orbital elements on timescales comparable to those of the RV observations. The spacings of the other systems indicated instead the presence of secular interactions, primarily dictated by different types of apsidal motion (libration, circulation, or at the boundary between the two states), and affecting particularly the values of eccentricity and mutual inclinations on very long timescales.

Broadly speaking, the observed orbital properties (in particular the eccentricity) of the multiple-planet systems in the Wright et al. (2009) sample, as well as their dynamical features in terms of resonant and secular behavior are consistent with planet formation by core/pebble accretion followed by two possible pathways of orbital evolution: (1) smooth gas-driven migration in the protoplanetary disk and (2) a more violent history of early dynamical interactions involving planet-planet scattering and subsequent high-eccentricity migration and tidal circularization. The latter evolutionary channel appears to explain more effectively the properties of both close-in single hot-Jupiter systems and multiple systems with $a < 5$ au (more on this in Sect. 3.6.1. See also Chap. 1).

3.5.1.2 Further Characterization of the Population

As of April 2021, there are ~ 400 Doppler-detected exoplanets in ~ 160 multiple systems, including over 30 systems with at least one transiting planet.[8] The left-hand panel of Fig. 3.34 shows the distribution of period ratios for planet pairs with

[8] Source: exoplanet.eu and https://exoplanetarchive.ipac.caltech.edu/ .

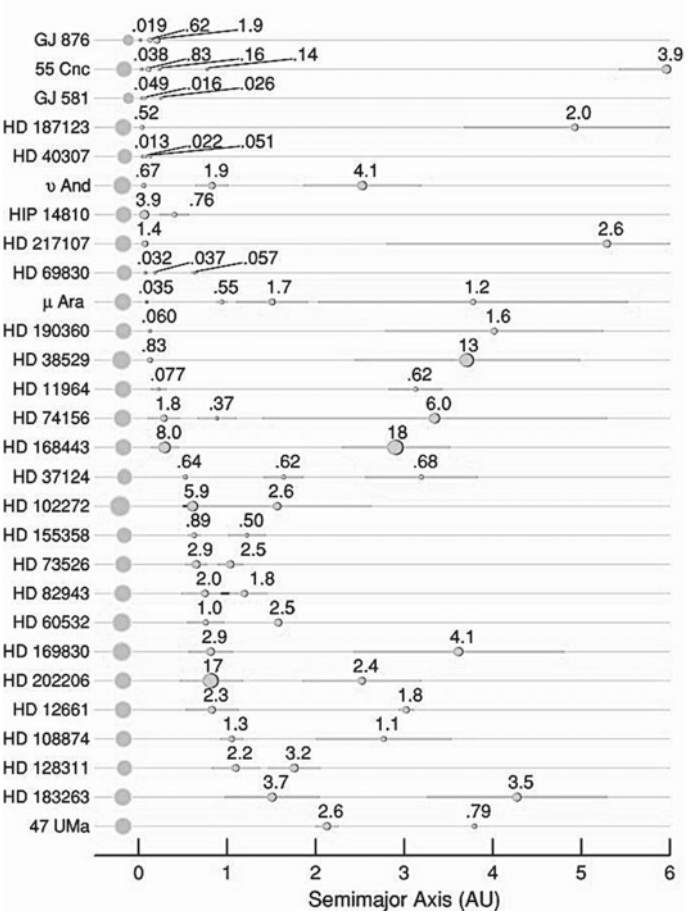

Fig. 3.33 Chart of semi-major axes and minimum masses for the 28 known multiplanet systems as of 2009. The first circle in each row represent the star, while the others represent the hosted planets. The sizes of the circles are proportional to the cube root of the stellar mass and the planetary $M_p \sin i$, respectively. The horizontal line intersecting the planet represents the periapse to apoapse excursion. Figure adapted from Wright et al. (2009) and reproduced with permission from Jason T. Wright

$P_{out}/P_{in} < 4$. There are clear peaks just wide of the 3:2 and 2:1 resonances, and another peak just interior to the 4:1 resonance. The smallest period ratio is recorded for the pair of super Earths HD 215152 b,c (Delisle et al. 2018), $\sim 1\%$ wide of the 5:4 resonance. From the right-hand panel of Fig. 3.34 we learn that the peak near the 2:1 resonance is populated by pairs of giant planets with total mass $\gtrsim 1\ M_{Jup}$, as it had already been noted by (Winn and Fabrycky 2015). The pairs in the peaks next to the 3:2 and 4:1 resonances are instead primarily composed of low-mass planets with masses $\lesssim 0.1\ M_{Jup}$. In general, most pairs in multi-planet systems detected in RV surveys do not lie near a period commensurability, however their mass correlates rather clearly with period ratio (Fig. 3.35).

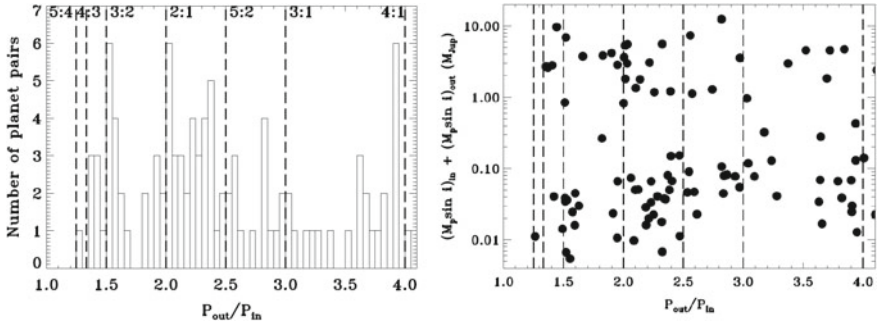

Fig. 3.34 *Left*: the distribution of period ratios for Doppler-detected planet pairs with $P_{\rm out}/P_{\rm in} < 4$. Vertical lines indicate first- and higher-order resonances. *Right*: total mass in a pair versus period ratio. The vertical lines are the same as in the left panel

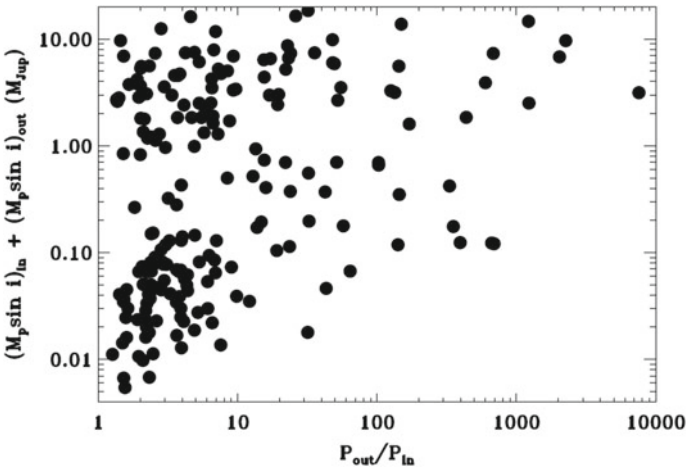

Fig. 3.35 Same as Fig. 3.34, but for all values of period ratio

The four panels of Fig. 3.36 show other interesting features of the population of multi-planet systems from RV surveys. First, the mass ratio clearly correlates with period ratio (top left panel), with only 28% of pairs in which the outer companion is the less massive one. Second, pairs with relatively low mass ratios ($\lesssim 4$) are more often composed of low-mass planets (top right panel), with a sparse population ($\sim 10\%$) of systems with high mass ratios (> 10) composed of an inner low-mass planet and an outer massive companion with a large period ratio. The masses of planet pairs are strongly correlated across all mass regimes (bottom left panel), but particularly so for companions with minimum masses below $10\,M_\oplus$. The sample of inner planets with $10\,M_\oplus \lesssim M_{\rm p} \sin i \lesssim 30\,M_\oplus$ is instead often accompanied by an outer, significantly more massive companion. Finally, low-mass pairs are almost exclusively found around K- and M-dwarf primaries ($M_\star \lesssim 0.8\,M_\odot$), while the sam-

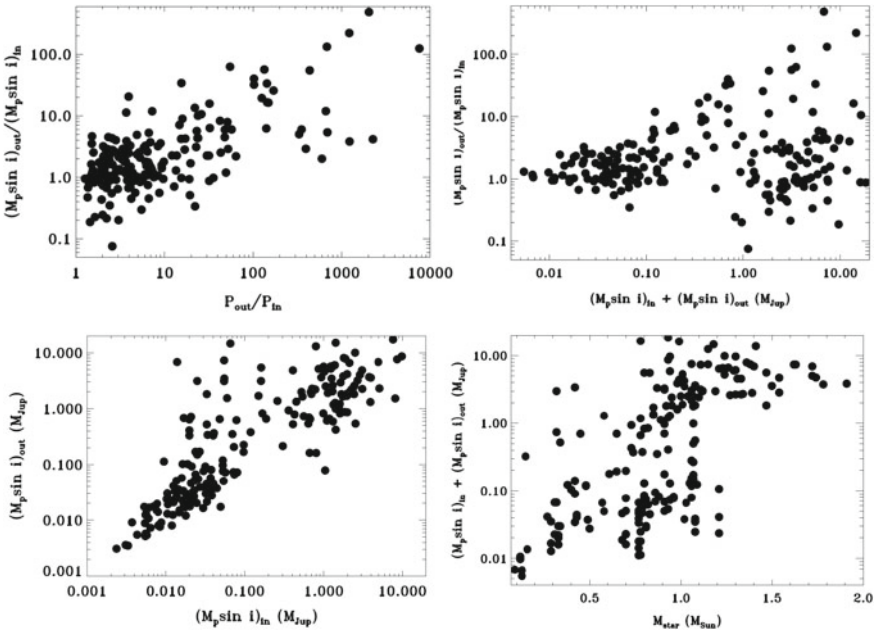

Fig. 3.36 *Top left*: mass ratio versus period ratio for planet pairs in Doppler-detected multiple systems. *Top right*: mass ratio versus total mass in pair. *Bottom left*: correlation diagram between minimum masses of the inner and outer planet in pairs. *Bottom right*: total mass in planet pairs versus mass of the stellar hosts

ple of planet pairs orbiting higher-mass stars is dominated by high-mass planets (bottom right panel).

Compact systems of low-mass planets at short orbital separations are increasingly more difficult (and very observing-time consuming) to unveil with high statistical confidence in the detections around increasingly higher-mass stars, due to their very low-amplitude RV signals (e.g., Delisle et al. 2018; Udry et al. 2019; Hara et al. 2020). It is therefore difficult for Doppler surveys to establish whether the apparently higher low-mass, close-in planet multiplicity for later spectral types is indeed real or due to observational biases. For one thing, the highest planet multiplicity has been recorded for the solar-type star HD 10180, which hosts at least six, and up to nine!, planets, 5 or 6 inside the orbit of Mercury (Lovis 2011; Tuomi 2012). The fact that adjacent pairs of close-in low-mass companions appear to have rather similar (minimum) masses and similar spacings is instead quite intriguing, and awaits a clear explanation from a theoretical viewpoint.

The structure of peaks and deficits near resonance in the period ratio distribution can be interpreted in terms of a couple of alternative scenarios of formation and subsequent orbital evolution of low-mass multi-planet systems. A viable path is *in-situ* formation in gas-poor conditions, in the late stages of the disk's lifetime, with little or no orbital migration (e.g., Lithwick et al. 2012; Ogihara et al. 2018;

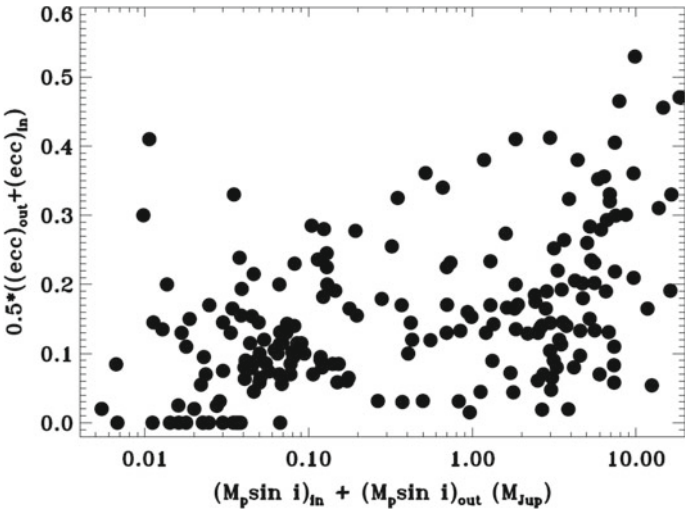

Fig. 3.37 Average eccentricity versus total mass for planet pairs in Doppler-detected multiple-planet systems

Terquem and Papaloizou 2019; Choksi and Chiang 2020, and references therein). Alternatively, such systems might have formed early in the gas-rich regions of the protoplanetary disk, undergone smooth disk-driven migration and resonance capture, and subsequently escaped resonance due to dynamical instability effects driven by a variety of other physical processes (e.g., Goldreich and Schlichting 2014; Izidoro et al. 2017; Lambrechts et al. 2019).

The average eccentricity of planet pairs is clearly correlated with the total mass (see Fig. 3.37), with low-mass multiples often compatible with having almost perfectly circular orbits.[9] As the Super Earths and Neptunes uncovered by Doppler surveys in multiple systems tend to have quite similar minimum masses (Fig. 3.36), it is tempting to conclude that they are also likely to be on nearly coplanar orbits, which could help in understanding whether their architectures have been shaped by 'clean' disk migration followed by phases of dynamical instability that retained both low eccentricities and low mutual inclinations (e.g., Esteves et al. 2020, and references therein), or they are produced by different *in-situ* formation conditions (e.g., MacDonald et al. 2020, and references therein).

Unfortunately, mutual inclination angles cannot be determined based on RV observations alone, unless planet-planet interactions produce detectable perturbations in the host star's motion beyond the simple superposition of Keplerian orbits. This has been possible in practice only for the two gas giants in a 2:1 resonance in the four-

[9] Note that the reported non-zero eccentricity values for low-mass companions are often compatible with zero within the error bars (not shown in the plot). It is in fact notoriously difficult to measure statistically significant small eccentricities for the low-amplitude RV signals induced by low-mass planets, as the estimated uncertainty on e scales as $\sigma_e = \frac{\sigma_K}{K}\left(\frac{2}{N_{\rm obs}}\right)^{1/2}$.

planet system around GJ 876, which were determined to have a mutual inclination of less than 5 deg (e.g., Rivera and Lissauer 2001; Bean et al. 2009; Rivera et al. 2010). The combination of RV data and relative HST astrometry (McArthur et al. 2010) allowed to measure a significant mutual inclination (30 ± 1 deg) between the two outer gas giants orbiting υ And. Most recently, the combination of RV data and Gaia-Hipparcos absolute astrometry allowed to infer that the hot super Earth found transiting around the naked-eye solar-type star π Men (Huang et al. 2018) must be on a significantly non-coplanar configuration with the outer, eccentric, massive giant planetary companion (Damasso et al. 2020; see also De Rosa et al. 2020 and Xuan and Wyatt 2020). Smooth disk migration likely explains the architecture of the resonant pair of gas giants around GJ 876 (e.g., Dempsey and Nelson 2018 and references therein). The detailed architectural properties of the υ And and π Men systems are more naturally explained by planet-planet scattering processes (e.g., Ford et al. 2008). Any attempt at observationally determining the mutual inclination of low-mass multiples in RV surveys remains so far elusive.

3.5.2 *Architecture of Kepler 'Multis': Global Patterns*

Two years after theWright et al. (2009) analysis, NASA's *Kepler* mission provided a new boost to the investigations of multi-planet demographics. Among the thousands of new exoplanet candidates, it uncovered a population of ~ 400 (as of April 2021) transiting multi-planet systems (Borucki et al. 2011; Lissauer et al. 2011b; Latham et al. 2011; Burke et al. 2014; Rowe et al. 2014) with orbital separations < 1 au. Based on statistical as well dynamical stability arguments, almost all of them are real ($\gtrsim 99\%$, e.g., Lissauer et al. 2012; Fabrycky et al. 2014). *Kepler* provided the first statistically robust evidence for the existence of a class of close-in, densely packed systems of small-size, low-mass planets, including record-holders Kepler-11 (six planets within Mercury's orbit; Lissauer et al. 2011a), Kepler-20 (six planets within Mercury's orbit, one of which non-transiting; Buchhave et al. 2016 and references therein), and Kepler-90 (eight planets within 1 au but 5 within Mercury's orbit; Shallue and Vanderburg 2018 and references therein). Such a large sample enables the robust identification of patterns in the intrinsic distributions of planets, which provide fundamental insights for models of the formation and evolution of planetary systems with a resolution that is not achievable by Doppler detections.

3.5.2.1 *Kepler* Singles Versus 'Multis'

The first question to ask is whether *Kepler*'s multi-planet systems (dubbed 'multis' thereafter) and those in which a single planet is known to transit (non-transiting planets could very well be present!) are drawn from the same parent population. The visual comparison of the population of singles and multis in the radius-orbital period space (Fig. 3.38) would make us infer this is indeed the case (except for hot Jupiters

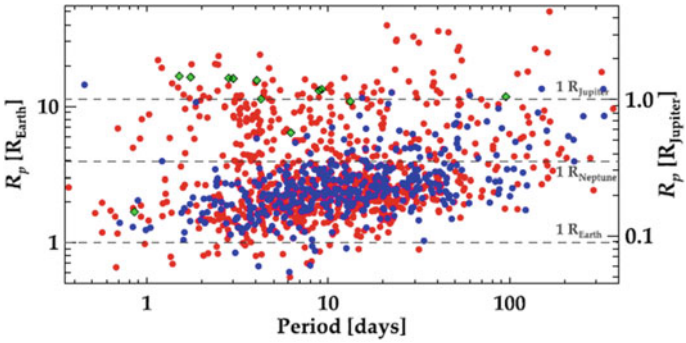

Fig. 3.38 The diagram of the planet radius versus orbital period for the planet candidates found during the first four months of the *Kepler* mission. Single candidate transiting planets are marked in red, multiple candidate transiting planets are marked in blue. The CoRoT planets known at the time are plotted in green. The figure was made by Samuel N. Quinn (Latham et al. 2011) and reproduced with permission from D. W. Latham

that tend to be 'lonely'; see, e.g., Latham et al. 2011; Steffen et al. 2012). Similarly, the radius valley seems to be present both for singles and multis (Fig. 3.39, left panel). Finally, the properties (particularly mass and metallicity) of the parent stars of *Kepler* singles and multis appear indistinguishable (an example is shown in the right panel of Fig. 3.39). This has brought many to conclude that the two populations are statistically the same (e.g., Xie et al. 2016; Munoz Romero and Kempton 2018; Zhu et al. 2018; Weiss et al. 2018a; for alternative views see, e.g., Brewer et al. 2018 and Anderson et al. 2021).

Small planet multiplicity within 1 au in the original *Kepler* field is not, however, independent of spectral type. We have already shown in Fig. 3.16 the dependence of occurrence rates with stellar mass originally uncovered by Howard et al. (2012). Several studies that followed confirmed the existence of the trend (e.g., Mulders et al. 2015a; Zhu et al. 2018). The latest work on the subject (Yang et al. 2020) has further confirmed this notion, establishing that planet hosts with 3000 K $\lesssim T_{\rm eff} \lesssim$ 5500 K are orbited typically by ~ 2.8 planets with $P < 400$ days, a number that drops sharply to ~ 1.8 for $T_{\rm eff} \gtrsim 6000$ K (Fig. 3.40).

3.5.2.2 The *Kepler* 'Dichotomy'

With such a large number of multi-planet systems identified by *Kepler*, the answer to the question: "What is the true multiplicity distribution of exoplanetary systems out to 1 au?" appears within reach. As the transit technique is by construction prone to miss planets in systems that are not almost perfectly coplanar, in order to model the planet number distribution one needs to make an hypothesis for both the the intrinsic multiplicity distribution and the mutual inclination distribution. Lissauer et al. (2011b) modeled the former as a uniform (or Poisson) distribution and the latter

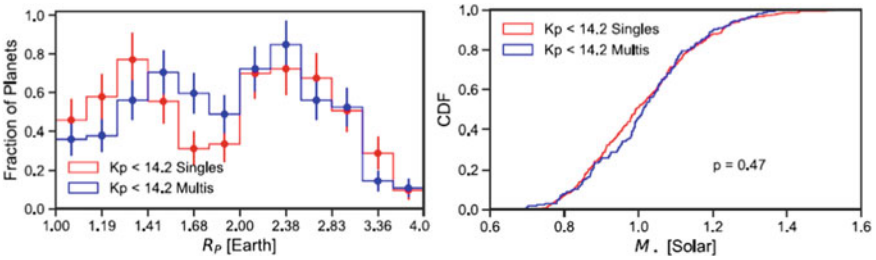

Fig. 3.39 *Left*: the distribution of planet radius for $K_p < 14.2$ mag systems with one (red) and multiple (blue) transiting planets. Only planets with $1\,R_\oplus < R_p < 4R_\oplus$ and $P_{orb} > 3$ days are shown. *Right*: cumulative distribution function (CDF) of the host-star masses for single and multi *Kepler* systems. Figure taken from Weiss et al. (2018a) and reproduced with permission from Lauren M. Weiss

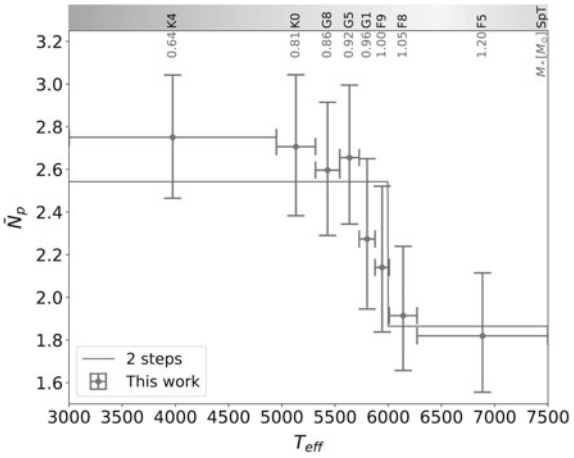

Fig. 3.40 Number of planets per star for *Kepler* planet hosts as functions of T_{eff}. Figure adapted from Yang et al. (2020) and reproduced with permission from Jia-Yi Yang

as a Rayleigh distribution, with a good match to all observed multiplicities except the singly transiting planets, whose occurrence was under-predicted by nearly 50%. The discrepancy could be reconciled if one considers the *Kepler* singles and multis as two distinct populations of planetary systems (orbiting stars with a broad range of spectral types and metallicities), a feature usually dubbed as the '*Kepler* dichotomy' (see Fig. 3.41): the first population is made up of dynamically 'cold', densely packed compact planetary systems with small mutual inclinations ($\sim 2°$), the second is composed of truly single close-in planets or dynamically 'hot' multi-planet systems (see cartoon of Fig. 3.42) with at least two companions with largely mutually inclined orbits (e.g., Johansen et al. 2012; Fang and Margot 2012; Tremaine and Dong 2012; Ballard and Johnson 2016; Munoz Romero and Kempton 2018; Mulders et al. 2018; He et al. 2019).

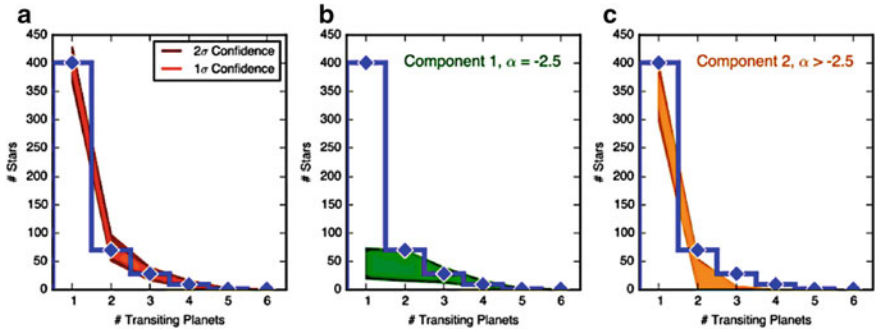

Fig. 3.41 Comparison between the *Kepler* multi-planet yield, in blue, to a best-fit power-law mixture model in multiplicity $\propto m^{\alpha}$ with 1σ and 2σ confidence levels. Panel **a** shows the result from the full model; panel **b** shows the contribution from a component with power-law index $\alpha = -2.5$, describing the high-multiplicity sector of the distribution; panel **c** shows the contribution from a component with power-law index $\alpha = -4$, describing the low-multiplicity sector of the distribution. Figure adapted from Ballard and Johnson (2016)

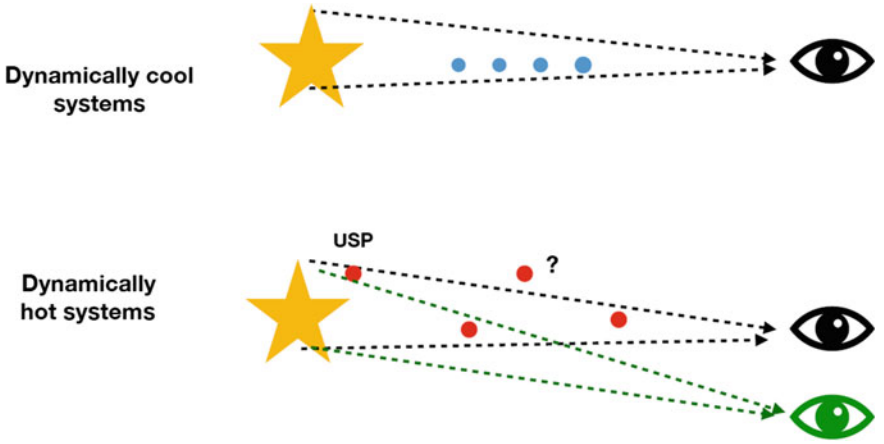

Fig. 3.42 Schematic drawing of the *Kepler* dichotomy: planetary systems densely packed and with small mutual inclinations are considered dynamically 'cold', whereas those composed of single close-in planets or several planets with large mutual inclinations are considered dynamically 'hot'

Recent work argues that the dichotomous model is not necessary, depending on the choice for the functional form of the multiplicity and mutual inclinations distributions (Gaidos et al. 2016; Bovaird and Lineweaver 2017; Sandford et al. 2019). The *Kepler* dichotomy might also artificially arise at least in part because of the increasingly lower detection efficiency of the *Kepler* pipeline with increasing planet multiplicity (Zink et al. 2019).

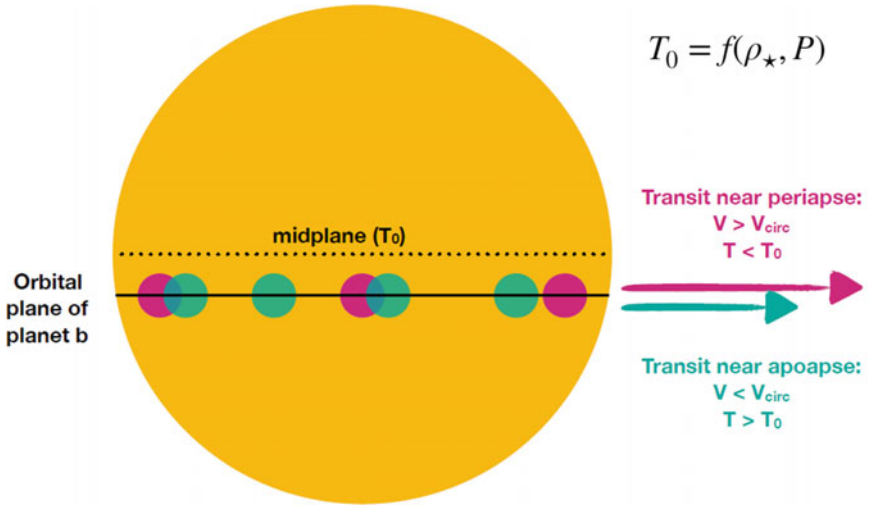

Fig. 3.43 Schematic drawing of how the transit duration, T, can change according to the orbital parameters. Here T_0 represents the transit duration corresponding to a central ($b = 0$) transit for a planet on a circular orbit ($e = 0$)

3.5.2.3 Eccentricities and Mutual Inclinations

A possibly convergent picture on the dynamical differences and similarities between *Kepler* systems with different multiplicity can be drawn when considering the combined information coming from in-depth studies of both eccentricity and mutual inclination distributions. The full duration of a transit can be expressed as:

$$T_{\rm dur}/T_0 = \sqrt{(1 + R_p/R_\star)^2 - b^2}\,\frac{\sqrt{1-e^2}}{1 + e\sin\omega}, \tag{3.15}$$

with $T_0 \simeq 13\,{\rm hr}\,(P/{\rm year})^{1/3}\,(\rho_\star/\rho_\odot)^{-1/3}$ the transit duration corresponding to a central ($b = 0$) transit for a planet on a circular orbit ($e = 0$). See the cartoon of Fig. 3.43 for a visual description. It is therefore possible to study the distribution of $T_{\rm dur}/T_0$ to infer the underlying distribution of eccentricities. Early attempts at determining the eccentricity distribution of *Kepler* multis (e.g., Moorhead et al. 2011; Kane et al. 2012; Wu and Lithwick 2013) were hampered by the pre-Gaia limited knowledge of the host stars. With more precisely determined stellar properties, the method has been applied by several authors (Van Eylen et al. 2015; Xie et al. 2016; Mills et al. 2019; Van Eylen et al. 2019). The clear, statistically robust picture portrayed by these studies is that *Kepler* multis are found on nearly-circular orbits (median $e \sim 0.05$), while *Kepler* systems with one detected transiting planet exhibit a large eccentricity dispersion, with a study-dependent median e in the range 0.15–0.3 (see Fig. 3.44 for an example). There is tentative evidence that the most eccentric *Kepler* singles might

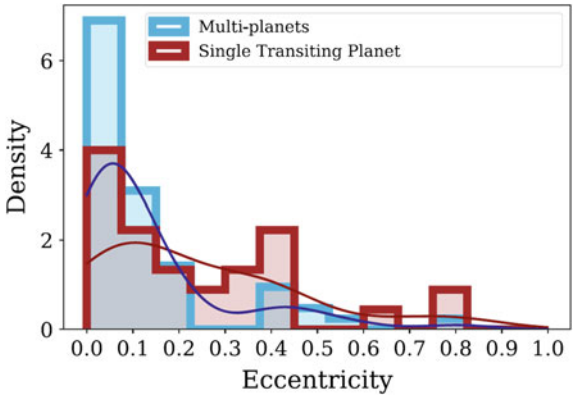

Fig. 3.44 Density histogram of the eccentricity distribution of *Kepler* systems with multiple transiting planets and systems with a single transiting planet. The bins have an arbitrarily chosen width of 0.075. Solid lines indicate kernel density estimates. Multi-planet systems clearly have a higher density of low eccentricities. Figure adapted from Van Eylen et al. (2019) and reproduced with permission from Vincent Van Eylen

preferentially orbit more metal-rich stars (Mills et al. 2019). We further elaborate on this point in Sect. 3.6.2.

The normalized transit duration ratio:

$$\xi = \frac{T_{\mathrm{dur,in}}/P_{\mathrm{in}}^{1/3}}{T_{\mathrm{dur,out}}/P_{\mathrm{out}}^{1/3}} \tag{3.16}$$

contains information on the mutual inclination of a planet pair in a multi-planet system (the subscripts in and out identify the inner and outer companion). Studies of the ξ distribution for *Kepler* multis (Fang and Margot 2012; Tremaine and Dong 2012; Fabrycky et al. 2014) agree on the fact that the mutual inclinations between *Kepler* multis can be described by a Rayleigh distribution with a dispersion of a few degrees (see Fig. 3.45).

More recent analyses (e.g., Zhu et al. 2018; He et al. 2020) have further corroborated the notion that mutual inclinations and eccentricities of *Kepler* multis are strongly correlated, and quantified the power-law dependence of the two distributions with multiplicity m ($\propto m^{\gamma}$, with $\gamma \sim -1.7/-2.0$ in both cases),[10] providing additional evidence for the solution of the *Kepler* dichotomy. Finally, Dai et al. (2018a) have uncovered a clear trend of increasing mutual inclination in planet pairs as a function of decreasing orbital distance of the innermost planet (for more details, see Sect. 3.7.6).

[10] Studies based on RV multis or a combination of transiting and RV multis have also identified an anti-correlation between orbital eccentricity and multiplicity (Limbach and Turner 2015; Zinzi and Turrini 2017; Turrini et al. 2020; Bach-Møller and Jørgensen 2021).

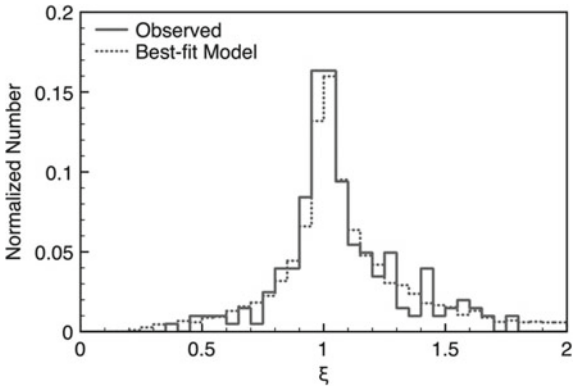

Fig. 3.45 Histograms of normalized transit duration ratios (Eq. 3.16). The solid histogram is the observed distribution, the dashed histogram is the distribution from simulated detections based on the best-fit model described in (Fang and Margot 2012). Figure reproduced with permission from Jean-Luc Margot

3.5.3 Architecture of Kepler 'Multis': Planet-to-Planet Patterns

Several other studies of *Kepler* exoplanetary systems have identified additional patterns in their observed architectures, particularly in relation to the intra-system variations of sizes and spacings, which are potentially very constraining for formation and evolution models.

3.5.3.1 Size Ordering and Period Ratios

The two panels of Fig. 3.46 show *Kepler* multis containing three or more, four or more planets ordered by orbital period or orbital separation of the innermost planet as well as stellar mass (Fabrycky et al. 2014; Weiss et al. 2018b). Visually, it appears that the largest planets are typically those with longer periods. It is also not difficult to get the impression that generally systems appear to have rather similar sizes and regular spacings.

Using a sample of $\sim$ 900 planets in 365 *Kepler* multis, Ciardi et al. (2013) studied the relative sizes of the planetary radii for all planet pairs, finding that when at least one planet in a pair has radius $\gtrsim 3\ R_\oplus$ then for $\sim$ 70% of the pairs the outer planet is larger than the inner planet. This number is almost the same as the one derived when looking at the minimum mass hierarchy in the RV sample of multis (Sect. 3.5.1.2). For pairs with both radii below $3\ R_\oplus$ no such size ordering was recorded.

The second much discussed pattern in orbital architecture of *Kepler* multis is related to the period ratio distribution. The histogram of period ratios for all pairs of planets with radii $< 4\ R_\oplus$ (Fig. 3.47) clearly shows that most of the systems are not in or close to mean motion resonances, but but there are excesses of systems just wide of the 3:2, 2:1, and 5:3 (and possibly 3:1) commensurabilities, and corresponding deficits just short of these resonances (Lissauer et al. 2011b; Delisle and Laskar 2018; Fabrycky et al. 2014; Xu and Lai 2016; Choksi and Chiang 2020). The similarity

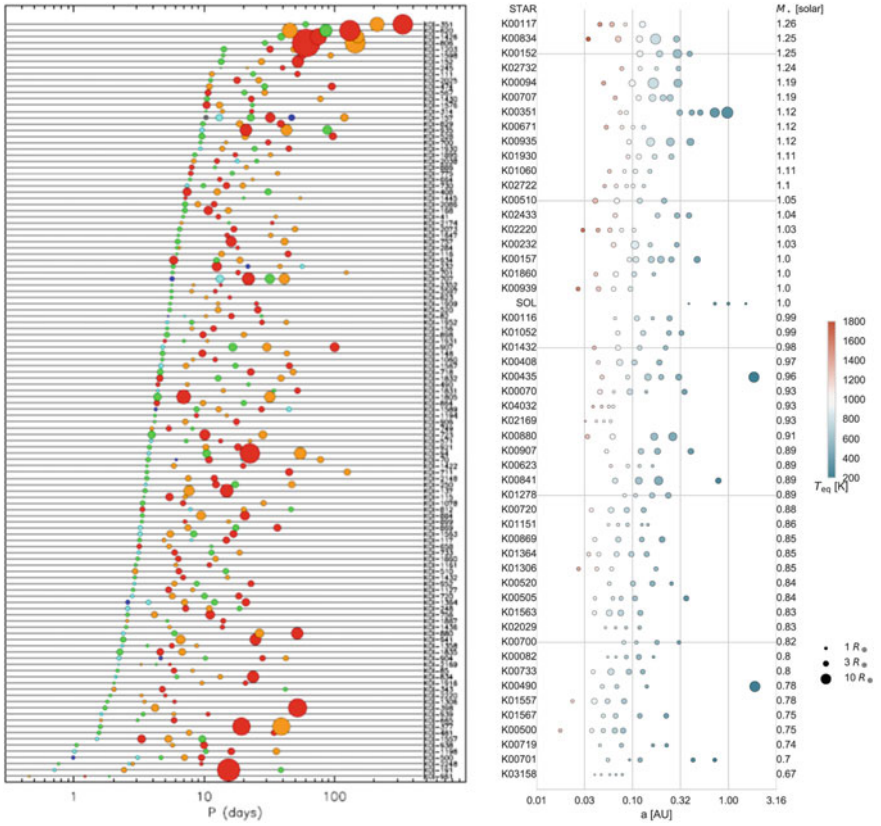

Fig. 3.46 *Left*: examples of architectures of *Kepler* multi-planet systems from Fabrycky et al. (2014). Planets are represented with circles, whose size is proportional to their radius and are colored by decreasing size within each system. The systems are ordered based on the orbital period of the inner planet. Figure reproduced with permission from Daniel C. Fabrycky. *Right*: examples of architectures of *Kepler* multi-planet systems with at least four transiting planets from Weiss et al. (2018b). Planets are represented with circles, whose size is proportional to their radius. Color indicates their equilibrium temperature. The systems are ordered based on the stellar primary mass, which is reported on the right side. The rocky planets of the Solar System are also included for comparison. Figure reproduced with permission from Lauren M. Weiss

with the histogram of Fig. 3.34 based on the RV sample of multis is compelling. The minimum period ratio is also very similar, $\simeq 1.2$ and $\simeq 1.26$ for the *Kepler* and RV multis, respectively.

3.5.3.2 The 'Peas in a Pod' Patterns

The visual appearance of similar sizes and regular spacings implies that sizes and period ratios of pairs in the same systems should be correlated. Weiss et al. (2018a) found exactly such a correlation in both parameters (Fig. 3.48). The null hypothesis

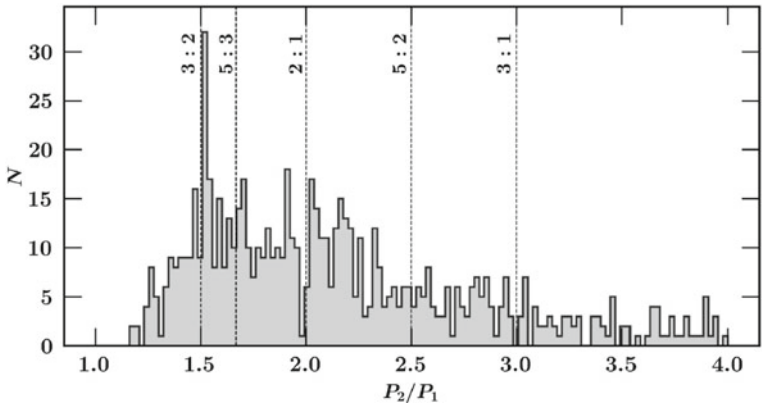

Fig. 3.47 Period ratios P_2/P_1 for all pairs of sub-Neptunes with $R_p < 4R_\oplus$ (the subscript 1 denoting the inner member of the pair and 2 the outer). N denotes the number of systems in a bin. Data taken from the NASA Exoplanet Archive on August 2019. Figure adapted from Choksi and Chiang (2020) and reproduced with permission from Nick Choksi

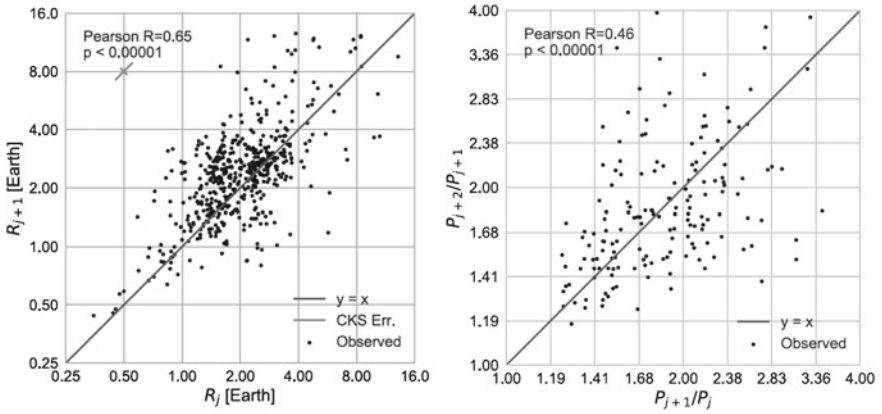

Fig. 3.48 *Left*: the radius of a planet versus the radius of the next planet out in *Kepler* multi-planet systems. *Right*: the orbital period ratio of the outer planets versus the orbital period ratio of the inner planets in *Kepler* systems with three or more planets. In both cases high Pearson correlation coefficients correspond to a very low probability of no correlation. Figures taken from Weiss et al. (2018b) and reproduced with permission from Lauren M. Weiss

of no correlation was tested in detail by Weiss et al. (2018b), based on a bootstrap procedure in which stars and number of planets were preserved, but sizes and orbital periods were randomly drawn from the observed distributions (Fig. 3.48, left-hand panel). The correlation was found to be much weaker for both parameters with respect to what was seen in real systems (Fig. 3.48, right-hand panel). The clear pattern of similar sizes and regular spacings was then termed by Weiss et al. (2018b) "peas in a pod". Strong intra-system uniformity was also shown by Millholland et al. (2017)

in mass-radius space for a sample of *Kepler* multis with mass measurements from transit-timing variations. It is very interesting to note the close similarity of the size correlation with the tight minimum-mass correlation plot of Fig. 3.36 for the RV sample of low minimum-mass multis. Finally, Weiss et al. (2018b) also found evidence for a correlation between the average planet size in an adjacent pair and the period ratio of the pair, which also closely resembles the analogous plot (in minimum mass vs. period ratio) of Fig. 3.36 for the RV sample, although on an overall different scale of period ratios.

The nature of the "peas in a pod" pattern of correlations has been the subject of a debate in the most recent literature, with evidence brought forward in support of both its astrophysical origin or it being produced by selection effects due to observational biases (He et al. 2019; Murchikova and Tremaine 2020; Weiss and Petigura 2020; Zhu 2020; Jiang et al. 2020). While the jury is still out, investigations based on state-of-the-art population synthesis models used for generating forward models of the *Kepler* survey (EPOS, Mulders et al. 2018; SysSim, Hsu et al. 2018) appear to indicate the former interpretation might be preferable (He et al. 2020; Gilbert and Fabrycky 2020).

Finally, *Kepler* multis are not only regularly, but also very closely spaced. An empirically-determined representation of the median spacing of a pair to ensure its long-term dynamical stability is (Pu and Wu 2015):

$$\Delta = 2.87 + 0.7 \log\left(\frac{t}{P_{\rm in}}\right) + 2.4\left[\left(\frac{\sigma_e}{R_H/a_{\rm in}}\right) + \left(\frac{\sigma_i}{4R_H/a_{\rm in}}\right)\right] \tag{3.17}$$

In the expression, t is the physical stability timescale, $P_{\rm in}$ the orbital period of the innermost planet, R_H is the mutual Hill radius of a planet pair (see Eq. 22 in Chap. 1) , $a_{\rm in}$ is the semi-major axis of the innermost planet, and σ_e and σ_i are the multiplicity-dependent dispersions of orbital eccentricities and mutual inclinations among the planets. The spacing threshold for dynamical stability decreases from $\Delta \sim 20$ to $\Delta \sim 12$ for $n = 2$ and $n = 5$, respectively,[11] and it is rather close to the typically observed values for *Kepler* multis ($\Delta \sim 20$, see, e.g., Fang and Margot 2012; Pu and Wu 2015; Weiss et al. 2018b). One is then induced to conclude that *Kepler* multis are indeed dynamically packed, and systematically close to empirical stability limits. The major caveat in drawing this conclusion is the fact that for the overwhelming majority of *Kepler* multis dynamical mass measurements are not available, therefore the calculation of R_H relies on the use of empirical mass-radius relationships.

3.5.3.3 Possible Interpretations

The eccentricity, mutual inclination and period ratio distributions for *Kepler* small multi-planet systems (including those containing ultra-short-period companions), and the ordering of and correlations between size and spacings bear key insights on

[11] Delta is measured in mutual Hill radii R_H

the variety of channels for planet formation and dynamical evolution of planetary systems. A variety of mechanisms have been invoked to reproduce the mixture of dynamically hot and cold configurations of variable multiplicity in the *Kepler* sample. They all likely contribute to a higher or lesser degree to shape the details of the distributions as a function of multiplicity. These include chaotic secular interactions (Petrovich et al. 2019; Volk and Malhotra 2020), low-eccentricity migration via planet-planet scattering (Pu and Lai 2019), interactions with an outer giant planet (e.g., Johansen et al. 2012; Huang et al. 2017; Mustill et al. 2017; Becker and Adams 2017; Pu and Lai 2018; Poon and Nelson 2020; Masuda et al. 2020, effects of primordial host star obliquity and oblateness, and planetary obliquity tides (e.g., Spalding and Batygin 2016; Li and Lai 2020; Becker et al. 2020; Millholland and Laughlin 2019; Millholland and Spalding 2020; Spalding and Millholland 2020), disk migration of (not necessarily) resonant chains that subsequently disrupt due to a variety of mechanisms (e.g., Baruteau and Papaloizou 2013; Goldreich and Schlichting 2014; Pu and Wu 2015; Chatterjee and Ford 2015; Izidoro et al. 2017; Lambrechts et al. 2019; Pichierri and Morbidelli 2020), or more or less in-situ formation (e.g., Hansen and Murray 2013; Matsumoto and Kokubo 2017; Lee and Chiang 2017; Terquem and Papaloizou 2019; MacDonald et al. 2020). Additional discussion can be found in Chap. 1.

3.6 Eccentricity and Obliquity

Let us now further discuss the distributions of specific parameters, namely eccentricity and obliquity, which can be considered optimal tracers of the *dynamical temperature* of planetary systems.[12] This concept was introduced in Sect. 3.5.2.2: exoplanet systems with orbits that are almost circular and are well aligned with the host stars' equatorial planes are defined as dynamically 'cool', whereas those that present misaligned and eccentric orbits are dynamically 'hot' (see Fig. 3.42). The distributions of these parameters and how they depend on stellar and planetary properties play and important role to shed light on planet-formation mechanisms and the subsequent evolution of planetary orbits (Winn and Fabrycky 2015).

3.6.1 Eccentricities of Giant Planets

The analysis of the eccentricity as a function of the orbital period or the semi-major axis is one of the first diagnostics of the statistical properties of the exoplanet population, which has been utilized since the early days of exoplanetary science (see Fig. 3.49, where the planets of the Solar System are in the lower-right quadrant of

[12] This section is based on the lecture performed in May 2019 by A. Howard, who thanked Josh Winn for many slides that he presented during his lecture.

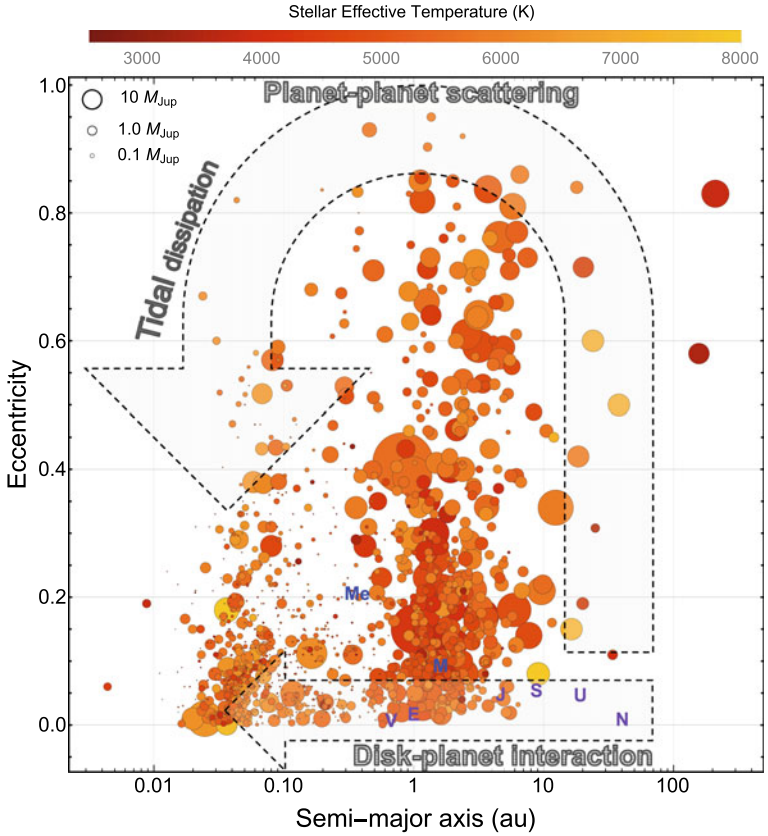

Fig. 3.49 Diagram of the orbital eccentricity versus the semi-major axis of known exoplanets. The planets are represented by circles, whose size is proportional to their mass, m_p, or $m_p \sin i$. The error bars have been suppressed for clarity. Color indicates the effective temperature of their parent stars. Data were taken from the NASA Exoplanet Archive in September 2020. The positions of the Solar-system planets are also reported by the initials of their names. Figure inspired by a similar plot from J. Winn

this semi-major axis – eccentricity diagram). All giant planets in the Solar System have very low-eccentricity orbits, and are found at at wider orbital separations than the terrestrial planets. We would expect that to be the case for exoplanetary systems as well, because, in order to become a giant planet, a core of solid material has to grow to a certain critical size, which is roughly ten times the mass of the Earth. At that critical size, the surface gravity of the planet becomes sufficient to start accreting hydrogen and helium. As we learned from Chap. 1, this phenomenon can only happen far away from the Sun, beyond the so-called *snow line*, because there are a lot more solid materials there (especially volatile chemical compounds with freezing points $> 100\,\mathrm{K}$, such as water, ammonia, methane, etc.) that aggregate to form large-core protoplanets, which subsequently become giant planets. Indeed,

the initial expectation from theory is that the orbits of these giant planets should be roughly circular, because the effective frictional force, which exists for planets that are orbiting within a massive disk of gas and dust, would produce an effective damping of any primordial eccentricity. Instead, examining Fig. 3.49, the observational evidence tells a different story:

- first, there are many giant planets on very eccentric orbits (for example, HD 80606 b has $e \approx 0.93$; Naef et al. 2001). In our Solar system, these kind of eccentricities are typically associated with comets;
- second and even more surprising, there are giant planets existing in abundance at short orbital separations much inside the snow line, as close as $\approx 0.01 - 0.1$ au.

We already saw (Chap. 1 and Sect. 3.3) that these giant planets are known as hot and warm Jupiters and likely formed in the outer regions of the protoplanetary disk (where Jupiter did in the Solar system), but then through some processes they have *migrated* from their initial locations to where we see them today.

As already discussed in this book (see Chap. 1, Sect. 2.4 and 3.2; Chap. 2, Sect. 3.2; see also Sect. 3.5 of this Chapter), a number of physical mechanisms have been proposed that are capable of evolving significantly the primordial orbit of a giant planet, shrinking it and/or exciting its eccentricity. The two main ones are:

- early interactions between a giant planet and the protoplanetary disk in which it formed. These can lead to the loss of energy and angular momentum from this planet to the disk, resulting in the planet spiraling towards the central star, turning it into a hot Jupiter (Lin et al. 1996; Ward 1997);
- *planet-planet scattering* in multiple systems (e.g., Rasio and Ford 1996; see also Davies et al. 2014 and references therein). Gravitational interactions between planets in a system can lead to a chaotic evolution of orbital elements that can cause planet orbits to cross. When that happens, giant planets rarely collide, but instead gravitationally scatter, resulting in ejection of some of the companions while others remain on high-eccentricity orbits. Through tidal dissipation mechanisms such eccentric orbits are then shrunk and circularized.[13]

To understand which of the two models best explains the observed distributions, we can examine the orientation of the planetary orbits. If planet-planet scattering is the process that produces hot Jupiters, the same scattering encounters will randomize to some degree the orbital planes, whereas disc-planet interactions keep the system coplanar throughout the whole migration process and we will see flat architectures. These expectations are well supported by numerical simulations. For example:

- Marzari and Nelson (2009) ran hydrodynamic simulations to investigate the dynamical evolution of a Jupiter-mass planet injected into an orbit highly inclined

[13] Similar to this case is the Kozai-migration mechanism, in which a planetary system is dynamically perturbed by a distant third body, which could be a companion star or a massive planet (see, for example, Wu and Murray 2003). Kozai oscillations can produce a very broad range of final orientations, primarily eccentric, misaligned and even polar and retrograde orbits are possible (Fabrycky and Tremaine 2007).

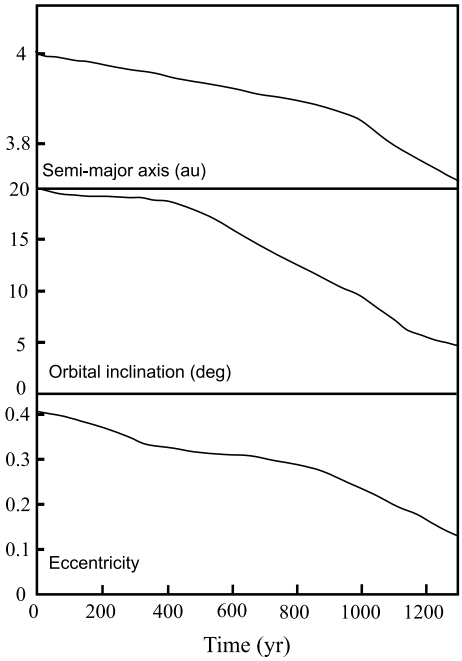

Fig. 3.50 Simulation of the evolution of a giant planet initially in an orbit inclined with respect to a circumstellar disk. The planet started on an orbit with semi-major axis equal to 4 au, eccentricity 0.4, and inclination 20°. The exchange of angular momentum between the disk and the planet causes these three planetary orbital parameters to evolve significantly over the ≈ 1000 year timescale of the simulation. Figure adapted from Marzari and Nelson (2009)

with respect to its protoplanetary disk. They found that, independently of the initial values of the semi-major axis and eccentricity of the planet, the eccentricity and inclination of its orbit are rapidly damped on a timescale of the order of 10^3 year, see Fig. 3.50.

- Chatterjee et al. (2008) performed simulations of gravitational planet-planet scattering, in systems containing three giant planets, orbiting solar-mass stars, on initially near-circular orbits and no gas disk. They found that in all of these systems, at least one planet is eventually ejected before reaching a stable configuration. In 20% of the cases, two planets are lost through ejections or collisions, leaving the system with only one giant planet, thus predicting the existence of many systems with a single eccentric giant planet. The exact distribution of eccentricities for the final remaining planets in stable orbits, after a secular evolution (≈ 10^9 year), depends on the choice and range of the initial mass distribution but is in general similar to what we observe in reality. The authors also found that it is possible to scatter some planets into orbits with low perihelion distances and that the inclination distribution of such planets could be significantly broadened. Therefore, these scattering events tend to amplify any initially small misalignments.

Indeed, planet–planet scattering processes can reproduce much of the observed distribution of exoplanet eccentricities for a wide range of initial conditions (Ford et al. 2008; Jurić and Tremaine 2008; Nagasawa et al. 2008; Matsumura et al. 2010; Raymond et al. 2010; Dawson and Murray-Clay 2013; Carrera et al. 2019). Furthermore,

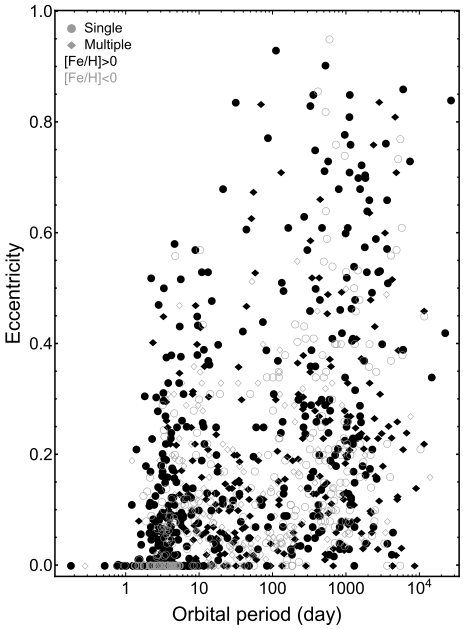

Fig. 3.51 Diagram of the orbital eccentricity versus orbital period of known exoplanets. The error bars have been suppressed for clarity. Most of the high-eccentric, single planets are found around high-metallicity ([Fe/H] > 0) stars, as noted by Buchhave et al. (2018). Data taken from the NASA Exoplanet Archive on September 2020

the initial metal content of protoplanetary disks also likely plays a role in the structure and architecture of planetary systems: high-metallicity systems are in fact expected to contain multiple gas giants that can perturb each other gravitationally, leading to enhanced planet–planet scattering rates. The eccentricity of cold gas giants should, therefore, increase with host-star metallicity and this is also observed (e.g., Bryan et al. 2016; Buchhave et al. 2018; see Fig. 3.51).

We would also expect that whatever mechanism perturbs the eccentricities of giant planets and/or produces hot Jupiters may also change their orbit orientation in space. Therefore, the angle between a planet's orbital axis and its host star's spin, which is also known as *spin-orbit obliquity* or simply *orbital obliquity*, ψ, represents a key parameter. Determining ψ for a statistically significant sample of exoplanetary systems, preferably spanning a range of precise parent-star ages, can allow us to figure out what the primary physical phenomenon related to the migration process of a giant planet is. We discuss in Sect. 3.6.3 the inferences obtained based on present-day statistics of ψ measurements.

3.6.2 Eccentricities of Super Earths and Sub-Neptunes

The *Kepler* space telescope (Borucki et al. 2010), with its exquisitely precise photometry, has given an enormous contribution to the study of planets with sizes smaller than that of our Jupiter. The *horn of plenty* of small exoplanets unveiled by *Kepler*

has allowed theoreticians to produce robust statistical inferences on the abundances and properties of planetary systems. As we have seen in Sect. 3.3.2 and Sect. 3.4, the analysis of *Kepler* data has in particular shown how the most common planets in the Galaxy are sub-Neptunes and super-Earths.

As already discussed in Sect. 3.5.2.3, the eccentricity distribution of small-size planets in the Kepler field can be studied based on transit duration statistics (see Eq. 3.15). Using this technique, Xie et al. (2016) derived the eccentricity distributions of roughly 700 reliable *Kepler* candidates (Mullally et al. 2015), finding an interesting dichotomy. Single transiting planets have a large mean eccentricity ($\bar{e} \approx 0.3$), whereas planets in multiple systems are on nearly circular orbits (mean eccentricity $\bar{e} < 0.07$. Using a larger sample of validated *Kepler* planets (Coughlin et al. 2017) and benefiting from Gaia parallaxes to derive high-precision measurements of stellar radii (Gaia Collaboration 2016a, b, 2018), Mills et al. (2019) performed a new statistical study of the eccentricity distribution of small planets, confirming that systems with only a single transiting planet have a higher mean eccentricity ($\bar{e} \approx 0.2$), compared to those with multiple transiting planets ($\bar{e} \approx 0.05$). Mills et al. (2019) also found evidence that *Kepler* single planets with high eccentricity preferentially orbit around high-metallicity ([Fe/H] > 0) stars, extending to the regime of Super Earths and sub-Neptunes the same inference already gathered by earlier studies focused on gas giants (Dawson and Murray-Clay 2013; Buchhave et al. 2018).

The eccentricity dichotomy can be possibly understood by considering that high-metallicity environments favor the formation of giant planets. Dynamical interactions between these giant planets and inner systems can excite the eccentricities and, at the same time, can decrease the apparent multiplicity of close-in planets, which are also subjected to mutual inclination excitation (e.g., Mustill et al. 2017; Pu and Lai 2018; Masuda et al. 2020; Poon and Nelson 2020, and references therein). On the other hand, close-in multi-planet systems which are not dynamically heated by cold gas giants may not reach sufficiently high eccentricities and mutual inclinations through self-excitation mechanisms (e.g., dynamical instabilities) during the late stages of formation (e.g., Becker and Adams 2016; Poon et al. 2020).

3.6.3 Measuring the Orbital Obliquity

As mentioned in Sect. 3.6.1, the relative role of the two main mechanisms that can act to shrink the orbits of giant planets, planet-planet scattering and disk-planet interactions, can be probed using measurements of stellar obliquities, as proxies of the orbital (mis)alignment of the planets. The reader may wonder what hope do we have of measuring the obliquity ψ of the parent stars and therefore the orientations of the planets since we cannot resolve the star and the planet and directly see in which way the star is rotating and in which way the planet is orbiting. The class of transiting planets comes crucially to our aid in this case.

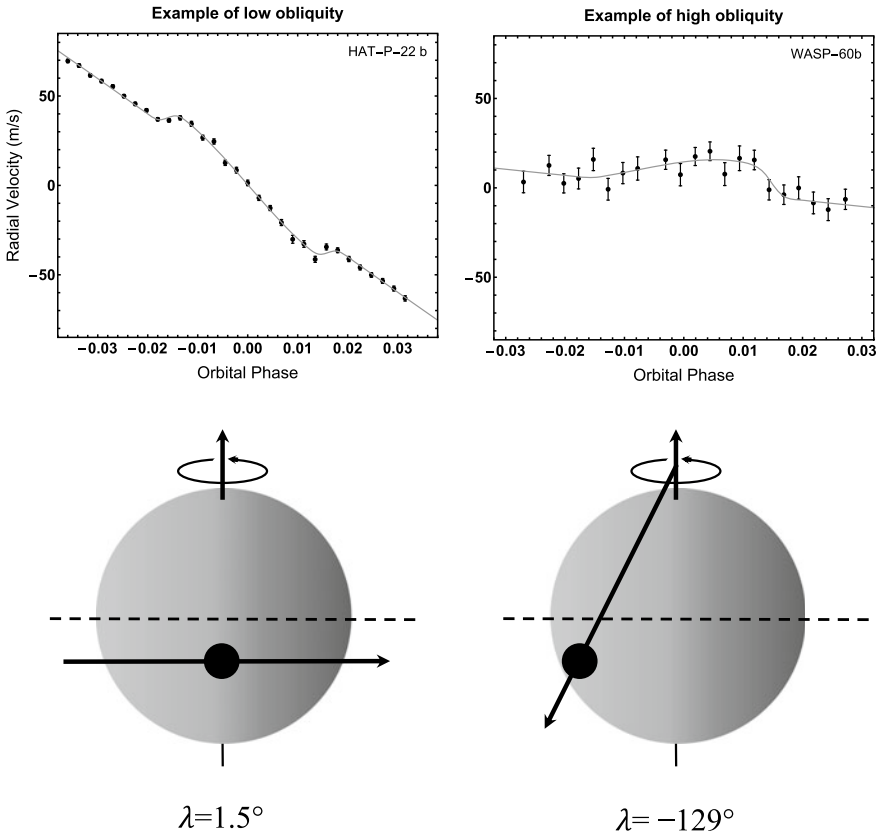

Fig. 3.52 The Rossiter-McLaughlin effect produced by two different transiting hot Jupiters, HAT-P-22 b and WASP-60 b. The phase-folded radial-velocity data (black points with error bars) were measured with the high-resolution spectrograph HARPS-N during planetary-transit events; superimposed are the best-fitting radial-velocity models (gray curves) (Mancini et al. 2018). The two planets have roughly the same impact parameter, but very different transit trajectories, which highlight the dependence of the Rossiter-McLaughlin radial velocity signature on λ

3.6.3.1 The Rossiter-McLaughlin Effect

The spin-orbit obliquity, ψ, which we learned is the angle between a planet's orbital axis and its host star's spin, is, unfortunately, not easy to determine. However, its sky projection, λ, is a quantity that is commonly measured for stars hosting transiting exoplanets through the observation of the Rossiter-McLaughlin (RML) effect (a well-known phenomenon in the context of eclipsing-binary stars), by using high-precision RV instruments. Usually, we see a transit as the apparent drop in brightness of the parent star as the planet gets in front of it (see Sect. 3.2.2.1), but if we monitor the transit event with a high-resolution spectrograph, which is sensitive to red or blue shifts of a hundred parts per million or better, then the RV time-series during transit would look similar to those in the top panels of Fig. 3.52.

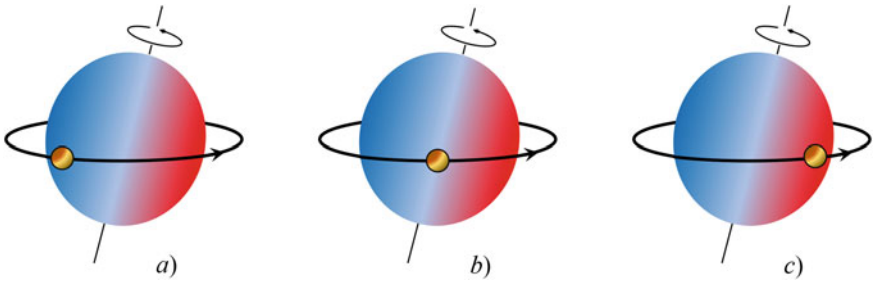

Fig. 3.53 A sketch of the Rossiter-McLaughlin effect, which can be measured during a planetary-transit event. During its rotation around the parent star, a transiting planet will block out more of the star's rotationally blue-shifted light immediately after the transit ingress (panel *a*) and more of its red-shifted light before the complete egress (panel *c*). This phenomenon changes the radial velocity profile of the parent star according to the planet's orbital phase. Figure inspired by a similar figure from Perryman (2018)

The distortions in the RV measurements on top of the Doppler shifts induced by the stellar orbital motion (see Sect. 3.2.1) occur because the parent star is rotating and so the half of the star approaching looks slightly blue-shifted, whereas the receding half looks slightly red-shifted. While transiting, a planet blocks first a small portion of the stellar surface approaching us, and then a fraction of the receding one. The stellar spectrum therefore becomes first anomalously red-shifted and then blue-shifted. This anomaly is null when the planet crosses the symmetry axis of the star. When the transit is over the effect disappears (see Fig. 3.53). By tracking the Doppler shift of the star throughout a complete planetary-transit event and by accurately measuring the shape of the RML effect, we can measure the projected stellar obliquity. If we are facing a system for which the planet's orbital plane is well aligned with the equatorial plane of the host star, i.e. a system with a low obliquity, we will measure a redshift and then a blueshift as in the top left panel of Fig. 3.52. However, in case of strong spin-orbit misalignment the planet could be spending, for example, all of its time covering the blue-shifted surface of the star and then we would only observe an anomalous redshift as in the case shown in the top right-hand panel of Fig. 3.52. Several cases of even very high-obliquity configurations have been found, including retrograde orbits (e.g., Winn et al. 2009; Narita et al. 2009).

In order to obtain an accurate modeling of the RM effect of a given planetary system and, therefore, a correct estimation of λ, it is crucial to obtain a stable out-of-transit baseline. This means that, similar to the case of a photometric transit light curve, one has to start observing the target at least ~ 60 min before ingress and ~ 60 min after egress.

The expected RV amplitude of the RML effect is approximately equal to (Winn 2010)

$$\Delta K \approx \left(R_{\rm p}/R_\star\right)^2 \sqrt{\left(1-b^2\right)} v \sin i_\star \overset{b\simeq 0}{\approx} 52.8\,{\rm m\,s^{-1}} \left(\frac{R_{\rm p}}{R_{\rm Jup}}\right)^2 \left(\frac{R_\star}{R_\odot}\right)^{-2} \left(\frac{v \sin i_\star}{5\,{\rm km\,s^{-1}}}\right), \tag{3.18}$$

where $v \sin i_\star$ is the projected rotational velocity of the parent star and b is the impact parameter, i.e. the sky-projected distance at the conjunction between the planet and the star ($b = 0$ for a central transit). This means that giant planets orbiting around rapidly rotating stars are the best objects to observe to get precise measurements of λ, exploiting the RML effect.

3.6.3.2 Doppler Tomography

The detection of the RML effect in transiting-planetary systems as an anomalous Doppler shift of the stellar atmospheric lines is routinely obtained as far as stellar rotation is not the dominant line broadening mechanism. However, if the parent star rotates quickly ($\gtrsim 10\,\mathrm{km\,s^{-1}}$), there will be a distortion of the stellar line profiles that change as the planet blocks parts of the rotating stellar surface during the transit. In this case, as noted by Collier Cameron et al. (2010a), the parameters derived from modeling the RML effect can be severely affected by systematic errors, which arise from this time-variable asymmetry of the spectral lines. By monitoring a complete planetary transit (including the out-of-transit baseline) with high-cadence and high-resolution spectroscopy, we can detect such a distortion, also known as 'Doppler shadow', moving across the line profiles. By mapping these line profile variations as a function of stellar rotational velocity and orbital phase, the Doppler tomography technique allows isolating and tracking the component of the starlight blocked by a planet as it transits the host star, which can be self-consistently expressed as a function of the projected spin-orbit misalignment angle.

In practice, the method of Doppler tomography entails subtracting the mean, out-of-transit, line shape (i.e. the representation of the unobscured starlight) from all the in-transit spectra, so that any dark inhomogeneity on the stellar surface (corresponding to the missing starlight blocked by the transiting planet) will pop up as a positive bump. In this way, we will see the bump appearing at ingress, moving along the transit chord and disappearing at egress. As a result, in this mean line profile residual map we will detect a trail that corresponds to the Doppler shadow of the transiting planet (see Fig. 3.54). We can, then, model the shadow with a Gaussian having a width of $(R_\mathrm{p}/R_\star)v \sin i_\star$ and an area of $1 - f(t)$, where $f(t)$ is the flux blocked by the planet, centered on $v_\mathrm{p}(t)$. The latter quantity is the projected rotational velocity for the region of the star occulted by the planet (Cegla et al. 2016; Zhou et al. 2016), which depends on $v \sin i_\star$ and λ.

Doppler imaging techniques have been effectively applied to measure the spin–orbit angles of planetary systems with hot, fast-rotating primaries (e.g., Collier Cameron et al. 2010a, b; Miller et al. 2010; Brown et al. 2012; Gandolfi et al. 2012; Hartman et al. 2015; Gaudi et al. 2017). In the case of ultra-hot Jupiters ($T_\mathrm{eq} \gtrsim 2000\,\mathrm{K}$), the *atmospheric* RML effect can be detected (Borsa et al. 2019). It corresponds to a deviation of the in-transit RVs from the classical RML effect that occurs when the atmosphere of the planet is intercepted by the mask used to create the stellar cross-correlation functions or mean line profile. The atmospheric trace will appear in the tomographic map of the line profile residuals after removal of

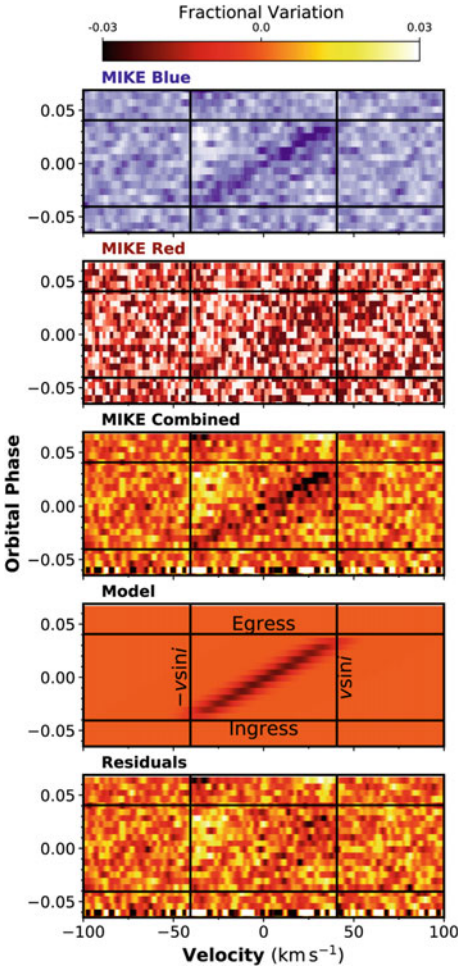

Fig. 3.54 The Doppler tomographic transit of the brown dwarf HATS-70 b, as measured by Zhou et al. (2019a) with the two cameras of the MIKE instrument on the 6.5 m Magellan Clay telescope. HATS-70 b successively blocks parts of the rotating stellar surface, inducing a 'Doppler shadow' in the stellar line profile. These line profile variations are mapped as a function of stellar rotational velocity and orbital phase. The vertical lines mark the $v \sin i_\star$ of the star, while the horizontal lines mark the timings of ingress and egress. The planetary transit signal is the dark trail crossing from bottom left to top right. The top two panels show the transit as seen with the blue and red cameras. The middle panel shows the combined data set. The bottom two panels show the best-fit model and the residuals after model subtraction. The figure is taken from Zhou et al. (2019a) and reproduced with permission from George Zhou

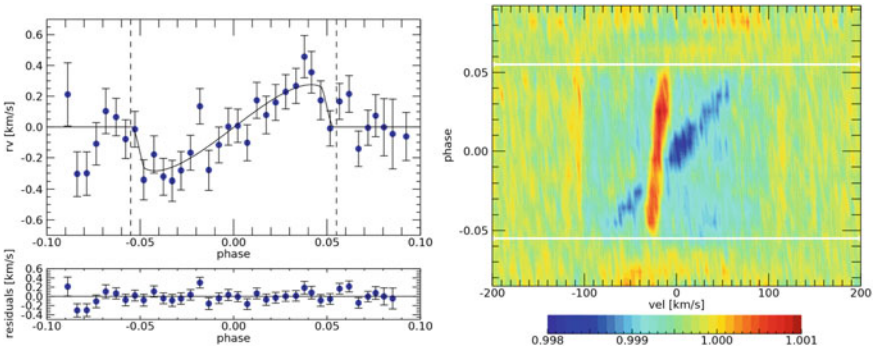

Fig. 3.55 Atmospheric RML effect of the ultra-hot-Jupiter KELT-9b. *Left*: the phase-folded radial-velocity data (points with error bars) were measured with the high-resolution spectrograph HARPS-N during four planetary-transit events of KELT-9b (the RVs of the four transits were averaged in bins of 0.005 in phase). *Right*: The Doppler tomographic map of the transit of KELT-9b as in Fig. 3.54. The line profile was averaged over four transit observations, with the horizontal white lines indicating the transit ingress and egress. Both the Doppler shadow of the planet (red) and the planetary atmospheric trace (blue) are clearly visible. The figure is taken from Borsa et al. (2019) and reproduced with permission © ESO

planetary Doppler shadow, see Fig. 3.55. By studying the shape of this deviation one can measure the extension of the planetary atmosphere that correlates with the stellar mask (Borsa et al. 2021; Rainer et al. 2021). The method is applicable only in the case of extremely hot planetary atmospheres, which show a chemical composition similar to that of late-type stars (in particular due to the presence of neutral or ionized iron).

Finally, if the star is a very fast rotator and the mass of the secondary is non-negligible (i.e. it is a brown dwarf or low-mass star), more accurate measurements of λ can be obtained by performing global modeling of the Doppler tomographic data, the RV measurements, the photometric transit light curves and the gravity-darkening effect (e.g., Zhou et al. 2019a, b).

3.6.3.3 Star-Spot Occultations

There is another fascinating technique that we can use to measure the spin-orbit angle of a planetary system, which is based on a simultaneous observation of a planetary transit and a *star-spot crossing* event. Instead of being spectroscopic, this technique is purely photometric and consists in measuring the brightness variations of an active, spotted star[14] during a transit of its planet. If there is a single star spot or a star-spot complex and the transiting planet occults it, then the transit depth will temporarily decrease as the star will appear brighter (star spots have lower effective temperature

[14] Just like the Sun can present sunspots, also the other stars that we observe in the Galaxy can have star spots on their photosphere.

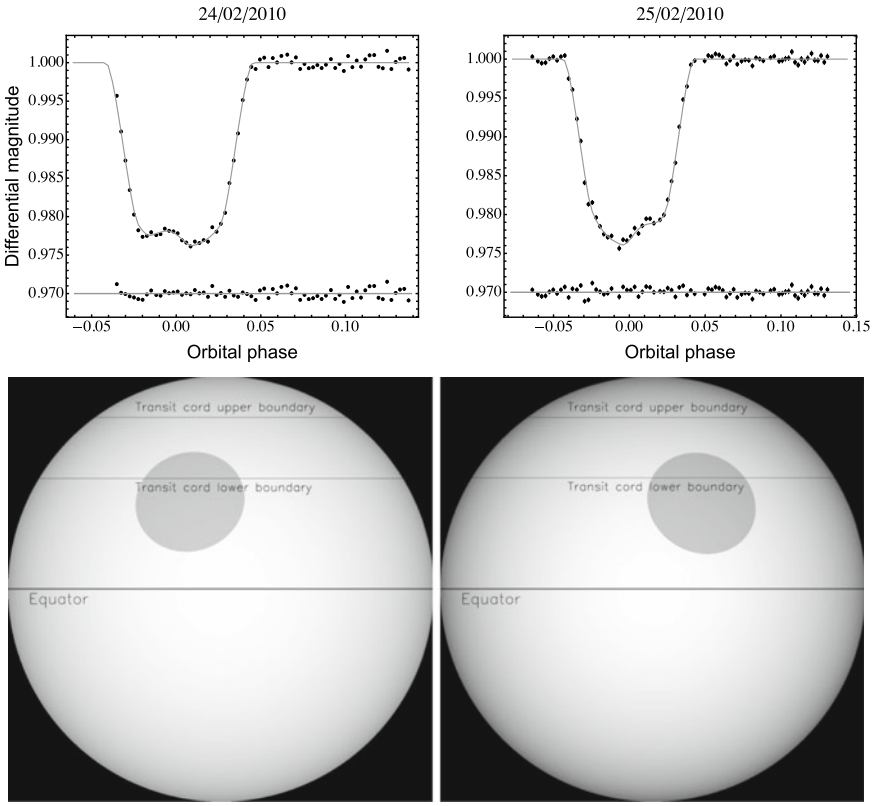

Fig. 3.56 *Top panels*: The light curves of two consecutive transits of the hot Jupiter WASP-19 b, which has an orbital period of ≈ 0.8 days, observed with the 3.6 m New Technology Telescope (Tregloan-Reed et al. 2013). *Bottom panels*: Representations of the WASP-19 stellar disc, star-spot positions, and transit chords for the two transit events with star-spot crossings. The gray-scale of each star-spot is related to its contrast. The two horizontal lines on each panel represent the upper and lower parts of the planet pass. The authors estimated $\lambda = 1.0 \pm 1.2$ deg. Data and bottom figures kindly provided by Jeremy Tregloan-Reed

than the surrounding photosphere). A small bump will then be recorded in the transit light curve, similar to those in Fig. 3.56. Now, if the planetary system is well aligned, if the star has a plausible rotation period of roughly a month and the planet has, instead, an orbital period of few days, the next time the planet transits in front of its star, we will see that the star spot has only moved slightly across the stellar surface, so that we will notice the same anomaly but occurring at a later transit phase. The phase shift of the anomalous feature will continue until the spots disappear from the visible hemisphere due to rotation. However, if the spin-orbit angle is significant, the planet will never encounter again the same star spot at the subsequent transit, we will no longer see the anomaly and we can put a lower limit on the stellar obliquity (e.g., Dai and Winn 2017).

In general, the occultation of the same star-spot complex in two or more transit events indicates that there is good spin-orbit alignment, allowing the measurement of λ with very good precision (e.g., Mancini et al. 2017). On the other hand, if in two consecutive transits we observed two different star spots, their latitude difference is completely degenerate with λ. Discriminating between the two cases is not trivial. Crucial parameters that one has to take into account are the rotational period of the host star, the flux modulation produced by the rotation of the starspots and the difference in position and time among the starspot-crossing events, which should be precisely modeled with sophisticated procedures (e.g., Désert et al. 2011; Sanchis-Ojeda et al. 2011; Sanchis-Ojeda and Winn 2011; Sanchis-Ojeda et al. 2013b; Tregloan-Reed et al. 2013; Mazeh et al. 2014; Tregloan-Reed et al. 2015; Juvan et al. 2018). The projected obliquity can also be efficiently determined by a statistical method, correlating the starspot anomalies observed in a sequence of transits (Dai et al. 2018b). In this case, a large number of consecutive transits are required, restricting this method only to long time-series photometric data collected with space missions, like *Kepler* and K2. With this method, (Dai et al. 2018b) determined the obliquities for 10 stars with hot Jupiters studying a sample of a bit more than 60 stars.

3.6.3.4 Other Methods

Another statistical approach for determining the spin-orbit alignment is the so-called $v \sin i_\star$*method*, which is based on searching anomalously low values of the projected rotation velocity, $v \sin i_\star$, in a large sample of stars hosting transiting planets. Since low obliquity for a transiting-planet system implies that $\sin i \approx \sin i_\star \approx 1$, a low value of $v \sin i_\star$ can be the sign of high-obliquity systems (Schlaufman 2010; Winn et al. 2017a).

Other methods for measuring the obliquity have not found many applications so far, because they require specific situations, like years of ultra-accurate photometry with ≈ 1 minute cadence for studying the stellar pulsation modes (the *asteroseismic method*; Gizon and Solanki 2003), or rapidly-rotating stars and high obliquity (the *gravity-darkening method*; Barnes 2009), or very bright and rapidly rotating stars (the *interferometric method*; Kraus et al. 2020).

3.6.4 Obliquity of Transiting Planetary Systems

Having determined λ, we can also estimate the real obliquity, ψ. For this purpose, we need to know the planetary orbital inclination, i, and the stellar-spin inclination angle, $i_\star$.[15] Then, by using the following formula (Winn et al. 2007)

[15] Frequency analysis of the time-series light curves and the study of the oscillation modes induced by stellar rotation (*Asteroseismology*) can be used for determining $i_\star$.

$$\cos\psi = \cos i_\star \cos i + \sin i_\star \sin i \cos\lambda\,, \tag{3.19}$$

we can get the true orbital obliquity of a given transiting planetary system. To-date (September 2020), λ has been measured for roughly 160 transiting exoplanets, while ψ has been constrained for only roughly 30 ones.[16] Except for the measurements of the RML effect of few brown dwarfs, Neptune-, superEarth-size planets and, recently, three rocky planets in the TRAPPIST-1 system (Hirano et al. 2020), the degree of spin-orbit alignment has been mostly determined for hot Jupiters, representing the only class for which we have a good statistical sample.

What this large collection of λ measurements for hot Jupiters is telling us is still a matter of debate, as reviewed by (Triaud 2018). No convincing patterns or trends have emerged from plotting the projected obliquity versus other parameters such as, for example, planetary mass and radius, orbital separation, or stellar age. Interestingly, however, early investigations based on smaller samples of λ measurements tentatively identified two populations of more or less aligned hot Jupiters based on the effective temperature $T_{\rm eff}$ of their parent stars, the dividing line being related to the Kraft break (Kraft 1967) and falling somewhere between 6090 and 6300 K (Winn et al. 2010; Albrecht et al. 2012; Dawson 2014). This is marked with a gray zone in Fig. 3.57, where the absolute values of λ of hot Jupiters ($0.1\,M_{\rm Jup} < M_{\rm p} < 13\,M_{\rm Jup}$) have been plotted versus $T_{\rm eff}$.

On the left side of this plot we find planets orbiting stars with mostly convective outer envelopes, whereas on the right side host stars have mostly radiative outer envelopes. Therefore, the two populations of planet hosts are distinctively different in terms of e.g., strength of the magnetic field, rotation rate and, especially, the tidal dissipation rate (a star's ability to convert tidal oscillations into heat). Mostly convective stars are cooler and supposed to have much more rapid tidal dissipation because the convective cells are producing the turbulent cascades that lead to energy/heat loss, whereas the radiative stars are thought to have much weaker tidal dissipation. Therefore, hot Jupiters hosted by relatively cool stars ($T_{\rm eff} < 6100$ K), should be much more aligned than those hosted by hotter stars because in the former case tides effectively damp any possible obliquity on timescales much shorter than those in connection to the planet's orbital decay (Lai 2012; Valsecchi and Rasio 2014). However, although high-obliquity hot Jupiters were found regularly above the Kraft break, many exceptions challenge this theory, as we can see from Fig. 3.57.

It was also noted that those planetary systems, in which the hot Jupiter is massive ($M_{\rm p} > 3M_{\rm Jup}$) tend to have lower spin-orbit angles, because the parent star is much more affected by planet's tidal forces (Hébrard et al. 2011). We plot in Fig. 3.58 the measured sky-projected obliquities of all known systems hosting $0.1\,M_{\rm Jup} < M_{\rm p} < 80\,M_{\rm Jup}$ companions, including brown dwarfs such as WASP-30 b, KELT-1 b and CoRoT-3 b, as a function of scaled orbital distance from the host star $a/R_\star < 12.5$. The larger circles in this plot, which are associated with companions with larger

[16] Data taken from TEPC at: `http://www.astro.keele.ac.uk/jkt/tepcat/rossiter.html` (Southworth 2011).

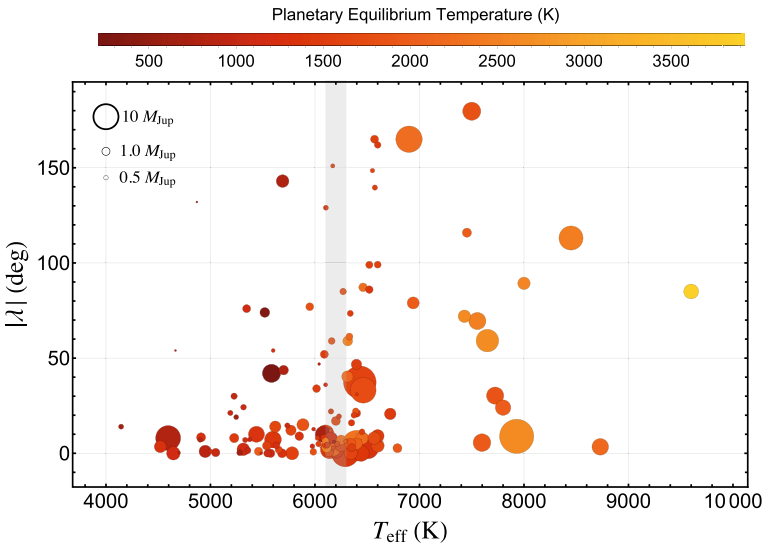

Fig. 3.57 Absolute values of the sky projected orbital obliquity angles of close-in giant planets as a function of the host star's effective temperature. The planets are represented by circles, whose size is proportional to their mass. The error bars have been suppressed for clarity. Color indicates their equilibrium temperature. The gray zone should discriminate two different populations of hot Jupiters, according to several authors (e.g., Winn et al. 2010; Albrecht et al. 2012). Data were taken from TEPCat in September 2020

masses, show that most of these systems present a good alignment (Zhou et al. 2019a).

Using the $v \sin i$ method (see Sect. 3.6.3.4), Winn et al. (2017a), Muñoz and Perets (2018) and Louden et al. (2021) selected samples of well-studied *Kepler* planet hosting stars with reliably measured photometric periods and projected rotation velocities. The aim was to investigate in a statistical sense the obliquities of *Kepler* stars that, as we know (cf. Sect 3.6.2), host planets spanning a wide range of sizes, most of which are smaller than Neptune. The above studies helped drawing a picture in which Kepler small-size planet hosts generally have higher values of projected rotational velocities, and therefore low obliquities, than control samples of field stars. The result is thus a broad indication of spin-orbit alignment for Kepler planetary systems, except for those orbiting hotter, late-F-type stars ($T_{\rm eff} \gtrsim 6250$ K), that exhibit compatible to random orientations and therefore typically high obliquities (see Fig. 3.59). The tentatively identified trend of increasing λ (or ψ) with $T_{\rm eff}$ for hot Jupiters thus appears to extend to other types of planets.

Important as the statistical inferences based on the $v \sin i$ method may be, it would be highly desirable to expand the domain of true obliquity measurements for other types of planets besides giant planets and brown dwarfs. Observations of the RML effect for Neptunes and Super Earths are especially challenging given that the amplitudes of the RV anomalies can be typically on the order of a few ms^{-1},

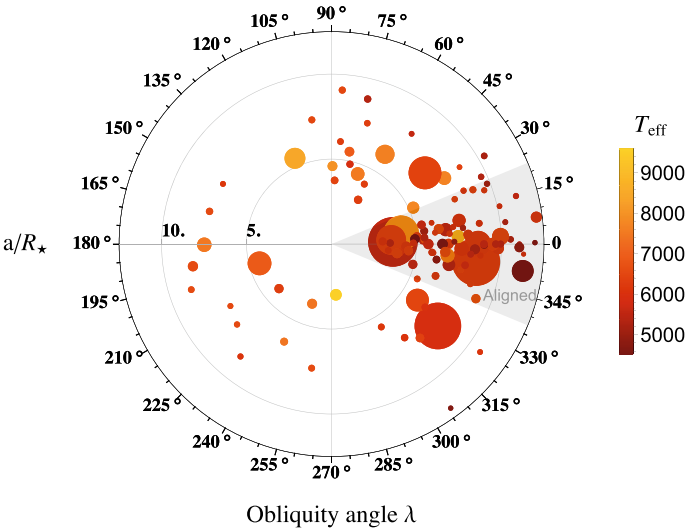

Fig. 3.58 Sky projected orbital obliquity of massive planets and brown dwarfs ($0.1\ M_{\rm Jup} < M_{\rm p} < 30\ M_{\rm Jup}$) as a function of their scaled orbital distance from the host star. The planets are represented by circles, whose size is proportional to their mass. The error bars have been suppressed for clarity. Color indicates the effective temperature of their parent stars. Data were taken from TEPCat in September 2020. Figure inspired by similar plots from J. Winn; see also Zhou et al. (2019a)

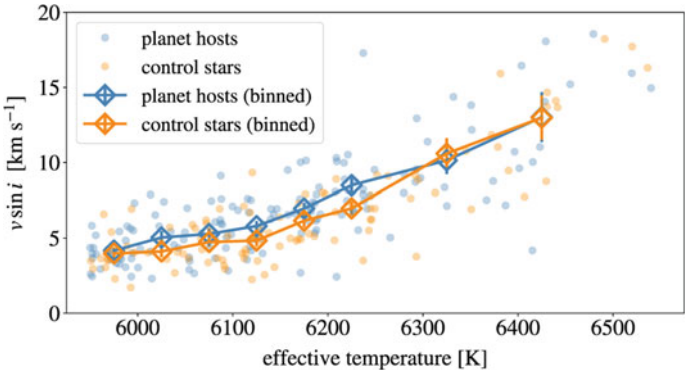

Fig. 3.59 Measured sky-projected rotation velocity versus effective temperatures for a sample of *Kepler* stars (blue points) with $T_{\rm eff}$ between 5950 and 6550 K. Orange points represent a control sample of stars with matching spectroscopic properties and random orientations. Figure taken from Louden et al. (2021) and reproduced with permission from Emma M. Louden

or smaller (see Eq. 3.18), unless the primary is a fast rotator. A particular focus has been devoted recently to obliquity measurements for transiting systems at young ages (e.g., DS Tuc Ab: Zhou et al. 2020; K2-25 b: Stefansson et al. 2020; AU Mic b: Addison et al. 2020; TOI-1726 c: Dai et al. 2020), as in this case dynamical masses are very difficult to determine due to the very high levels of activity and fast rotation of the primaries, therefore detection of the RML effect also corresponds to a direct planet confirmation. So far, these systems all appear well aligned, but the regime of small-number statistics still prevents any clear conclusions to be drawn.

The emerging picture is that in the case of giant planets the wide range of measured obliquity values implies that dynamical processes such as planet-planet scattering and secular perturbations are responsible for tilting their orbits. The situation for smaller planets is less clear, as obliquities might be excited or damped based on a number of possible mechanisms, either environmental in nature (originally misaligned protoplanetary disks, dynamical interactions with outer giant planets or stellar companions; e.g. Bate et al. 2010; Spalding and Batygin 2015; Anderson and Lai 2018; Takaishi et al. 2020), or star-specific (stochasticity of internal gravity waves in hotter stars; e.g. Rogers et al. 2012).

3.7 Ultra-Short Period Planets

3.7.1 Introduction

One of the most intriguing findings in the field of exoplanetary science was the discovery of small planets with ultra-short orbital periods, which are operationally defined as having $P \lesssim 1$ day. A key step forward from space-based surveys came in 2009 during the *CoRoT* mission, when Corot-7b was announced, a small ($\sim 1.5 - 1.6\, R_\oplus$) transiting planet with a very short period of 0.85 days (Léger et al. 2009). Two years later, the two super-Earth planets Kepler-10b and 55 Cnc e were found with periods smaller than 0.8 days (Batalha et al. 2011; Winn et al. 2011). Later on, many other surveys, both in space and from the ground, continued finding new very short-period planets. For instance, by early 2021, 98 giant planets ($R > 8 R_\oplus$) had been discovered with periods between 2 and 3 days, 65 with periods between 1 and 2, and 8 with periods shorter than one day (namely, NGTS-10b, WASP-19b, WASP-43b, HATS-18b, NGTS-6b, WASP-103b, KELT-16b, HIP 65 A b; see exoplanetarchive.ipac.caltech.edu). The *Kepler* spacecraft has unveiled the presence of over 100 ultra-short period (USP) small planets with $R_\mathrm{p} \lesssim 2\, R_\oplus$. It is clear that, at least for solar-type stars, super Earths with periods shorter than one day occur as frequently as hot Jupiters with periods of $\sim$ 1-10 days and that their discovery was previously hampered mainly because of their small signals.

The study of short-period planets is important for many reasons. They are so close to their host stars that the geometric probability for transits can be as large as 40%. Moreover, the expected surface temperatures of USP planets can reach 2000 –

3000 K, allowing the detection of thermal emission from the planetary surface (e.g., Sanchis-Ojeda et al. 2013a), and the induced RV signals can be as high as a few m/s, allowing the planet masses to be measured even for moderately faint stars (Howard et al. 2013; Pepe et al. 2013). Therefore, this class of objects is important to understand the formation and evolution of short-period planets in general, but also to study star-planet interactions, atmospheric erosion, photoevaporation, and other processes arising from strong irradiation and tidal forces (Winn et al. 2018, and references therein).

3.7.2 The Case of Kepler-78b and the USP Planets

One object that emerged from the 4-year *Kepler* survey of about 200,000 stars was the Earth-sized planet Kepler-78b (Sanchis-Ojeda et al. 2013a). This planet, with an orbital period of 8.5 hours, is important because is one of the very smallest planets for which both mass and radius have been measured to better than 20% precision (Howard et al. 2013; Pepe et al. 2013). Based on spectroscopic monitoring performed with HIRES@Keck, Howard et al. (2013) reported a radius of $1.20 \pm 0.09\ R_{\oplus}$ and a mass of $1.69 \pm 0.41\ M_{\oplus}$, implying a planet's mean density of 5.3 ± 1.8 g/cm^3. Similar findings were also found by Pepe et al. (2013) from independent measurements using the HARPS-N@TNG spectrograph. All these results are similar to the Earth values, suggesting for Kepler-78b a rock/iron composition and negligible atmosphere (see Fig. 3.60).

Howard et al. (2013) explored some possibilities for the interior structure of Kepler-78b using a simplified two-component model (Fortney et al. 2007) consisting of an iron core surrounded by a silicate mantle, which is a model reproducing correctly the masses of Earth and Venus. Applied to Kepler-78b, the model gives an iron fraction of $\sim 20\%$, similar to that of the Earth and Venus and smaller than that of Mercury. Moreover, with a star-planet separation of 0.01 au, the dayside of Kepler-78b is heated to temperatures of 2300-3100 K, therefore any gaseous atmosphere around the planet would probably have been lost due to photoevaporation by intense starlight. Kepler-78b represents a 'prototype' for the class of USP planets (the interested reader can find additional details in the recent review by Winn et al. (2018) on Kepler-78 and the ultra-short period planets in general.)

3.7.3 The 1-Day Cutoff and Planet Occurrence

The boundary at one day for the orbital periods of USP planets is an arbitrary choice, mainly due to the fact that such $P_{\rm orb} < 1$ day regime was previously unexplored. Therefore, there is no sharp astrophysical distinction between the USP planets with periods less than one day and the short-period planets with periods of 1–10 days. Following the reasoning of Winn et al. (2018), it is possible to verify that the angular

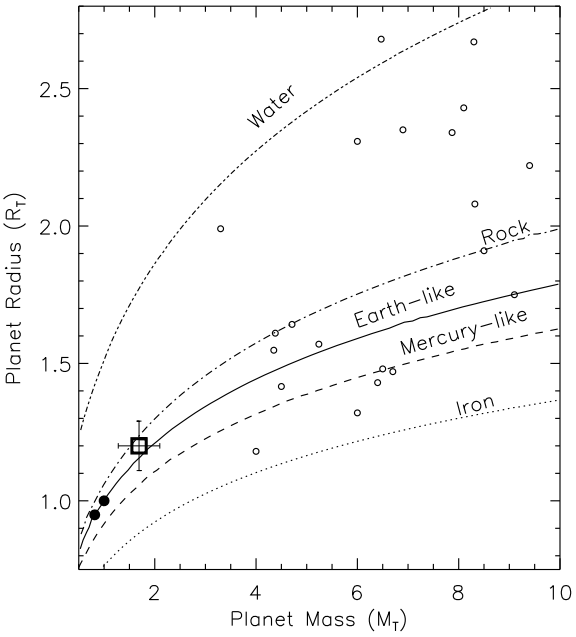

Fig. 3.60 The planet Kepler-78b (open square) placed on a planetary-mass diagram. Earth and Venus are represented by filled circles, while the other extrasolar planets with well characterized mass and radius are plotted as open circles. Model mass-radius relationships for idealized planets consisting of 100% iron, rock (Mg_2SiO_4), and pure water are shown as dotted, dot-dashed, and dot-dot-dot dashed lines, respectively (Seager et al. 2007; Fortney et al. 2007). Solid and dashed lines denote Earth-like composition (67% rock, 33% iron) and Mercury-like composition (40% rock, 60% iron). Exoplanet masses and radii (without restrictions on uncertainties) were taken from the Exoplanet Orbit Database (Wright et al. 2011; September 2020). Data for Kepler-78 were taken from (Howard et al. 2013). Figure inspired by a similar plot by Howard et al. (2013)

diameter of a main-sequence star in the sky of the USP planet is around fifty times wider than the Sun in the sky of the Earth. This means that tidal interactions lead to relatively rapid orbital and spin evolution. Therefore, when there is a USP planet around a main-sequence star it is reasonable to assume that the planet has a circular orbit and is tidally locked (with a permanent dayside and nightside). However, the orbit of an Earth-like USP planet does not have enough angular momentum to spin up the star and achieve a stable double-synchronous state, leading to its spiraling towards the star (see, e.g., Patra et al. 2017). Moreover, a one-day planet around a solar-like star intercepts around 2500 times the flux of the Sun impinging on the Earth and should be bathed in strong UV and X-ray radiation. If all incident energy is re-radiated locally, the planet's surface can easily reach temperatures as high as $\gtrsim$ 3000 K (as in fact determined for Kepler-78b). This would lead to a complete loss of any hydrogen-helium atmospheric envelope (Owen and Wu 2016) and the melting of silicates and iron, resulting in the so-called "lava worlds" or "hot Earths" (Léger et al. 2011; Rouan et al. 2011).

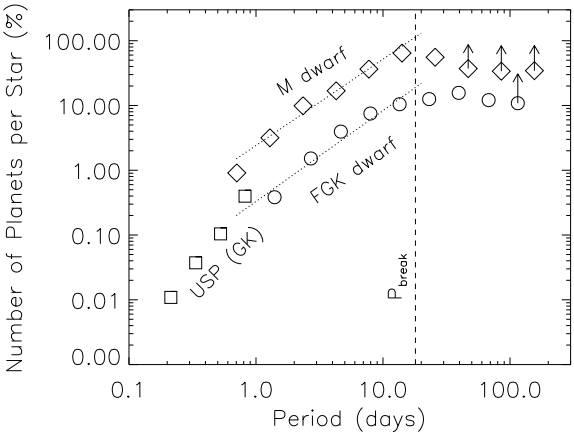

Fig. 3.61 Occurrence rates of sub-Neptunes orbiting FGKM dwarfs (Fressin et al. 2013; Dressing and Charbonneau 2015). The $P_{\rm break}$ at ∼10 days is shown as vertical dashed line. Short-period planets at $P < P_{\rm break}$ appear distributed according to a $P^{1.4-1.5}$ power law (dotted lines). USP planets at $P < 1$ days using data from Sanchis-Ojeda et al. (2014) are shown as open squares. Points without arrows correspond to sub-Neptunes larger than 0.5 $R_\oplus$ for M-dwarf hosts, and larger than 0.8 $R_\oplus$ for FGK stars. Points with arrows represent sub-Neptunes larger than 1 $R_\oplus$ (M dwarfs) and larger than 1.25 $R_\oplus$ (FGK dwarfs). Figure adapted from Lee and Chiang (2017)

From *Kepler* data, Sanchis-Ojeda et al. (2014) found that the occurrence rate of USP planets shows a strong dependence on the host star's mass. They measured an occurrence rate in the range ∼ 1.10% and ∼ 0.83% for M and K dwarfs, respectively, and ∼ 0.51% and ∼ 0.15% for G and F dwarfs, respectively. This represents the evidence that cooler stars are more likely to host USP planets. Occurrence rates of sub-Neptunes ($R < R_\oplus$) orbiting FGKM dwarfs as obtained by the *Kepler* mission in combination with RV surveys are shown in Fig. 3.61 (Fressin et al. 2013; Dressing and Charbonneau 2015), where USP planets around GK stars are marked with open squares (Sanchis-Ojeda et al. 2014). At periods $P > 100$ days sub-Neptunes appear to be evenly distributed, while at shorter periods they are less common. The occurrence rate as a function of orbital period follows a broken power law, with a break at $P_{\rm break} \sim 10$ days (e.g., Youdin 2011; Mulders et al. 2015a). Within ∼ 10 days, the occurrence rate scales approximately as $P^{1.4-1.5}$ depending on the spectral type, while beyond ∼ 10 days the occurrence rate shows a plateau. The lower occurrence rate of planets at $P < P_{\rm break}$ may reflect a truncation of their disks, perhaps due to the magnetosphere of their host stars (e.g., Mulders et al. 2015a). In fact, disk-locking theory posits that the inner disk edge corotates with the host star in equilibrium (e.g., Camenzind 1990; Königl 1991; Romanova and Owocki 2016). The disk-locking scenario is supported observationally by "dippers" in the light curves of young low-mass stars with relatively evolved disks (see, e.g., Ansdell et al. 2020; Frasca et al. 2020, and references therein). These stars exhibit material lifted out of the disk midplane, near the corotation radius (see, e.g., Stauffer et al. 2015; Ansdell et al. 2016). The distribution of rotation periods of low-mass stars younger than ∼ 5 Myr typically ranges

from 0.2 to 20 days with peaks around $\sim$ 10 days and falls towards shorter periods. This result has been interpreted as a possible connection between disk truncation at corotation and occurrence rate of short-period planets (Lee and Chiang 2017).

3.7.4 Host Star Iron Abundance and Planet Formation

The connection between stellar iron abundance and the presence of planets offers an observational link between conditions during the epoch of planet formation and mature planetary systems. This is because the star iron abundance (usually expressed as [Fe/H], the iron to hydrogen abundance ratio measured with respect to that of the Sun) is thought to reflect the metallicity of the protostellar nebula and the protoplanetary disk from which planets form. Since metal-rich protoplanetary disks are thought to have enhanced surface densities of solids, one expects that metal-rich disks form cores of gas giant planets and terrestrial planets with higher efficiency than metal-poor disks (core-accretion theory; Lissauer et al. 1995; Pollack et al. 1996). As we have already noticed in Sect. 3.3.1, the increase in giant planet occurrence with iron abundance is well established, while in the regime of lower planetary masses this trend appears less solid.

Figure 3.62 shows the distribution of [Fe/H] for stars in three samples of *Kepler* stars analyzed through Keck spectroscopy (Winn et al. 2017b):

1. USP planets selected from Sanchis-Ojeda et al. (2014);
2. hot Jupiters with radii in the range $4 - 20\,R_\oplus$ and orbital periods shorter than 10 days;
3. hot small planets with radii $< 4\,R_\oplus$ and orbital periods between 1 and 10 days.

Even at a glance, it is clear that the hot Jupiters appear to be weighted toward higher [Fe/H] than either the USP planets or the hot small planets. The distributions for the USP and the small planets appear similar to one another. From a two-sample Kolmogorov-Smirnov test, Winn et al. (2017b) concluded that it is very unlikely that the USP planets and hot Jupiters are drawn from the same distribution, while the USP planets and the hot smaller planets have distributions that are indistinguishable. The association between high metallicity and occurrence of USP planets is of particular interest because it was postulated that USP planets may be the remnants of disrupted hot Jupiters (Jackson et al. 2013; Valsecchi et al. 2015). Since this correlation was not found, it is unlikely that USP planets are the evaporated cores of hot Jupiters that reached so close to their host stars that they completely lost their gas through photoevaporation, or Roche lobe overflow, or other processes. It remains quite possible that they are solid cores of formerly gaseous planets smaller than Neptunes.

Recently, Petigura et al. (2018), based on California-*Kepler* Survey results, modeled the metallicity (M) distribution of planets as $df \propto 10^{\beta M} dM$, where β is related to the strength of any metallicity correlation. The authors found that the correlation gets steeper with decreasing orbital period and increasing planet size, from $\beta = -0.3 \pm 0.2$ for warm super-Earths to $\beta = 3.4 \pm 0.9$ for hot Jupiters. This result

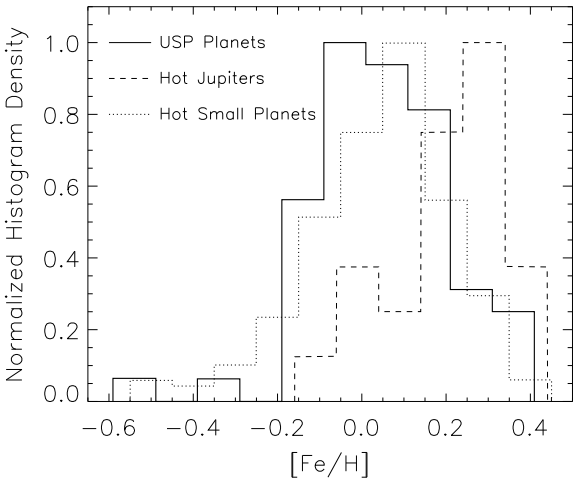

Fig. 3.62 Metallicity distribution of three statistical samples: UPS planets (solid line; $[Fe/H]_{mean} \sim 0.06$ dex), hot Jupiters (dashed line; $[Fe/H]_{mean} \sim 0.21$ dex), and hot small planets (dotted line; $[Fe/H]_{mean} \sim 0.05$ dex). Figure adapted from Winn et al. (2017b)

supports the idea that high metallicities in protoplanetary disks increase the mass of the largest rocky cores or the speed at which they are assembled, enhancing the production of planets with higher masses. They conclude that the association between high metallicity and short-period planets may reflect disk density profiles that facilitate the inward migration of solids or higher rates of planet-planet scattering.

3.7.5 Composition of Hot Earths

High-cadence RV monitoring of USP planets allows to fully sample their orbits in just a few nights of observation. Furthermore, since the RV semi-amplitude scales with $P^{-1/3}$, the shorter the orbital period, the higher the amplitude of the RV signal, increasing the likelihood of swift detection. However, because the planets tend to be small, the Doppler signals typically have K_p not exceeding a few m/s, making their detection challenging nonetheless. Accurate masses have been measured for a few USP planets, as shown in Fig. 3.63, where the data points are color-coded according to the level of insolation by the host star. Indeed, one might have expected the more strongly irradiated planets to have a higher density, as a consequence of photoevaporation. However, no clear correlation between planetary mean density and level of irradiation appears. This could be due to the fact that all USP planets are so strongly irradiated that they have been entirely stripped of any preexisting hydrogen/helium atmospheres, as all of them show irradiation values much higher than the threshold of $650\,F_\oplus$ above which close-in sub-Neptunes have undergone photoevaporation (Lundkvist et al. 2016). In the mass-radius diagram for USP planets with well-characterized parameters, radii smaller than $2.2\,R_\oplus$ and orbital periods smaller than 1 day, most planets are placed between the theoretical relations for pure

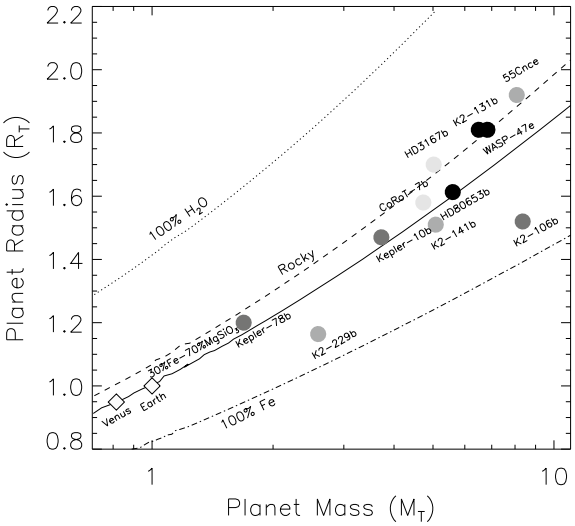

Fig. 3.63 Masses and radii of USP planets for which very accurate Doppler mass measurements have been reported (filled circles). The circles are color-coded according to four levels of irradiation by the star in units of $F_\oplus$, the insolation level received by Earth: light grey ($< 2000\ F_\oplus$), dark gray ($2000 - 3000\ F_\oplus$), very dark gray ($3000 - 4000\ F_\oplus$), black ($> 4000\ F_\oplus$). The diamonds represent Venus and Earth. The curves are theoretical mass-radius relationships for planets of different compositions: pure iron, iron core and silicate mantle, pure rock, and pure water (Zeng et al. 2016). References for planetary masses and radii are: Howard et al. (2013); Haywood et al. (2014); Weiss et al. (2016); Demory et al. (2016); Dai et al. (2017); Gunther et al. (2017); Christiansen et al. (2017); Vanderburg et al. (2017); Malavolta et al. (2018); Santerne et al. (2018); Frustagli et al. (2020). Figure inspired by a similar plot by (Dai et al. 2017)

rock (100% $MgSiO_3$) and Earth-like (30% Fe and 70% $MgSiO_3$) compositions (see Fig. 3.63). K2-229b has high density suggesting a massive iron core compatible with that of Mercury, although it was expected to be similar to that of Earth based on host-star chemistry (Santerne et al. 2018).

Dressing et al. (2015) claimed that planets heavier than $6\ M_\oplus$ should have gaseous H/He envelopes, while Rogers (2015) found that planets with orbital periods shorter than 50 days and radii smaller than $1.6\ R_\oplus$ are predominantly rocky. Later, Lopez (2017) found that planets on USP orbits could often retain their envelopes even at high irradiation levels if they formed with very high-metallicity water dominated envelopes. This would imply that planets larger than $1.6\ R_\oplus$ to be more massive than $6\ M_\oplus$ and with densities compatible with water envelopes. Of the eleven USP planets for which mass and radius have been both measured with high accuracy, six are larger than $\sim$ 1.5-1.6 $R_\oplus$ (HD3167b, K2-131b, WASP-47e, 55 Cnc e, HD 80653b, and CoRoT-7b). Three of them (namely, K2-131b, WASP-47e, 55 Cnc e) have masses heavier than $6\ M_\oplus$ and a low mean density ($\sim$ 6.0–6.4 g/cm^3) compatible with a layer of volatiles (like water) surrounding a rocky-iron body. For K2-106b, Sinukoff et al. (2017) reported a planetary mass and radius of $9.0\ M_\oplus$ and $1.82\ R_\oplus$, compatible

with a rocky composition and a water mass fraction of $\sim 2\%$, while the values by Gunther et al. (2017) shown in Fig. 3.63 pointed to an iron-rich composition and a water mass fraction $< 20\%$ (Dai et al. 2017). For HD 3167b, Christiansen et al. (2017) reported a planetary mass and radius of 5.02 $M_\oplus$ and 1.70 $R_\oplus$ (consistent with a rocky composition and a water mass fraction $\sim 15\%$, as shown in Fig. 3.63), while Gandolfi et al. (2017) reported 5.69 $M_\oplus$ and 1.575 $R_\oplus$, suggesting a predominantly rocky composition (with a water mass fraction $< 10\%$). The position of HD 80653b and its density is consistent with an Earth-like composition of rock and iron with no significant envelope of volatiles or H/He surrounding the planet (Frustagli et al. 2020).

3.7.6 Formation and Early Evolution of USP Planets

The formation and early evolution of USP planets and their relationship to wider-orbit planets are not fully understood. Dai et al. (2018b) considered a sample of *Kepler* and *K2* multiple-planet systems with the innermost planet of radius smaller than 4 $R_\oplus$ (to avoid giant planets) and $a/R_\star < 12$ (to consider inclinations of 85–90°). They measured the minimum difference $\Delta I = |I_1 - I_2|$ between the fitted orbital inclinations of the innermost two planets as a function of the orbital distance of the innermost planet (see Fig. 3.64). ΔI is equal to the mutual inclinations only if the trajectories of the two planets across the stellar disk are parallel and on the same hemisphere of the star. Among the systems with the closest-orbiting planets ($a/R_\star < 5$), there are about 10 systems for which $\Delta I = 5° - 10°$, larger than the typical mutual inclinations inferred for planets in wider orbits. The planets with $a/R_\star > 5$ almost all have $\Delta I < 5°$. This means that the planets with smaller values of $a/R_\star$ have a broader distribution of ΔI, nearly filling the full range of inclinations compatible with transits. Similar results were obtained by, e.g., Tremaine and Dong (2012) and Fabrycky et al. (2014). Dai et al. (2018b) also noted that higher values of ΔI are associated with larger period ratios. They found that period ratios tend to be higher when the inner planet's period is shorter than about one day (Steffen and Farr 2013). This means that the innermost planets have experienced both inclination excitation and orbital shrinkage, and therefore that they are dynamically more separated.

The results by Dai et al. (2018b) can be interpreted as follows: the shortest-period planets tend to have larger mutual inclinations, and thus are likely to be observed to transit even when the wider-orbiting companions do not transit. These results indicate that the shortest-period planets have a different orbital architecture, with higher mutual inclinations and larger period ratios, meaning that whatever processes led to the extremely tight orbits of these planets were also responsible for tilting the orbit to a higher inclination.

Several theories have been proposed for the formation of very short-period sub-Neptune planets:

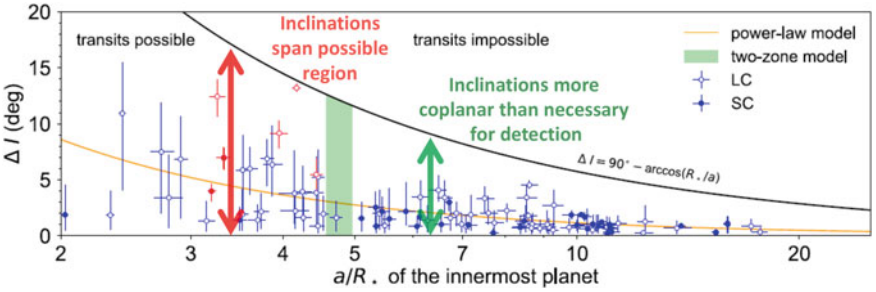

Fig. 3.64 Inclination difference ΔI versus $a/R_\star$ of the innermost planet of a sample of *Kepler/K2* multiple-planet systems. The orange solid line represents a power law model by Dai et al. (2018b), while the black solid line is the boundary above which the inner planet would not transit. Figure adapted from Dai et al. (2018b)

- Spalding and Batygin (2016) proposed that if the host star was initially rotating rapidly, with a non-zero obliquity, the planets' orbits would undergo nodal precession at different rates becoming misaligned, with the innermost planet being most strongly affected.
- Lee and Chiang (2017) proposed that planets form from material collected near the innermost edge of the protoplanetary disk, begin with nearly circular well-aligned orbits, and then the innermost planet undergoes tidal orbital decay.
- In the "secular dynamic chaos" scenario, the innermost planet of a multi-planet system is launched into a high-eccentricity orbit via chaotic secular interactions with its companion planet. If the period is short and the eccentricity becomes high enough, tidal interactions with the host star shrink the orbit. Since eccentricity and inclination are excited together, this theory predicts that the shortest-period planets should have larger mutual inclinations (Petrovich et al. 2019).
- In the "forced-eccentricity migration" scenario, in which the interaction with outer companions continually excites the eccentricity of the innermost planet, eccentricity tides dissipate energy and shrink the orbit (Hansen and Murray 2015).

3.7.7 Brief Summary on USP Planets

Even though the origin of USP planets still remains a matter of debate, we can summarize their main properties as follows:

- USP planets tend to be in multi-planet systems (with longer-period companions), and very few of them have known transiting companions;
- the metallicity distribution of USP-planet-hosting stars does not resemble that of hot-Jupiter hosts and it is indistinguishable from that of close-in sub-Neptunes hosts;

- only very few USP planets have densities compatible with the presence of substantial water envelopes;
- the shortest-period planets likely migrated inwards via a dynamical process that excited orbital eccentricity and mutual inclinations simultaneously.

In conclusion, USP planets seem to represent a subset of sub-Neptunes, most of which have lost their atmospheres because of photoevaporation, or Roche lobe overflow, or other processes, with the exception of a few larger planets that have retained a water (or other volatiles) envelope.

References

Adams, E.R., Seager, S., Elkins-Tanton, L.: Astrophy. J. **673**, 1160 (2008)
Addison, B. C., Horner, J., Wittenmyer, R. A., et al.: (2020). arXiv:2006.13675
Albrecht, S., Winn, J.N., Johnson, J.A., et al.: Astrophys. J. **757**, 18 (2012)
Alonso, R., Brown, T.M., Torres, G., et al.: Astrophys. J. Lett. **613**, L153 (2004)
Alsubai, K.A., Parley, N.R., Bramich, D.M., et al.: Acta Astron. **63**, 465 (2013)
Anderson, K.R., Lai, D.: Mon. Noti. R. Astrono. Soc. **480**, 1402 (2018)
Anderson, S.G., Dittmann, J.A., Ballard, S., et al.: Astron. J. **161**, 203 (2021)
Ansdell, M., Gaidos, E., Hedges, C., et al.: Mon. Not. R. Astron. Soc. **492**, 572 (2020)
Ansdell, M., Gaidos, E., Williams, J.P., et al.: Mon. Not. R. Astron. Soc. **462**, L101 (2016)
Auvergne, M., et al.: Astron. Astrophys. **506**, 411 (2009)
Bach-Møller, N., Jørgensen, U.G.: Mont. Not. R. Astron. Soc. **500**, 1313 (2021)
Bakos, G.Á., Noyes, R.W., Kovács, G., et al.: Proc. Astron. Soc. Pac. **116**, 266 (2004)
Bakos, G.Á., Csubry, Z., Penev, K., et al.: Proc. Astrono. Soc. Pac. **125**, 154 (2013)
Ballard, S., Johnson, J.A.: Astrophy. J. **816**, 66 (2016)
Barnes, J.W.: Astrophys. J. **705**, 683 (2009)
Baruteau, C., Papaloizou, J.C.B.: Astrophy. J. **778**, 7 (2013)
Bashi, D., Helled, R., Zucker, S., Mordasini, C.: Astron. Astrophys. **604**, A83 (2017)
Bashi, D., Zucker, S., Adibekyan, V.: Astron. Astrophys. **643**, A106 (2020)
Batalha, N.M., et al.: Astrophy. J. **729**, 27 (2011)
Batalha, N.M.: Proc. Natal Acad. Sci. **111**, 12647 (2014)
Batalha, N.M., Lewis, T., Fortney, J.J., et al.: Astrophy. J. **885**, L25 (2019)
Bate, M.R., Lodato, G., Pringle, J.E.: Mon. Not. R. Astron. Soc. **401**, 1505 (2010)
Bean, J.L., Seifahrt, A.: Astron. Astrophys. **496**, 249 (2009)
Bean, J.L., Raymond, S.N., Owen, J.E.: J. Geophys. Res. **126**, 06639 (2021)
Becker, J.C., Adams, F.C.: Mon. Not. R. Astron. Soc. **455**, 2980 (2016)
Becker, J.C., Adams, F.C.: Mon. Not. R. Astron. Soc. **468**, 549 (2017)
Becker, J., Batygin, K., Fabrycky, D., et al.: Astron. J. **160**, 254 (2020)
Benneke, B., Wong, I., Piaulet, C., et al.: Astrophy. J. **887**, L14 (2019)
Berger, T.A., Huber, D., Gaidos, E., et al.: Astrono. J. **160**, 108 (2020)
Bitsch, B., Raymond, S.N., Izidoro, A.: Astron. Astrophys. **624**, A109 (2019)
Bonfils, X., Delfosse, X., Udry, S., et al.: Astron. Astrophys. **549**, A109 (2013)
Bonfils, X., Almenara, J.M., Jocou, L., et al.: Proc. SPIE **9605**, 96051L (2015)
Borsa, F., Rainer, M., Bonomo, A.S., et al.: Astron. Astrophys. **631**, A34 (2019)
Borsa, F., Allart, R., Casasayas-Barris, N., et al.: Astron. Astrophys. **645**, A24 (2021)
Borucki, W.J.: Rep. Prog. Phys. **79**, 036901 (2016)
Borucki, W.J., Summers, A.L.: Icarus **58**, 121 (1984)
Borucki, W.J., Koch, D., Basri, G., et al.: Science **327**, 977 (2010)

Borucki, W.J., Koch, D., Basri, G., et al.: Astrophy. J. **736**, 19 (2011)
Bouchy, F., Pepe, F., Queloz, D.: Astron. Astrophys. **374**, 733 (2001)
Bovaird, T., Lineweaver, C.H.: Mon. Not. R. Astron. Soc. **468**, 1493 (2017)
Brewer, J.M., Wang, S., Fischer, D.A., Foreman-Mackey, D.: Astrophy. J. **867**, L3 (2018)
Broeg, C., et al.: EPJ Web of Conf. **47**, 03005 (2013)
Brown, D.J.A., Collier Cameron, A., Díaz, R.F., et al.: Astrophy. J. **760**, 139 (2012)
Brügger, N., Burn, R., Coleman, G.-A.L., et al.: Astron. Astrophys. **640**, A21 (2020)
Bryan, M.L., Knutson, H.A., Howard, A.W., et al.: Astrophy. J. **821**, 89 (2016)
Bryson, S., Coughlin, J., Batalha, N.M., et al.: Astrono. J. **159**, 279 (2020a)
Bryson, S., Coughlin, J., Kunimoto, M., Mullally, S.E.: Astron. J. **160**, 200 (2020b)
Bryson, S., Kunimoto, M., Kopparapu, R.K., et al.: Astrophy. J. **161**, 32 (2021)
Buchhave, L.A., Latham, D.W., Johansen, A., et al.: Nature **486**, 375 (2012)
Buchhave, L.A., Bizzarro, M., Latham, D.W., et al.: Nature **509**, 593 (2014)
Buchhave, L.A., Latham, D.W.: Astrophy. J. **808**, 187 (2015)
Buchhave, L.A., Dressing, C.D., Dumusque, X., et al.: Astron. J. **152**, 160 (2016)
Buchhave, L.A., Bitsch, B., Johansen, A., et al.: Astrophy. J. **856**, 37 (2018)
Burke, C.J., Bryson, S.T., Mullally, F., et al.: Astrophy. J. Suppl. Ser. **210**, 19 (2014)
Burke, C.J., Christiansen, J.L., Mullally, F., et al.: Astrophy. J. **809**, 8 (2015)
Butler, R.P., et al.: Astrophy. J. **526**, 916 (1999)
Butler, R.P., et al.: Astrophy. J. **617**, 580 (2004)
Camenzind, M.: Rev. Modern Astron. **3**, 234 (1990)
Carrera, D., Raymond, S.N., Davies, M.B.: Astron. Astrophys. **629**, L7 (2019)
Carter, J.A., Winn, J.N.: Astrophy. J. **709**, 1219 (2010)
Catanzarite, J., Shao, M.: Astrophy. J. **738**, 151 (2011)
Cegla, H.M., Lovis, C., Bourrier, V., et al.: Astron. Astrophys. **588**, A127 (2016)
Charbonneau, D.: Research on extrasolar planets. ASP Conf. Ser. **294**, 449 (2003)
Charbonneau, D., et al.: Astrophy. J. **529**, L45 (2000)
Charbonneau, D., et al.: Nature **462**, 891 (2009)
Chatterjee, S., Ford, E.B.: Astrophy. J. **803**, 33 (2015)
Chatterjee, S., Ford, E.B., Matsumura, S., Rasio, F.A.: Astrophy. J. **686**, 580 (2008)
Chen, H., Rogers, L.A.: Astrophy. J. **831**, 180 (2016)
Chen, J., Kipping, D.: Astrophy. J. **834**, 17 (2017)
Choksi, N., Chiang, E.: Mon. Not. R. Astron. Soc. **495**, 4192 (2020)
Christiansen, J.L., Vanderburg, A., Burt, J., et al.: Astrophy. J. **154**, 17 (2017)
Ciardi, D.R., Fabrycky, D.C., Ford, E.B.: Astrophy. J. **763**, 41 (2013)
Cloutier, R., Menou, K.: Astron. J. **159**, 211 (2020)
Collier Cameron, A., Bruce, V.A., Miller, G.R.M., et al.: Mon. Not. R. Astron. Soc. **403**, 151 (2010a)
Collier Cameron, A., Guenther, E., Smalley, B., et al.: Mon. Not. R. Astron. Soc. **407**, 507 (2010b)
Collier Cameron, A.: Methods of Detecting Exoplanets, Springer, Berlin, p. 89 (2016)
Coughlin, J., Thompson, S.E. and Kepler Team: Astron. J. 152, 158 (2017)
Courcol, B., Bouchy, F., Deleuil, M.: Mon. Not. R. Astron. Soc. **461**, 1841 (2016)
Crossfield, I.J.M., Kreidberg, L.: Astron. J. **154**, 261 (2017)
Cumming, A., Butler, R.P., Marcy, G.W., et al.: Proc. Astron. Soc. Pac. **120**, 531 (2008)
Dai, F., Winn, J.N.: Astron. J. **153**, 205 (2017a)
Dai, F., Winn, J.N., Gandolfi, D., et al.: Astron. J. **154**, 226 (2017b)
Dai, F., Masuda, K., Winn, J.N.: Astrophy. J. Lett. **864**, L38 (2018a)
Dai, F., Winn, J.N., Berta-Thompson, Z., et al.: Astron. J. **155**, 177 (2018b)
Dai, F., Masuda, K., Winn, J.N., Zeng, L.: Astrophy. J. **883**, 79 (2019)
Dai, F., Roy, A., Fulton, B., et al.: (2020). arXiv:2008.12397
Damasso, M., Sozzetti, A., Lovis, C., et al.: Astron. Astrophys. **642**, A31 (2020)
Davies, M.B., Adams, F.C., Armitage, P., et al.: Protostars and Planets VI, 787 (2014)
Dawson, R.I., Murray-Clay, R.A.: Astrophy. J. **767**, L24 (2013)
Dawson, R.I.: Astrophy. J. **790**, 31 (2014)

Delisle, J.-B., Laskar, J.: Astron. Astrophys. **570**, L7 (2014)
Delisle, J.-B., Ségransan, D., Dumusque, X., et al.: Astron. Astrophys. **614**, 133 (2018)
Delrez, L., Gillon, M., Queloz, D., et al.: ıProc. SPIE **10700**, 107001I (2018)
Deming, D., et al.: Nature **434**, 740 (2005)
Demory, B.-O., Gillon, M., Madhusudhan, N., Queloz, D.: Mon. Not. R. Astron. Soc. **455**, 2018 (2016)
Dempsey, A.M., Nelson, B.E.: Astrophy. J. **867**, 75 (2018)
De Rosa, R.J., Dawson, R., Nielsen, E.L.: Astrono. Astrophys. **640**, A73 (2020)
Désert, J.M., Charbonneau, D., Demory, B.O., et al.: Astrophy. J. Suppl. Ser. **197**, 14 (2011)
Dong, S., Zhu, Z.: Astrophy. J. **778**, 53 (2013)
Dorn, C., Khan, A., Heng, K., et al.: Astron. Astrophys. **577**, 83 (2015)
Dorn, C., Venturini, J., Khan, A., et al.: Astron. Astrophys. **597**, 37 (2017)
Dorn, C., Noack, L., Rozel, A.B.: Astron. Astrophys. **614**, A18 (2018)
Doyle, L.R., et al.: Science **333**, 1602 (2011)
Dragomir, D., Matthews, J.M., Eastman, J.D., et al.: Astrophy. J. **772**, L2 (2013)
Dressing, C.D., Charbonneau, D.: Astrophy. J. **767**, 95 (2013)
Dressing, C.D., Charbonneau, D.: Astrophy. J. **807**, 45 (2015)
Dressing, C.D., Charbonneau, D., Dumusque, X., et al.: Astrophy. J. **800**, 135 (2017)
Dumusque, X., et al.: Astron. Astrophys. **598**, A133 (2017)
Eastman, J., Gaudi, B.S., Agol, E.: Proc. Astron. Soc. Pac. **125**, 83 (2013)
Endl, M., Cochran, W.D., Kürster, M.: Astrophy. J. **649**, 436 (2006)
Fabrycky, D., Tremaine, S.: Astrophy. J. **669**, 1298 (2007)
Fabrycky, D.C., Lissauer, J.J., Ragozzine, D., et al.: Astrophy. J. **790**, 146 (2014)
Fang, J., Margot, J.-L.: Astrophy. J. **761**, 92 (2012)
Fellgett, P.: Optical Acta **2**, 9 (1955)
Fernandes, R.B., Mulders, G.D., Pascucci, I., et al.: Astrophy. J. **874**, 81 (2019)
Fischer, D.A., Valenti, J.: Astrophy. J. **622**, 1102 (2005)
Fischer, D.A., et al.: Astrophy. J. **675**, 790 (2008)
Fischer, D.A., et al.: Proc. Astron. Soc. Pac. **128**, 066001 (2016)
Ford, E.B., Rasio, F.A.: Astrophy. J. **686**, 621 (2008)
Foreman-Mackey, D., Hogg, D.W., Morton, T.D.: Astrophy. J. **795**, 64 (2014)
Foreman-Mackey, D., Montet, B.T., Hogg, D.W., et al.: Astrophy. J. **806**, 215 (2015)
Fortney, J.J., Marley, M.S., Barnes, J.W.: Astrophy. J. **659**, 1661 (2007)
Fortney, J.J., Mordasini, C., Nettelmann, N., et al.: Astrophy. J. **775**, 80 (2013)
Fressin, F., Torres, G., Charbonneau, D., et al.: Astrophy. J. **766**, 81 (2013)
Frasca, A., Manara, C.F., Alcalá, J.M., et al.: Astron. Astrophys. **639**, L8 (2020)
Frustagli, G., Poretti, E., Milbourne, T., et al.: Astron. Astrophys. **633**, 133 (2020)
Fulton, B.J., et al.: Astron. J. **142**, 84 (2011)
Fulton, B.J., Petigura, E.A., Howard, A.W., et al.: Astron. J. **154**, 109 (2017)
Fulton, B.J., Petigura, E.A.: Astron. J. **156**, 264 (2018)
Fulton, B.J., Rosenthal, L.J., Hirsch, L.A., et al.: Astrophy. J. Suppl. Ser. (2021) in press (arXiv:2105.11584)
Gaidos, E., Mann, A.W., Kraus, A.L., Ireland, M.: Mon. Not. R. Astron. Soc. **457**, 2877 (2016)
Gandolfi, D., Barragán, O., Hatzes, A.P., et al.: Astron. J. **154**, 123 (2017)
Gaia Collaboration, Prusti, T., de Bruijne, J.H.J., et al.: Astron. Astrophys. **595**, A1 (2016a)
Gaia Collaboration, Brown, A.G.A., Vallenari, A., et al.: Astron. Astrophys. **595**, A2 (2016b)
Collaboration, Gaia, Brown, A.G.A., Vallenari, A., et al.: Astron. Astrophys. **616**, 22 (2018)
Gandolfi, D., Collier Cameron, A., Endl, M., et al.: Astron. Astrophys. **543**, L5 (2012)
Garrett, D., Savransky, D., Belikov, Rus, 2018, Proc. Astron. Soc. Pac. **130**, 4403
Gaudi, B.S., Stassun, K.G., Collins, K.A., et al.: Nature **546**, 514 (2017)
Ghezzi, L., Cuñha, K., Smith, V. V., et al.: Astrophy. J. **720**, 1290 (2010)
Ghezzi, L., Montet, B.T., Johnson, J.A.: Astrophy. J. **860**, 109 (2018)
Gibbs, A., Bixel, A., Rackham, B.V., et al.: Astron. J. **159**, 169 (2020)

Gilbert, G.J., Fabrycky, D.C.: Astron. J. **159**, 281 (2020)
Gillon, M., Demory, B.-O., Barman, T., et al.: Astron. Astrophys. **471**, L51 (2007)
Gillon, M., Triaud, A.H.M.J., Fortney, J.J., et al.: Astron. Astrophys. **542**, A4 (2012)
Gillon, M., et al.: Nature **542**, 23 (2017)
Ginzburg, S., Schlichting, H.E., Sari, R.: Astrophy. J. **825**, 29 (2016)
Ginzburg, S., Schlichting, H.E., Sari, R.: Mon. Not. R. Astron. Soc. **476**, 759 (2018)
Gizon, L., Solanki, S.K.: **589**, 1009 (2003)
Goldreich, P., Schlichting, H.E.: Astron. J. **147**, 32 (2014)
Greene, T.P., et al.: Astrophy. J. **817**, 17 (2016)
Griffin, R.F.: Astrophy. J. **148**, 465 (1967)
Guilluy, G., Gressier, A., Wright, S., et al.: Astron. J. **161**, 19 (2021)
Guenther, E.W., Barragán, O., Dai, F., et al.: Astron. J. **608**, 93 (2017)
Gupta, A., Schlichting, H.E.: Mon. Not. R. Astron. Soc. **487**, 24 (2019)
Hansen, B.M.S., Murray, N.: Astrophy. J. **775**, 53 (2013)
Hansen, B.M.S., Murray, N.: Mon. Not. R. Astron. Soc. **448**, 1044 (2015)
Hara, N.C., Bouchy, F., Stalport, M., et al.: Astron. Astrophys. **636**, L6 (2020)
Hardegree-Ullman, K.K., Cushing, M.C., Muirhead, P.S., Christiansen, J.L.: Astron. J. **158**, 75 (2019)
Hartman, J.D., Bakos, G.A., Buchhave, L.A., et al.: Astron. J. **150**, 197 (2015)
Hatzes, A.P., Dvorak, R., Wuchterl, G., et al.: Astron. Astrophys. **520**, A93 (2010)
Hatzes, A.P.: Methods of Detecting Exoplanets, p. 3 . Springer, Berlin (2016)
Haywood, R.D., Cameron, A.C., Queloz, D., et al.: Mon. Not. R. Astron. Soc. **443**, 2517 (2014)
He, M.Y., Ford, E.B., Ragozzine, D.: Mon. Not. R. Astron. Soc. **490**, 4575 (2019)
He, M.Y., Ford, E.B., Ragozzine, D., Carrera, D.: Astron. J. **160**, 276 (2020)
Hébrard, G., Ehrenreich, D., Bouchy, F., et al.: Astron. Astrophys. **527**, L11 (2011)
Henry, G.W., Marcy, G.W., Butler, R.P., Vogt, S.S.: Astrophy. J. **529**, L41 (1999)
Hirano, T., Gaidos, E., Winn, J.N., et al.: Astrophy. J. Lett. **890**, L27 (2020)
Horne, J.H., Baliunas, S.L.: Astrophy. J. **302**, 757 (1986)
Howard, A.W., et al.: Astrophy. J. **721**, 1467 (2010a)
Howard, A.W., Marcy, G.W., Johnson, J.A., et al.: Science **330**, 653 (2010b)
Howard, A.W., Johnson, J.A., Marcy, G.W., et al.: Astrophy. J. **730**, 10 (2011)
Howard, A.W., Marcy, Marcy, G. W., Bryson, S. T., et al.: Astrophy. J. Supplement Series **201**, 15 (2012)
Howard, A.W., Sanchis-Ojeda, R., Marcy, G.W., et al.: Nature **503**, 381 (2013)
Howard, A.W., Fulton, B.J.: Proc. Astron. Soc. Pac. **128**, 114401 (2016)
Howe, A.R., Burrows, A., Verne, W.: Astrophy. J. **787**, 173 (2014)
Hsu, D.C., Ford, E.B., Ragozzine, D., Morehead, R.C.: Astron. J. **155**, 205 (2018)
Hsu, D.C., Ford, E.B., Ragozzine, D., Ashby, K.: Astron. J. **158**, 109 (2019)
Hsu, D.C., Ford, E.B., Terrien, R.: Mon. Not. R. Astron. Soc. **498**, 2249 (2020)
Huang, C.X., Petrovich, C., Deibert, E.: Astron. J. **153**, 210 (2017)
Huang, C.X., Burt, J., Vanderburg, A., et al.: Astrophy. J. **868**, L39 (2018)
Ida, S., Lin, D.N.C.: Astrophy. J. **626**, 1045 (2005)
Ida, S., Lin, D.N.C.: Astrophy. J. **685**, 584 (2008)
Ida, S., Lin, D.N.C.: Astrophy. J. **719**, 810 (2010)
Ida, S., Lin, D.N.C.: Astrophy. J. **775**, 42 (2013)
Inamdar, N.K., Schlichting, H.E.: Astrophy. J. **817**, 13 (2016)
Izidoro, A., Ogihara, M., Raymond, S.N., et al.: Mon. Not. R. Astron. Soc. **470**, 1750 (2017)
Jackson, A.P., Davis, T.A., Wheatley, P.J.: Mon. Not. R. Astron. Soc. **422**, 2024 (2012)
Jackson, B., Stark, C.C., Adams, E.R., et al.: Astrophy. J. **779**, 2 (2013)
Jiang, C.-F., Xie, J.-W., Zhou, J.-L.: Astron. J. **160**, 180 (2020)
Jin, S., Mordasini, C., Parmentier, V., et al.: Astrophy. J. **795**, 65 (2014)
Jin, S., Mordasini, C.: Astrophy. J. **853**, 163 (2018)
Johansen, A., Davies, M.B., Church, R.P., Holmelin, V.: Astrophy. J. **758**, 39 (2012)

Johansen, A., Lambrechts, M.: Ann. Rev. Earth Planet. Sci. **45**, 359 (2017)
Johnson, J.A., Aller, K.M., Howard, A.W., Crepp, J.R.: Proc. Astron. Soc. Pac. **122**, 905 (2010)
Jurgenson, C., Fischer, D., McCracken, T., et al.: Proc. SPIE **9908**, 99086T (2016)
Jurić, M., Tremaine, S.: Astrophy. J. **686**, 603 (2008)
Juvan, I.G., Lendl, M., Cubillos, P.E., et al.: Astron. Astrophys. **610**, A15 (2018)
Kane, S.R., Ciardi, D.R., Gelino, D.M., von Braun, K.: Mon. Not. R. Astron. Soc. **425**, 757 (2012)
Kawashima, Y., Hu, R., Ikoma, M.: Astrophy. J. **876**, L5 (2019)
Knutson, H.A., Dragomir, D., Kreidberg, L., et al.: Astrophy. J. **794**, 155 (2014a)
Knutson, H.A., Benneke, B., Deming, D., et al.: Nature **505**, 66 (2014b)
König, K.: Astrophy. J. **370**, L37 (1991)
Köingl, A., Giacalone, S., Matsakos, T.: Astrophy. J. Lett. **846**, L13 (2017)
Kopparapu, R.K.: Astrophy. J. **767**, L8 (2013)
Kopparapu, R.K., Hébrard, E., Belikov, R., et al.: Astrophy. J. **856**, 122 (2018)
Kovács, G., Zucker, S., Mazeh, T.: Astron. Astrophys. **391**, 369 (2002)
Kovács, G., Hodgkin, S., Sipőcz, B., et al.: Mon. Not. R. Astron. Soc. **433**, 889 (2013)
Kraft, R.P.: Astrophy. J. **150**, 551 (1967)
Kraus, S., Le Bouquin, J.-B., Kreplin, A., et al.: Astrophy. J. **897**, L8 (2020)
Kreidberg, L., Bean, J.L., Désert, J.-M., et al.: Nature **505**, 69 (2014)
Kreidberg, L., Molliére, P., Crossfield, I. J. M., et al.: (2020). arXiv:2006.07444
Kunimoto, M., Matthews, J.M.: Astron. J. **159**, 248 (2020)
Lai, D.: Mon. Not. R. Astron. Soc. **423**, 486 (2012)
Lambrechts, M., Morbidelli, A., Jacobson, S.A., et al.: Astron. Astrophys. **627**, A83 (2019)
Latham, D.W., Rowe, J.F., Quinn, S.N.: Astrophy. J. **732**, L24 (2011)
Lee, E.J., Chiang, E., Ormel, C.W.: Astrophy. J. **797**, 95 (2014)
Lee, E.J., Chang, Ph., Murray, N.: Astrophy. J. **800**, 49 (2015)
Lee, E.J., Chiang, E.: Astrophy. J. **817**, 90 (2016)
Lee, E.J., Chiang, E.: Astrophy. J. **842**, 40 (2017)
Léger, A., Selsis, F., Sotin, C., et al.: Icarus **169**, 499 (2004)
Léger, A., Rouan, D., Schneider, J., et al.: Astron. Astrophys. **506**, 287 (2009)
Léger, A., Grasset, O., Fegley, B., et al.: Icarus **213**, 1 (2011)
Li, J., Lai, D.: Astrophy. J. **898**, L20 (2020)
Limbach, M.A., Turner, E.L.: Proc. Natl. Acad. Sci. **112**, 20 (2015)
Lin, D.N.C., Bodenheimer, P., Richardson, D.C.: Nature **380**, 606 (1996)
Lissauer, J.J., Pollack, J.B., Wetherill, G.W., Stevenson, D.J.: Neptun and Triton, vol. 37. Cruikshank Univ. of Arizona Press, Tucson (1995)
Lissauer, J.J., Fabrycky, D.C., Ford, E.B., et al.: Nature **470**, 53 (2011a)
Lissauer, J.J., Ragozzine, D., Fabrycky, D.C., et al.: Astrophy. J. Suppl. Ser. **197**, 8 (2011b)
Lissauer, J.J., Marcy, G.W., Rowe, J.F., et al.: Astrophy. J. **750**, 112 (2012)
Lithwick, Y., Xie, J., Wu, Y.: Astrophy. J. **761**, 122 (2012)
Lomb, N.R.: Astrophys. Space Sci. **39**, 447 (1976)
Lopez, E.D., Fortney, J.J., Miller, N.: Astrophy. J. **761**, 59 (2012)
Lopez, E.D., Fortney, J.J.: Astrophy. J. **776**, 2 (2013)
Lopez, E.D., Fortney, J.J.: Astrophy. J. **792**, 1 (2014)
Lopez, E.D.: Mon. Not. R. Astron. Soc. **472**, 245 (2017)
Lopez, E.D., Rice, K.: Mon. Not. R. Astron. Soc. **479**, 5303 (2018)
Louden, E.M., Winn, J.N., Petigura, E.A., et al.: Astron. J. **161**, 68 (2021)
Lovis, C., Mayor, M., Pepe, F., et al.: Nature **441**, 305 (2006)
Lovis, C., Ségransan, D., Mayor, M., et al.: Astron. Astrophys. **528**, A112 (2011)
Lozovsky, M., Helled, R., Dorn, C., Venturini, J.: Astrophy. J. **866**, 49 (2018)
Lu, C.X., Schlaufman, K.C., Cheng, S.: Astron. J. **160**, 253 (2020)
Lundkvist, M.S., Kjeldsen, H., Albrecht, S., et al.: Nat. Commun. **7**, 11201 (2016)
MacDonald, M.G., Dawson, R.I., Morrison, S.J., et al.: Astrophy. J. **891**, 20 (2020)
Madhusudhan, N., Nixon, M.C., Welbanks, L., et al.: Astrophy. J. **891**, L7 (2020)

Malavolta, L., Mayo, A.W., Louden, T., et al.: Astron. J. **155**, 107 (2018)
Maldonado, J., Micela, G., Baratella, M., et al.: Astron. Astrophys. **644**, A68 (2020)
Mancini, L., Southworth, J., Raia, G., et al.: Mon. Not. R. Astron. Soc. **465**, 843 (2017)
Mancini, L., Esposito, M., Covino, E., et al.: Astron. Astrophys. **613**, A41 (2018)
Mandel, K., Agol, E.: Astrophy. J. **580**, L171 (2002)
Marcy, G.W., Isaacson, H., Howard, A.W., et al.: Astrophy. J. Suppl. Ser. **210**, 20 (2014)
Martinez, C.F., Cunha, K., Ghezzi, L., et al.: Astrophy. J. **875**, 29 (2019)
Marzari, F., Nelson, A.F.: Astrophy. J. **705**, 1575 (2009)
Masuda, K., Winn, J.N., Kawahara, H.: Astron. J. **159**, 38 (2020)
Matsumoto, Y., Kokubo, E.: Astron. J. **154**, 27 (2017)
Matsumura, S., Peale, S.J., Rasio, F.A.: Astrophy. J. **725**, 1995 (2010)
Mayor, M., Udry, S., Lovis, C., et al.: Astron. Astrophys. **493**, 639 (2009)
Mayor, M., Marmier, M., Lovis, C., et al.: (2011). arXiv:1109.2497
Mayor, M., Queloz, D.: Nature **378**, 355 (1995)
Mazeh, T., Perets, H.B., McQuillan, A., Goldstein, E.S.: Astrophy. J. **801**, 3 (2014)
Mazeh, T., Holczer, T., Faigler, S.: Astron. Astrophys. **589**, A75 (2016)
McArthur, B.E., Benedict, G.F., Barnes, R., et al.: Astrophy. J. **715**, 1203 (2010)
McCullough, P.R., Stys, J.E., Valenti, J.A., et al.: Proc. Astron. Soc. Pac. **117**, 783 (2005)
Mikal-Evans, T., Crossfield, I.J.M., Benneke, B., et al.: Astron. J. **161**, 18 (2021)
Miller, G.R.M., Collier Cameron, A., Simpson, E.K., et al.: Astron. Astrophys. **523**, A52 (2010)
Miller-Ricci, E., Rowe, J.F., Sasselov, D., et al.: Astrophy. J. **682**, 586 (2008a)
Miller-Ricci, E., Rowe, J.F., Sasselov, D., et al.: Astrophy. J. **682**, 593 (2008b)
Miller-Ricci, E., Seager, S., Sasselov, D.: Astrophy. J. **690**, 1056 (2009)
Millholland, S., Wang, S., Laughlin, G.: Astrophy. J. **849**, L33 (2017)
Millholland, S., Laughlin, G.: Nature Astronomy **3**, 424 (2019)
Millholland, S., Spalding, C.: Astrophy. J. **905**, 71 (2020)
Mills, S.M., Howard, A.W., Petigura, E.A., et al.: Astron. J. **157**, 198 (2019)
Morbidelli, A., Lambrechts, M., Jacobson, S., Bitsch, B., Icarus 258, 418 (2015)
Morbidelli, A., Bitsch, B., Crida, A., et al.: Icarus **267**, 368 (2016)
Mordasini, C., Alibert, Y., Benz, W.: Astron. Astrophys. **501**, 1139 (2009a)
Mordasini, C., Alibert, Y., Benz, W., Naef, D.: Astron. Astrophys. **501**, 1161 (2009b)
Mordasini, C., Alibert, Y., Benz, W., et al.: Astron. Astrophys. **541**, A97 (2012a)
Mordasini, C., Alibert, Y., Klahr, H., Henning, T.: Astron. Astrophys. **547**, A111 (2012b)
Mordasini, C., Alibert, Y., Georgy, C., et al.: Astron. Astrophys. **547**, A112 (2012c)
Mordasini, C., Klahr, H., Alibert, Y., et al.: Astron. Astrophys. **566**, A141 (2014)
Moorhead, A.V., Ford, E.B., Morehead, R.C., et al.: Astrophy. J. Suppl. Ser. **197**, 1 (2011)
Mortier, A., Santos, N.C., Sozzetti, A., et al.: Astron. Astrophys. **543**, A45 (2012)
Mousis, O., Deleuil, M., Aguichine, A., et al.: Astrophy. J. **896**, L22 (2020)
Mulders, G.D., Pascucci, I., Apai, D.: Astrophy. J. **798**, 112 (2015a)
Mulders, G.D., Ciesla, F.J., Min, M., et al.: Astrophy. J. **807**, 9 (2015b)
Mulders, G.D., Pascucci, I., Apai, D., Ciesla, F.J.: Astron. J. **156**, 24 (2018)
Mullally, F., Coughlin, J.L., Thompson, S.E., et al.: Astrophy. J. Suppl. Ser. **217**, 31 (2015)
Muñoz, D.J., Perets, H.B.: Astrophy. J. **156**, 253 (2018)
Munoz Romero, C.E., Kempton, E.M.-R.: Astron. J. **155**, 134 (2018)
Murchikova, L., Tremaine, S.: Astron. J. **160**, 160 (2020)
Mustill, A.J., Davies, M.B., Johansen, A.: Mon. Not. R. Astron. Soc. **468**, 3000 (2017)
Naef, D., Latham, D.W., Mayor, M., et al.: Astron. Astrophys. **375**, L27 (2001)
Nagasawa, M., Ida, S., Bessho, T.: Astrophy. J. **678**, 498 (2008)
Narang, M., Manoj, P., Furlan, E., et al.: Astron. J. **156**, 221 (2018)
Narita, N., Sato, B., Hirano, T., Tamura, M.: Proc. Astron. Soc. Jpn. **61**, L35 (2009)
Ogihara, M., Kokubo, E., Suzuki, T.K., Morbidelli, A.: Astron. Astrophys. **615**, A63 (2018)
Ormel, C.W., Liu, B., Schoonenberg, D.: Astron. Astrophys. **604**, A1O (2017)
Otegi, J.F., Bouchy, F., Helled, R.: Astron. Astrophys. **634**, A43O (2020)

Owen, J.E., Wu, Y.: Astrophy. J. **775**, 105O (2013)
Owen, J.E., Wu, Y.: Astrophy. J. **817**, 107 (2016)
Owen, J.E., Wu, Y.: Astrophy. J. **847**, 29O (2017)
Owen, J.E.: Ann. Rev. Earth Planet. Sci. **47**, 67 (2019)
Paardekooper, S.-J., Baruteau, C., Meru, F.: Mon. Not. R. Astron. Soc. **416**, 65 (2011)
Paardekooper, S.-J., Rein, H., Kley, W.: Mon. Not. R. Astron. Soc. **434**, 3018 (2013)
Pascucci, I., Mulders, G.D., Lopez, E.: Astrophy. J. **883**, 15 (2019)
Patra, K.C., Winn, J.N., Holman, M.J., et al.: Astrophy. J. **154**, 4 (2017)
Pepe, F., Cameron, A.C., Latham, D.W., et al.: Nature **503**, 377 (2013)
Pepe, F., Cristiani, S., Rebolo, R., et al.: Astron. Astrophys. **645**, A96 (2021)
Pepper, J., et al.: Proc. Astron. Soc. Pac. **119**, 923 (2007)
Perryman, M.: The Exoplanet Handbook, 2nd edn. Cambridge University Press, Cambridge (2018)
Petigura, E.A., Marcy, G.W., Howard, A.W., et al.: Astrophy. J. **770**, 69 (2013a)
Petigura, E.A., Howard, A.W., Marcy, G. W., et al.: Proc. Natl Acad. Sci. **110**, 19273 (2013b)
Petigura, E.A., Howard, A.W., Marcy, G.W., et al.: (2017), **154**, 107
Petigura, E.A., Marcy, G.W., Winn, J.N., et al.: Astron. J. **155**, 89 (2018)
Petigura, E.A.: Astron. J. **160**, 89 (2020)
Petrovich, C., Deibert, E., We, Y.: Astrophy. J. **157**, 180 (2019)
Pichierri, G., Morbidelli, A.: Mon. Not. R. Astron. Soc. **494**, 4950 (2020)
Pickering, E.C.: Mon. Not. R. Astron. Soc. **50**, 296 (1890)
Pollacco, D.L., Skillen, I., Cameron, A.C., et al.: Proc. Astron. Soc. Pac. **118**, 1407 (2006)
Pollack, J.B., Hubickyj, O., Bodenheimer, P., et al.: Icarus **124**, 62 (1996)
Poon, S.T.S., Nelson, R.P.: Mon. Not. R. Astron. Soc. **498**, 5166 (2020)
Poon, S.T.S., Nelson, R.P., Jacobson, S.A.: Mon. Not. R. Astron. Soc. **491**, 5595 (2020)
Pu, B., Wu, Y.: Astrophy. J. **807**, 44 (2015)
Pu, B., Lai, D.: Mon. Not. R. Astron. Soc. **478**, 197 (2018)
Pu, B., Lai, D.: Mon. Not. R. Astron. Soc. **488**, 3568 (2019)
Queloz, D.: New developments in array technology and applications. In: IAU Symposium. vol. 167, 221 (1995)
Queloz, D.: Astron. Astrophys. **379**, 279 (2001)
Rainer, M., Borsa, F., Pino, L., et al.: (2021). arXiv:2103.10395
Rasio, F.A., Ford, E.B.: Science **274**, 954 (1996)
Rauer, H., et al.: Exp. Astr. **38**, 249 (2014)
Raymond, S.N., Armitage, P.J., Gorelick, N.: Astrophy. J. **711**, 772 (2010)
Raymond, S.N., Boulet, T., Izidoro, A., et al.: Mon. Not. R. Astron. Soc. **479**, 81 (2018)
Reffert, S., Bergmann, C., Quirrenbach, A., et al.: Astron. Astrophys. **574**, A116 (2015)
Ricker, G.R., Winn, J.N., Vanderspek, R., et al.: JATIS **1**, 014003 (2015)
Rivera, E.J., Lissauer, J.J.: Astrophy. J. **558**, 392 (2001)
Rivera, E.J., Laughlin, G., Butler, R.P., et al.: Astrophy. J. **719**, 890 (2010)
Rogers, T.M., Lin, D.N.C., Lau, H.H.B.: Astrophy. J. **758**, L6 (2012)
Rogers, L.A.: Astrophy. J. **801**, 41 (2015)
Rogers, L.A., Seager, S.: Astrophy. J. **712**, 974 (2010)
Romanova, M.M., Owocki, S.P.: The strongest magnetic fields in the universe. In: Beskin et al. (eds.) Space Science Series of ISSI, vol. 54, , p. 347. Springer, New York (2016)
Rouan, D., Deeg, H.J., Demangeon, O., et al.: Astrophy. J. Lett. **741**, L30 (2011)
Rowe, J.F., Bryson, S.T., Marcy, G.W., et al.: Astrophy. J. **784**, 45 (2014)
Sanchis-Ojeda, R., Winn, J.N., Holman, M.J.: Astrophy. J. **733**, 127 (2011a)
Sanchis-Ojeda, R., Winn, J.N.: Astrophy. J. **743**, 61 (2011b)
Sanchis-Ojeda, R., Rappaport, S., Winn, J.N., et al.: Astrophy. J. **774**, 54 (2013a)
Sanchis-Ojeda, R., Winn, J.N., Marcy, G.W.: Astrophy. J. **775**, 54 (2013b)
Sanchis-Ojeda, R., Rappaport, S., Winn, J.N., Kotson, M.C.: Astrophy. J. **787**, 47 (2014)
Sandford, E., Kipping, D., Collins, M.: Mon. Not. R. Astron. Soc. **489**, 3162 (2019)
Santerne, A., Brugger, B., Armstrong, D.J., et al.: Nat. Astron. **2**, 393 (2018)

Santos, N.C., Israelian, G., Mayor, M.: Astron. Astrophys. **415**, 1153 (2004a)
Santos, N.C., Bouchy, F., Mayor, M., et al.: Astron. Astrophys. **426**, 19 (2004b)
Scargle, J.D.: Astrophy. J. **263**, 835 (1982)
Schlaufman, K.C.: Astrophy. J. **719**, 602 (2010)
Schlaufman, K.C.: Astrophy. J. **790**, 91 (2014)
Schlichting, H.E., Sari, R., Yalinewich, A.: Icarus, **247**, 81 (2015)
Seager, S., Mallén-Ornelas, G.: Astrophy. J. **585**, 1038 (2003)
Seager, S., Kuchner, M., Hier-Majumder, C.A., Militzer, B.: Astrophy. J. **669**, 1279 (2007)
Shallue, C.J., Vanderburg, A.: Astron. J. **155**, 9 (2018)
Silburt, A., Gaidos, E., Wu, Y.: Astrophy. J. **799**, 180 (2015)
Sing, D.: Observational techniques with transiting exoplanetary atmospheres. In: Bozza, V., Mancini, L. Sozzetti, A. (eds.) Astrophysics of Exoplanetary Atmospheres: 2nd Advanced School on Exoplanetary Science, Astrophysics and Space Science Library, vol. 450, p. 3. Springer International Publishing Switzerland (2018)
Sinukoff, E., Howard, A.W., Petigura, E.A., et al.: Astron. J. **153**, 271 (2017)
Snellen, I.A.G., Stuik, R., Navarro, R., et al.: Proc. SPIE **8444**, 84440I (2012)
Sousa, S.G., Santos, N.C., Mayor, M., et al.: Astron. Astrophys. **487**, 373 (2008)
Sousa, S.G., Adibekyan, V., Santos, N.C., et al.: Mon. Not. R. Astron. Soc. **485**, 3981 (2019)
Southworth, J.: Mon. Not. R. Astron. Soc. **417**, 2166 (2011)
Southworth, J.: Astron. Astrophys. **557**, A119 (2013)
Sozzetti, A., Torres, G., Latham, D.W., et al.: Astrophy. J. **697**, 544 (2009)
Sozzetti, A., Bernagozzi, A., Bertolini, E., et al.: EPJWC **47**, 03006 (2013)
Sozzetti, A., Damasso, M., Bonomo, A.S., et al.: Astron. Astrophys. **648**, A75 (2021)
Spalding, C., Batygin, K.: Astrophy. J. **811**, 82 (2015)
Spalding, C., Batygin, K.: Astrophy. J. **830**, 5 (2016)
Spalding, C., Millholland, S.: Astron. J. **160**, 105 (2020)
Stauffer, J., Cody, A.M., McGinnis, P., et al.: Astron. J. **149**, 130 (2015)
Stefansson, G., Mahadevan, S., Maney, M., et al.: Astron. J. **160**, 192 (2020)
Steffen, J.H., Farr, W.M.: Astrophy. J. **774**, 12L (2013)
Steffen, J.H., Ragozzine, D., Fabrycky, D.C., et al.: Proc. Natl. Acad. Sci. **109**, 7982S (2012)
Szabó, G., M., Kiss, L.L.: Astrophy. J. **727**, L44 (2011)
Takaishi, D., Tsukamoto, Y., Suto, Y.: Mon. Not. R. Astron. Soc. **492**, 5641 (2020)
Tanaka, H., Takeuchi, T., Ward, W.R.: Astrophy. J. **565**, 1257 (2002)
Terquem, C., Papaloizou, J.C.B.: Mon. Not. R. Astron. Soc. **482**, 530 (2019)
Thompson, S.E., Coughlin, J.L., Hoffman, K., et al.: Astrophy. J. Suppl. Ser. **235**, 38 (2018)
Tinetti, G., Drossart, P., Eccleston, P., et al.: Exp. Astr. **46**, 135 (2018)
Torres, G., Fischer, D.A., Sozzetti, A., et al.: Astrophy. J. **757**, 161 (2012)
Traub, W.A.: Astrophy. J. **745**, 20 (2012)
Tregloan-Reed, J., Southworth, J., Tappert, C.: Mon. Not. R. Astron. Soc. **428**, 3671 (2013)
Tregloan-Reed, J., Southworth, J., Burgdorf, M., et al.: Mon. Not. R. Astron. Soc. **450**, 1760 (2015)
Tremaine, S., Dong, S.: Astron. J. **143**, 94 (2012)
Triaud, A.H.M.J.: Handbook of Exoplanets. Springer International Publishing AG, id. 2 (2018)
Tsiaras, A., Waldmann, I.P., Tinetti, G., et al.: Nat. Astron. **450**, 1760 (2019)
Tuomi, M.: aap, **543**, A52 (2012)
Tuomi, M., Jones, H.R.A., Barnes, J.R.: Mon. Not. R. Astron. Soc. **441**, 1545 (2014)
Turbet, M., Ehrenreich, D., Lovis, C., et al.: Astron. Astrophys. **628**, A12 (2019)
Turbet, M., Bolmont, E., Ehrenreich, D., et al.: Astron. Astrophys. **638**, 41 (2020)
Turrini, D., Zinzi, A., Belinchon, J.A.: Astron. Astrophys. **636**, A53 (2020)
Udalski, A., et al.: Acta Astron. **52**, 1 (2002)
Udry, S., Mayor, M., Santos, N.C.: Astron. Astrophys. **407**, 369 (2003)
Udry, S., Dumusque, X., Lovis, C., et al.: Astron. Astrophys. **622**, A37 (2019)
Valencia, D., Sasselov, D.D., O'Connell, R.J.: Astrophy. J. **665**, 1413 (2007)
Valencia, D., Ikoma, M., Guillot, T., Nettelmann, N.: Astron. Astrophys. **516**, 20 (2010)

Valsecchi, F., Rasio, F.A.: Astrophy. J. **786**, 102 (2014)
Valsecchi, F., Rappaport, S., Rasio, F.A., et al.: Astrophy. J. **813**, 101 (2015)
Van Eylen, V., Albrecht, S.: Astrophy. J. **808**, 126 (2015)
Van Eylen, V., Agentoft, C., Lundkvist, M.S., et al.: Mon. Not. R. Astron. Soc. **479**, 4786 (2018)
Van Eylen, V., Albrecht, S., Huang, Xu., et al.: Astron. J. **157**, 61 (2019)
Van Grootel, V., Gillon, M., Valencia, D., et al.: Astrophy. J. **786**, 2 (2014)
Vandenburg, A., et al.: Astrophy. J. Suppl. Ser. **222**, 14 (2016)
Vanderburg, A., Becker, J.C., Buchhave, L.A., et al.: Astrophy. J. **154**, 237 (2017)
Venturini, J., Guilera, O.M., Haldemann, J., et al.: Astron. Astrophys. **643**, L1 (2020)
Volk, K., Malhotra, R.: Astron. J. **160**, 98 (2020)
Wang, J., Fischer, D.A.: Astron. J. **149**, 14 (2015)
Ward, W.R.: Astrophy. J. **482**, L211 (1997)
Weiss, L.M., Marcy, G.W.: Astrophy. J. **783**, L6 (2014)
Weiss, L.M., Rogers, L.A., Isaacson, H.T., et al.: Astrophy. J. **819**, 83 (2016)
Weiss, L.M., Isaacson, H.T., Marcy, G.W., et al.: Astron. J. **156**, 254 (2018a)
Weiss, L.M., Marcy, G.W., Petigura, E.A., et al.: Astron. J. **155**, 48 (2018b)
Weiss, L.M., Petigura, E.A.: Astrophy. J. **893**, L1 (2020)
Welsh, W.F., Orosz, J.A.: Handbook of Exoplanets. Springer International Publishing AG, id. 34 (2018)
Wheatley, P.J., Pollacco, D.L., Queloz, D., et al.: EPJ Web Conf. **47**, 13002 (2013)
Wheatley, P.J.: European Planetary Science Congress, 10, EPSC2015-908 (2015)
Wilson, R.F., Teske, J., Majewski, S.R., et al.: Astron. J. **155**, 68 (2018)
Winn, J.: Exoplanets. In: Seager S. (ed.) University of Arizona Press (2010)
Winn, J.N., Fabrycky, D.C.: Ann. Rev. Astron. Astrophys. **53**, 409 (2015)
Winn, J.N., Holman, M.J., Henry, G.W., et al.: Astron. J. **133**, 1828 (2007)
Winn, J.N., Johnson, J.A., Albrecht, S., et al.: Astrophy. J. **703**, L99 (2009)
Winn, J.N., Fabrycky, D., Albrecht, S., Johnson, J.A.: Astrophy. J. **718**, L145 (2010)
Winn, J.N., Matthews, J.M., Dawson, R.I., et al.: Astrophy. J. Lett. **737**, L18 (2011)
Winn, J.N., Petigura, E.A., Morton, T.D., et al.: Astron. J. **154**, 270 (2017a)
Winn, J.N., Sanchis-Ojeda, R., Rogers, L., et al.: Astrophy. J. **154**, 60 (2017b)
Winn, J.N., Sanchis-Ojeda, R., Rappaport, S.: New Astron. Rev. **83**, 37 (2018)
Wittenmyer, R.A., Tinney, C.G., Butler, R.P., et al.: Astrophy. J. **738**, 81 (2011)
Wittenmyer, R.A., Wang, S., Horner, J., et al.: Mon. Not. R. Astron. Soc. **492**, 377 (2020)
Wolfgang, A., Rogers, L.A., Ford, E.B.: Astrophy. J. **825**, 19 (2016)
Wolszczan, A., Frail, D.A.: Nature **355**, 145 (1992)
Wright, J.T., Upadhyay, S., Marcy, G.W., et al.: Astrophy. J. **693**, 1084 (2009)
Wright, J.T., Fakhouri, O., Marcy, G.W., et al.: Proc. Astron. Soc. Pac. **123**, 412 (2011)
Wright, J.T., Marcy, G.W., Howard, A.W., et al.: Astrophy. J. **753**, 160 (2012)
Wright, J.: Handbook of Exoplanets. Springer International Publishing AG, id. 4 (2018)
Wu, Y., Murray, N.: Astrophy. J. **589**, 605 (2003)
Wu, Y.: Astrophy. J. **874**, 91 (2019)
Wu, Y., Lithwick, Y.: Astrophy. J. **772**, 74 (2013)
Xie, J.-W., Dong, S., Zhu, Z., et al.: Proc. Natl. Acad. Sci. **113**, 11431 (2016)
Xu, W., Lai, D.: Mon. Not. R. Astron. Soc. **468**, 3223 (2017)
Xuan, J.W., Wyatt, M.C.: Mon. Not. R. Astron. Soc. **497**, 2096 (2020)
Yang, J.-Y., Xie, J.-W., Zhou, J.-L.: Astron. J. **159**, 164 (2020)
Youdin, A.N.: Astrophy. J. **742**, 38 (2011)
Zechmeister, M., Kürster, M.: Astron. Astrophys. **49**, 577 (2009)
Zeng, L., Sasselov, D.D.: Proc. Astron. Soc. Pac. **125**, 227 (2013)
Zeng, L., Sasselov, D.D., Jacobsen, S.B.: Astrophy. J. **819**, 127 (2016)
Zeng, L., Jacobsen, S.B., Sasselov, D.D., et al.: Proc. Natl. Acad. Sci. **116**, 9723 (2019)
Zhou, G., Latham, D.W., Bieryla, A., et al.: Mon. Not. R. Astron. Soc. **460**, 3376 (2016)
Zhou, G., Bakos, G.Á., Bayliss, D., et al.: Astron. J. **157**, 31 (2019a)

Zhou, G., Huang, C.X., Bakos, G.Á.: Astron. J. **158**, 141 (2019b)
Zhou, G., Winn, J.N., Newton, E.R., et al.: Astrophy. J. Lett. **892**, L21 (2020)
Zhu, W., Wang, J., Huang, C.: Astrophy. J. **832**, 196 (2016)
Zhu, W., Wu, Y.: Astron. J. **156**, 92 (2018)
Zhu, W., Petrovich, C., Wu, Y., et al.: Astrophy. J. **860**, 101 (2018)
Zhu, W.: Astrophy. J. **873**, 8 (2019)
Zhu, W.: Astron. J. **159**, 188 (2020)
Zink, J.K., Hansen, B.M.S.: Mon. Not. R. Astron. Soc. **487**, 246 (2019)
Zink, J.K., Christiansen, J.L., Hansen, B.M.S.: Mon. Not. R. Astron. Soc. **483**, 4479 (2019)
Zinzi, A., Turrini, D.: Astron. Astrophys. **605**, 4 (2017)